Wide Speed Control of Permanent Magnet Synchronous Motors with Improved Torque Capacity

by

Gabriel Moscardi Pauka

A thesis submitted in partial fulfillment of the requirements for the degree of

Master of Science

in

Energy Systems

Department of Electrical and Computer Engineering

University of Alberta

Abstract

This research deals with wide speed control of permanent magnet synchronous machines (PMSMs) driven by voltage-source converters (VSCs). The objective is to develop a current control algorithm that allows said machines to optimize their torque for any speeds within their operational range, for any torque requested: from maximum motoring torque to maximum regenerative braking, including a no torque operation known as "coasting". This optimization will have as main objective to minimize the amount of current needed to maximize the machine's torque for a certain operating point, while taking into consideration the current and voltage limitations of the VSC and the machine in a wide-speed operation, which requires the need of field-weakening, where a portion of the machine's current is dedicated to weaken its permanent magnets in order to reduce its induced voltage. It is also discussed the concepts of finite and infinite speed machines, which difference is having valid operating points up to a maximum speed or for any rotational speeds. In order to reach this goal, the first step is to analyze the mathematical modeling of PMSMs in the dq-frame in a MATLAB script, and, with the aid of a graphical interpretation of those equations, regions of operation and boundary conditions are defined in order to determine which equations of the algorithm must be used for the reference currents generation. The mathematical modeling is then proven in a PLECS simulation, showing that the algorithm developed can be executed in a two-level three-phase VSC, successfully controlling the machine. This serves as a base for an experimental implementation of a small-scale PMSM using dSPACE MicroLabBox. The experimental results prove the control algorithm is capable of achieving its goals in a VSC-driven PMSM.

Preface

Section 2.3.1 and Chapter 4 of this thesis have been accepted for publication as G.M. Pauka, L. Ding, Y. Li "Voltage and Current Limited Maximum Torque Algorithm of SPMSM in Traction Applications", *ICPE 2023 ECCE Asia*. I was responsible for the development of the control algorithm, data processing and part of the manuscript composition , L. Ding was responsible for the experimental setup and revision of the manuscript, and Y. Li assisted with guidance for the experiments and revision of the manuscript.

to my parents

The scientists of today think deeply instead of clearly. One must be sane to think clearly, but one can think deeply and be quite insane.

– Nikola Tesla

Then it comes to be that the soothing light at the end of your tunnel
Is just a freight train coming your way

– "No Leaf Clover", Metallica

Acknowledgements

First and foremost, I would like to thank Professor Yunwei (Ryan) Li for the research opportunity and guidance.

I would also like to thank Dr. Li Ding for his support through the practical implementation of this research, especially for his patience, comprehension and suggestions during challenging moments.

And last, but not least, I would like to thank my parents for their love and support during my entire life.

Contents

1 Introduction **1**
- 1.1 Brief Problem Formulation and Research Motivation . . . 1
- 1.2 Background . . . 3
  - 1.2.1 Rotating Reference Frame . . . 3
  - 1.2.2 Three-Phase Voltage Source Converter . . . 5
    - 1.2.2.1 Space Vector Modulation . . . 7
  - 1.2.3 Permanent Magnet Synchronous Machines . . . 9
    - 1.2.3.1 Configurations of PMSMs . . . 10
    - 1.2.3.2 Mathematical Modelling of a PMSM . . . 10
  - 1.2.4 Current Control of Permanent Magnet Synchronous Machines in the Rotating Reference Frame . . . 15
    - 1.2.4.1 Introduction . . . 15
    - 1.2.4.2 Current Control in Rotor-Field Coordinates . . . 17
- 1.3 Objective and Contribution . . . 21
- 1.4 Thesis Structure . . . 21

2 Wide Speed Operation of Permanent Magnet Synchronous Machines **23**
- 2.1 Introduction . . . 23
- 2.2 Below Base Speed: Maximum Torque per Ampère . . . 27
  - 2.2.1 SPMSM . . . 28
  - 2.2.2 IPMSM . . . 28
- 2.3 Above Base Speed: Voltage and Current Limited Maximum Torque . . . 32
  - 2.3.1 Case 1: SPMSM with $I_{ch} > i_{s,max}$ . . . 37
  - 2.3.2 Case 2: SPMSM with $I_{ch} < i_{s,max}$ . . . 47
  - 2.3.3 Case 3: IPMSM with $I_{ch} > i_{s,max}$ . . . 59
  - 2.3.4 Case 4: IPMSM with $I_{ch} < i_{s,max}$ . . . 65
  - 2.3.5 Special Case: PMSM with $I_{ch} = i_{s,max}$ . . . 75
  - 2.3.6 Finite Speed PMSM Operation At or Above the Maximum Speed . . . 75
- 2.4 User Input and the Generation of $i_{s,ref}$ . . . 76
- 2.5 Complete Wide Speed Operation Algorithm . . . 77
- 2.6 Complete Control System . . . 78
- 2.7 Impacts of Lower DC Link Voltage: Undervoltage Operation . . . 79
- 2.8 Impacts of Higher Stator Current: Overcurrent Operation . . . 81
- 2.9 Impacts of the Resistive Voltage Drop . . . 82
- 2.10 Practical Considerations . . . 84
  - 2.10.1 Magnetic Saturation . . . 84
  - 2.10.2 Permanent Magnet Demagnetization . . . 84
  - 2.10.3 Thermal Constraints . . . 85

3 Simulation Results **86**
3.1 Case 1: Finite Speed SPMSM 87
3.1.1 Simulation 1: Four Quadrant Operation 87
3.1.2 Simulation 2: Coasting at the Field Weakening Region 89
3.2 Case 2: Theoretically Infinite Speed SPMSM 91
3.3 Case 3: Finite Speed IPMSM 92
3.4 Case 4: Theoretically Infinite Speed IPMSM 93

4 Experimental Results **94**
4.1 Experiment 1: System Startup at Maximum Torque 95
4.2 Experiment 2: System Stop 98
4.3 Experiment 3: Comparison to Traditional Methods 99

5 Conclusion and Future Work **100**
5.1 Conclusion 100
5.2 Recommendation of Future Work 101

References **102**

List of Tables

1.1 Space Vectors, Switching States and On-State Switches 7

2.1 Parameters for IPMSM Example 30
2.2 Parameters for Case 1 37
2.3 Parameters for Case 2 47
2.4 Parameters for Case 3 59
2.5 Parameters for Case 4 66

List of Figures

1.1 PMSM Parameters and Quantities . . . 2
1.2 Model of a Non-Ideal Two-Level VSC . . . 6
1.3 Model of the Three-Phase VSC in the dq-Frame . . . 7
1.4 Space Vector Diagram for a Two-Level VSC . . . 8
1.5 Simplified Model of a Friction Torque from a Rotational Load . . . 17
1.6 Electrical Model of a PMSM in Rotor-Field Coordinates . . . 17
1.7 Current Control Loops . . . 18
1.8 Current Control in Rotor-Field Coordinates with Axes-Decoupling . . . 20

2.1 Constant-Torque Loci for a PMSM in the dq-Frame . . . 25
2.2 Illustration of Current Trajectory . . . 26
2.3 Current Limit Circle for a PMSM in the dq-Frame . . . 27
2.4 Maximum Torque per Ampère Trajectories . . . 27
2.5 Torque Angle Definition . . . 29
2.6 Reluctance, Magnetic and Total Torques for the IPMSM Example . . . 30
2.7 MTPA Trajectory for the IPMSM Example . . . 32
2.8 Voltage-Limiting Circles for an SPMSM . . . 36
2.9 Voltage-Limiting Ellipses for an IPMSM . . . 36
2.10 Case 1 MTPA, CLC and Base Speed VLC . . . 38
2.11 Case 1 MTPA Trajectory . . . 38
2.12 Case 1 MTPA, CLC and VLCs . . . 39
2.13 Case 1 Cutoff Current . . . 39
2.14 Case 1 Cutoff Current . . . 40
2.15 Case 1 Critical Speed . . . 41
2.16 Case 1 Above Critical Speed . . . 43
2.17 Case 1 Lower Limit Current . . . 43
2.18 Case 1 Maximum Speed . . . 44
2.19 Case 1 dq-Frame Currents and Voltages for Maximum Torque . . . 46
2.20 Case 1 Torque and Power for Maximum Torque . . . 46
2.21 Case 1 dq-Frame Currents and Voltages for Zero Torque . . . 47
2.22 Case 2 MTPA, CLC and VLCs . . . 48
2.23 Case 2 MTPA, CLC and VLCs . . . 49
2.24 Case 2 Torque and Definition of $i_{s,upplim}$ . . . 50
2.25 Case 2 VLMT Trajectory . . . 50
2.26 Case 2 Upper Limit Current . . . 51
2.27 Case 2 Demagnetizing Speed . . . 52
2.28 Case 2 Current Trajectories . . . 53
2.29 Modified Case 2 . . . 53
2.30 Modified Case 2 Trajectory . . . 54
2.31 Case 2 dq-Frame Currents and Voltages for Maximum Torque . . . 56
2.32 Case 2 Torque and Power for Maximum Torque . . . 56
2.33 Case 2 dq-Frame Currents and Voltages for Zero Torque . . . 57
2.34 Modified Case 2 dq-Frame Currents and Voltages for Maximum Torque . . . 57
2.35 Modified Case 2 Torque and Power for Maximum Torque . . . 58

2.36 Modified Case 2 Torque and Power for Zero Torque 58
2.37 Case 3 MTPA, CLC and Base Speed VLE 59
2.38 Case 3 Current Trajectories 64
2.39 Case 3 dq-Frame Currents and Voltages for Maximum Torque 64
2.40 Case 3 Torque and Power for Maximum Torque 65
2.41 Case 3 dq-Frame Currents and Voltages for Zero Torque 65
2.42 Case 4 MTPA, CLC, VLEs and Torque Lines 67
2.43 Case 4 MTPV Trajectory 69
2.44 Case 4 MTPV Current 71
2.45 Case 4 Trajectories 72
2.46 Case 4 dq-Frame Currents and Voltages for Maximum Torque 74
2.47 Case 4 Torque and Power for Maximum Torque 74
2.48 Case 4 dq-Frame Currents and Voltages for Zero Torque 74
2.49 Finite Speed PMSM Algorithm 77
2.50 Theoretically Infinite Speed PMSM Algorithm 78
2.51 Complete Control System 79
2.52 Undervoltage Operation Effect on the PMSM Performance 81
2.53 Overcurrent Operation Effect on the PMSM Performance 82
2.54 Resistive Voltage Drop for Maximum Torques 83

3.1 PLECS Simulation Model 86
3.2 Case 1 Simulation Calculated Currents for Maximum Torque 87
3.3 Case 1 Simulation Calculated Torque and Power for Maximum Torque . . . 87
3.4 Case 1 Simulation 1 PMSM Speed 88
3.5 Case 1 Simulation 1 dq-Frame Currents 88
3.6 Case 1 Simulation 1 Four Quadrants Operation 89
3.7 Case 1 Simulation 1 αβ-Frame Voltage References 89
3.8 Case 1 Simulation 2 90
3.9 Case 1 Simulation 2 dq-Frame Currents in the Speed Domain 90
3.10 Case 1 Simulation 2 αβ-Frame Voltage References 90
3.11 Case 2 Simulation dq-Frame Currents 91
3.12 Case 2 Simulation Torque and Power Profiles 91
3.13 Case 3 Simulation dq-Frame Currents 92
3.14 Case 3 Simulation Torque and Power Profiles 92
3.15 Case 4 Simulation dq-Frame Currents 93
3.16 Case 4 Simulation Torque and Power Profiles 93

4.1 Experimental Setup 95
4.2 Experiment 1 Results 95
4.3 Experiment 1 dq-Frame Currents 96
4.4 Experiment 1 abc-Frame Currents 96
4.5 Experiment 1 Torque and Power Profiles 97
4.6 Experiment 1 Duty Cycles 97
4.7 Experiment 2 Results 98
4.8 Experiment 3 Results 99

Chapter 1

Introduction

The expanding electric mobility market and its demand for traction systems with higher efficiency, torque and power densities and low maintenance creates a favorable scenario for permanent magnet synchronous machines (PMSMs) when compared to synchronous reluctance machines (SRMs), permanent magnet assisted synchronous reluctance machines (PMASRMs), cage rotor induction machines (CRIMs) and DC machines [1]–[14].

This research will have as main objective to develop an optimization algorithm for a voltage-source converter (VSC) driven PMSM, which will minimize the current while maximizing the torque produced (thus "Maximum Toque per Ampère"). Said algorithm will also be optimized for a wide-speed operation, meaning that for high speeds, there will be the need of field-weakening, in which a portion of the machine's current will be used to oppose and weaken the permanent magnets, instead of being fully dedicated to generate torque. This operating region is known as "field-weakening operation", and the DC link voltage – therefore, the voltage that the VSC can impose to the PMSM – become a constraint, along with the system's currents.

1.1 Brief Problem Formulation and Research Motivation

According to [15], a PMSM can be summarized by the following equations:

$$T_m = \frac{3p_p}{2}\left(L_d - L_q\right) i_d i_q + \frac{3p_p}{2}\lambda_{pm} i_q \tag{1.1}$$

$$i_s = \sqrt{i_d^2 + i_q^2} \tag{1.2}$$

$$v_d = -\omega_e \left(L_q i_q\right) + R_s i_d + L_d \frac{di_d}{dt} \tag{1.3}$$

$$v_q = \omega_e \left(L_d i_d + \lambda_{pm}\right) + R_s i_q + L_q \frac{di_q}{dt} \tag{1.4}$$

$$v_s = \sqrt{v_d^2 + v_q^2} \tag{1.5}$$

Where T_m is the mechanical torque, p_p is the machine pole pairs, L_d and L_q are the dq-frame stator inductances, i_d and i_q are the dq-frame currents, i_s is the stator current, v_d and v_q are the dq-frame voltages, v_s is the stator voltage, ω_e is the electrical rotational speed, R_s is the stator resistance and λ_{pm} is the rotor magnetic flux linkage. These parameters and quantities can be seen in Figure 1.1.

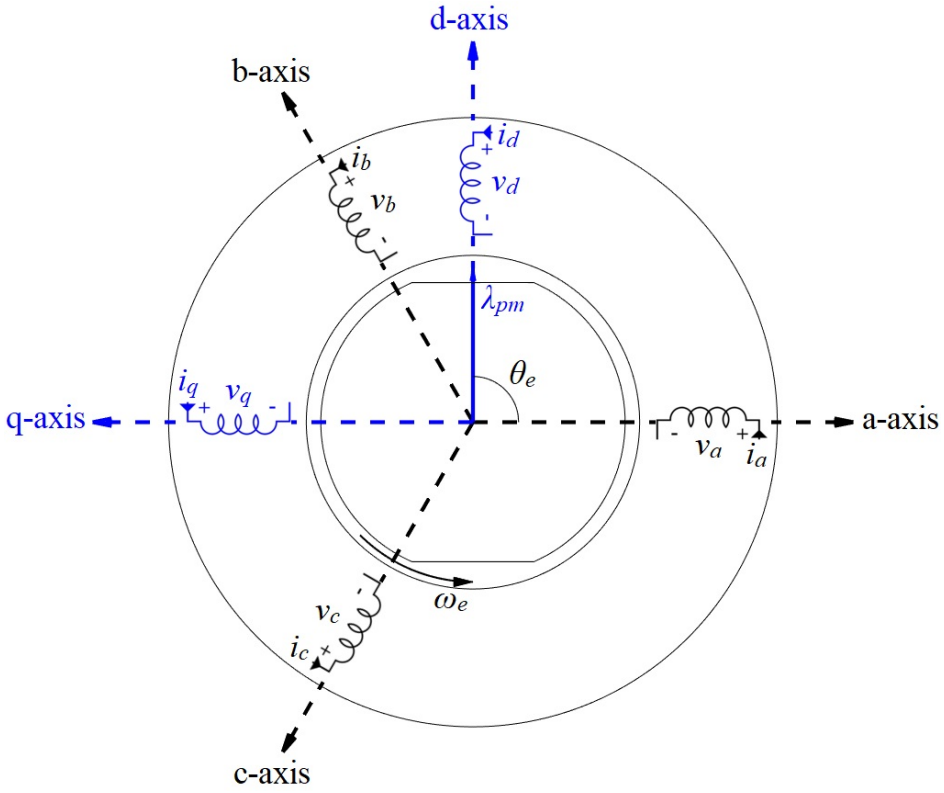

Figure 1.1: PMSM Parameters and Quantities

For a normal and optimized operation, v_s must be within the maximum voltage that the voltage-source converter can impose to the machine, which is based on the DC link voltage. At the same time, i_s must be within the machine's thermal and magnetic limits. Once the machine above a certain speed, most of the stator voltage will be used to compensate the machine's back-EMF, indicated by the terms multiplied by ω_e in the dq-frame voltages, meaning that a maximum torque operation can no longer be achieved. The currents once dedicated to torque production need to compensate for the excessive voltage generated by the machine, part of the current needs to be dedicated to weaken the rotor's magnetic field, thus not being able to produce torque. This is known as field weakening operation.

Some simplified solutions are proposed [16]–[19], however, even though simple and easy to implement, yielding good results, the results are not optimized.

The motivation for this research is to obtain a control algorithm for wide speed operation that can optimize the torque generation for every PMSM configuration, based on a "user input" that can request maximum motoring torque, no torque, maximum braking torque or anything in between.

A detailed problem formulation will be further discussed in Chapter 2.

1.2 Background

This chapter will consist in the theoretical background for the proposed wide-speed operation algorithms developed.

1.2.1 Rotating Reference Frame

Control theory dictates that a DC command can be effectively tracked with a simple Proportional-Integral (PI) Controller, however sinusoidal references need a dedicated controller tuned to have higher order and bandwidth, being able to track a single frequency [15]. In the classical abc-frame, when dealing with variable frequency drives (VFD), in which its fundamental frequency ranges continuously from DC up to a few kHz, designing a compensator that is able to track this reference is not a straightforward task. The αβ-frame and the dq-frame are introduced in this chapter to simplify the analysis and control that will be made in the following chapters.

The αβ-frame is used to transform a three-phase AC system in a two-phase AC system,

and the dq-frame is used to transform said system in a two-phase DC system. These frames are also called stationary reference frame and rotating reference frame, respectively.

Besides the advantage of using simple PI controllers to track DC references, the dq-frame also allows models of electric machines that exhibit time-varying mutually coupled inductances in the abc-frame to be simplified to constant parameters [15].

The transformation from the abc-frame to the αβ-frame is done via Clarke's Transform,

$$\begin{aligned}\begin{bmatrix} f_\alpha(t) \\ f_\beta(t) \end{bmatrix} &= \frac{2}{3}\boldsymbol{T_C} \begin{bmatrix} f_a(t) \\ f_b(t) \\ f_c(t) \end{bmatrix} \\ &= \frac{2}{3}\begin{bmatrix} 1 & -\frac{1}{2} & -\frac{1}{2} \\ 0 & \frac{\sqrt{3}}{2} & -\frac{\sqrt{3}}{2} \end{bmatrix} \begin{bmatrix} f_a(t) \\ f_b(t) \\ f_c(t) \end{bmatrix}\end{aligned} \tag{1.6}$$

$$\begin{aligned}\begin{bmatrix} f_a(t) \\ f_b(t) \\ f_c(t) \end{bmatrix} &= \frac{3}{2}\boldsymbol{T_C^{-1}} \begin{bmatrix} f_\alpha(t) \\ f_\beta(t) \end{bmatrix} \\ &= \frac{3}{2}\begin{bmatrix} 1 & 0 \\ -\frac{1}{2} & \frac{\sqrt{3}}{2} \\ -\frac{1}{2} & -\frac{\sqrt{3}}{2} \end{bmatrix} \begin{bmatrix} f_\alpha(t) \\ f_\beta(t) \end{bmatrix}\end{aligned} \tag{1.7}$$

The αβ-frame to the dq-frame tansmation can be done using Park's Transform, where $\varepsilon(t)$ is the angle between the d-axis and the a-axis:

$$\begin{aligned}\begin{bmatrix} f_d(t) \\ f_q(t) \end{bmatrix} &= \boldsymbol{T_P} \begin{bmatrix} f_\alpha(t) \\ f_\beta(t) \end{bmatrix} \\ &= \begin{bmatrix} \cos(\varepsilon(t)) & \sin(\varepsilon(t)) \\ -\sin(\varepsilon(t)) & \cos(\varepsilon(t)) \end{bmatrix} \begin{bmatrix} f_\alpha(t) \\ f_\beta(t) \end{bmatrix}\end{aligned} \tag{1.8}$$

$$\begin{aligned}\begin{bmatrix} f_\alpha(t) \\ f_\beta(t) \end{bmatrix} &= \boldsymbol{T_P^{-1}} \begin{bmatrix} f_d(t) \\ f_q(t) \end{bmatrix} \\ &= \begin{bmatrix} \cos(\varepsilon(t)) & -\sin(\varepsilon(t)) \\ \sin(\varepsilon(t)) & \cos(\varepsilon(t)) \end{bmatrix} \begin{bmatrix} f_d(t) \\ f_q(t) \end{bmatrix}\end{aligned} \tag{1.9}$$

The direct transformation from the abc-frame to the dq-frame, and its inverse operation, can be written as

$$\begin{bmatrix} f_d(t) \\ f_q(t) \end{bmatrix} = \frac{2}{3} \begin{bmatrix} \cos(\varepsilon(t)) & \cos\left(\varepsilon(t) - \frac{2\pi}{3}\right) & \cos\left(\varepsilon(t) - \frac{4\pi}{3}\right) \\ -\sin(\varepsilon(t)) & -\sin\left(\varepsilon(t) - \frac{2\pi}{3}\right) & -\sin\left(\varepsilon(t) - \frac{4\pi}{3}\right) \end{bmatrix} \begin{bmatrix} f_a(t) \\ f_b(t) \\ f_c(t) \end{bmatrix} \tag{1.10}$$

$$\begin{bmatrix} f_a(t) \\ f_b(t) \\ f_c(t) \end{bmatrix} = \frac{3}{2} \begin{bmatrix} \cos(\varepsilon(t)) & -\sin(\varepsilon(t)) \\ \cos\left(\varepsilon(t) - \frac{2\pi}{3}\right) & -\sin\left(\varepsilon(t) - \frac{2\pi}{3}\right) \\ \cos\left(\varepsilon(t) - \frac{4\pi}{3}\right) & -\sin\left(\varepsilon(t) - \frac{4\pi}{3}\right) \end{bmatrix} \begin{bmatrix} f_d(t) \\ f_q(t) \end{bmatrix} \tag{1.11}$$

with power given as

$$P(t) = \frac{3}{2} \left[v_d(t) i_d(t) + v_q(t) i_q(t) \right] \tag{1.12}$$

$$Q(t) = \frac{3}{2} \left[-v_d(t) i_q(t) + v_q(t) i_d(t) \right] \tag{1.13}$$

1.2.2 Three-Phase Voltage Source Converter

The three-phase voltage source converter (VSC) is a configuration of switching power devices that allows the conversion of a fixed DC voltage to an amplitude and frequency adjustable three-phase AC waveform [15][20]. It can be composed of several configurations of switching devices and have diverse control schemes to meet the criteria of a certain application. In the present research, the topology chosen is the two-level VSC, widely used for traction applications, having variable frequency and voltage magnitudes, to properly control the speed and torque of an electrical machine, both as a motor and as a generator. The schematic of this converter is seen in Figure 1.2.

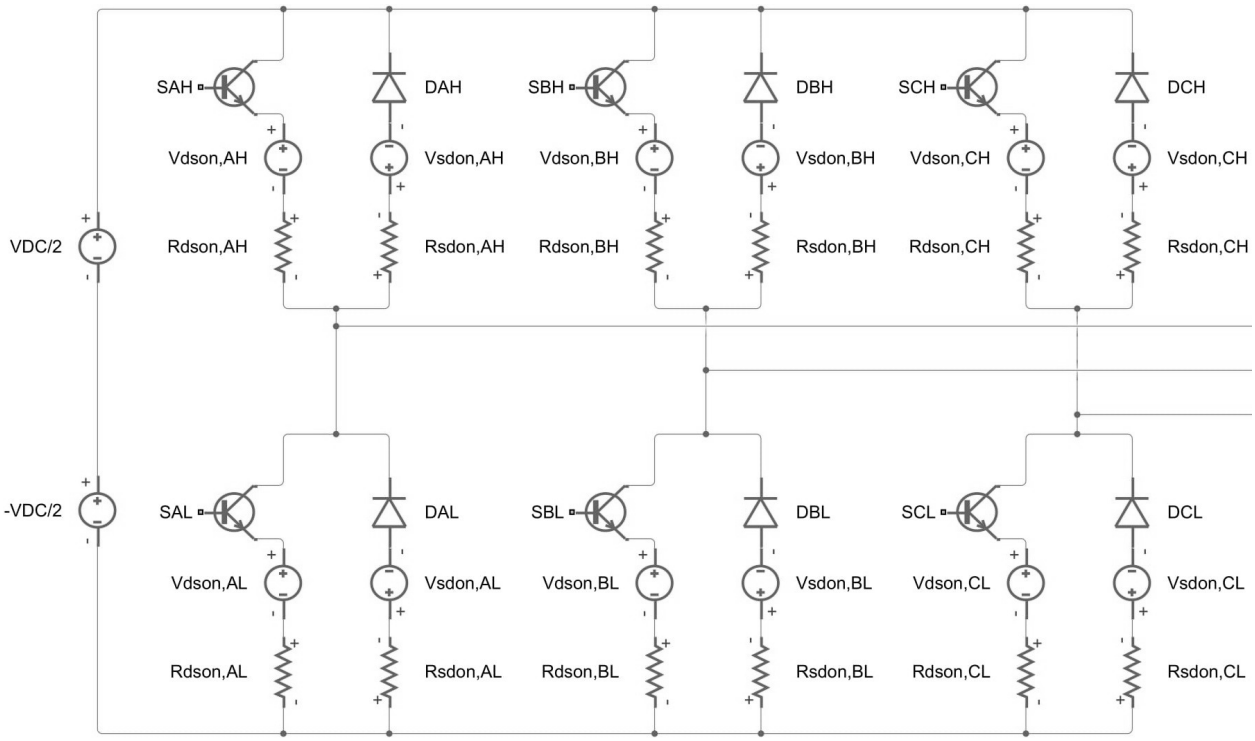

Figure 1.2: Model of a Non-Ideal Two-Level VSC

The two-level VSC is composed of three identical half-bridge converters, in which DC sides are connected in parallel with a common DC bus. For each half-bridge converter, their middle point – a terminal of the three-phase VSC – can be connected either to the voltage $V_{DC}/2$ or $-V_{DC}/2$, justifying the "two-level" designation [15].

In the rotating reference frame, with modulating signals $m_d(t)$ and $m_q(t)$, the terminal voltages of the VSC are given as

$$V_{td}(t) = \frac{V_{DC}}{2} m_d(t) \tag{1.14}$$

$$V_{tq}(t) = \frac{V_{DC}}{2} m_q(t) \tag{1.15}$$

In the same way as in the stationary reference frame, the model of the VSC in the rotating reference frame is also linear, with a gain of $V_{DC}/2$, as seen in Figure 1.3.

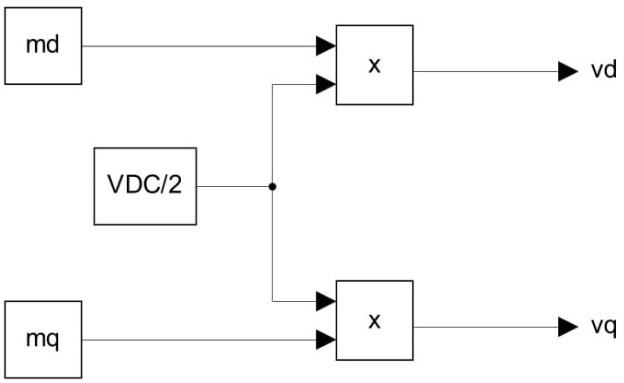

Figure 1.3: Model of the Three-Phase VSC in the dq-Frame

1.2.2.1 Space Vector Modulation

Section 1.2.2 presented a simple PWM technique that can be used to replicate a sinusoidal signal to the output of a VSC. However, there are other ways to realize the desired voltage than a simple comparison of the modulating signal with a triangular carrier. This section will present the most common modulation techniques used in digital control for two-level VSCs.

For three legs with two states each, there are eight states in which the VSC can operate, as seen in Figure 1.1. They will be referred to in the order of phases A, B and C, respectively. State "P" denotes the high-side switch is on (the middle point is connected to V_{DC}), and the state "O" indicates the low-side switch is closed (the middle point is connected to $0V$). For the eight states possible, [PPP] and [OOO] do not generate any voltage difference between phases, not forcing any current to the load. Therefore, they will be referred to as zero-states, while the other six will be referred to as active states [20].

Space Vector		Switching State	On-State Switches	Vector Definition
Zero Vector	$\vec{V}_0$	PPP	S_{AH}, S_{BH}, S_{CH}	$\vec{V}_0 = 0$
		OOO	S_{AL}, S_{BL}, S_{CL}	
Active Vector	$\vec{V}_1$	POO	S_{AH}, S_{BL}, S_{CL}	$\vec{V}_1 = 2/3 V_{DC} e^{j0}$
	$\vec{V}_2$	PPO	S_{AH}, S_{BH}, S_{CL}	$\vec{V}_2 = 2/3 V_{DC} e^{j\pi/3}$
	$\vec{V}_3$	OPO	S_{AL}, S_{BH}, S_{CL}	$\vec{V}_3 = 2/3 V_{DC} e^{j2\pi/3}$
	$\vec{V}_4$	OPP	S_{AL}, S_{BH}, S_{CH}	$\vec{V}_4 = 2/3 V_{DC} e^{j\pi}$
	$\vec{V}_5$	OOP	S_{AL}, S_{BL}, S_{CH}	$\vec{V}_5 = 2/3 V_{DC} e^{j4\pi/3}$
	$\vec{V}_6$	POP	S_{AH}, S_{BL}, S_{CH}	$\vec{V}_6 = 2/3 V_{DC} e^{j5\pi/3}$

Table 1.1: Space Vectors, Switching States and On-State Switches

The active and zero switching states are represented by active and zero space vectors, respectively. As shown in Figure 1.4, the six active vectors $\vec{V}_1$ to $\vec{V}_6$ form a hexagon with six equal sectors, noted as Sectors I to VI. The zero vector $\vec{V}_0$ lies in the center of the hexagon as it does not have a magnitude [20].

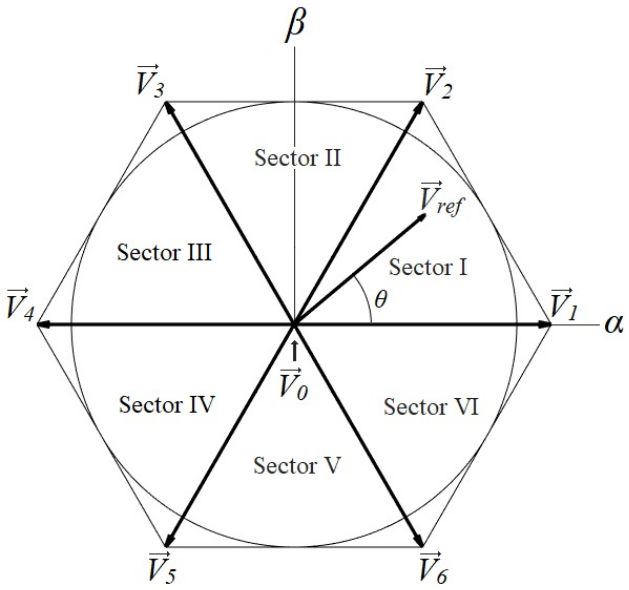

Figure 1.4: Space Vector Diagram for a Two-Level VSC

For any given voltage reference in the αβ-frame, it can be expressed in terms of the two active vectors that form the boundaries of the sector in which the reference is located and the zero vector. The dwell time for each stationary vector essentially represents the duty cycle of the chosen switches during a sampling time T_s. According to [20], the calculation of the dwell times is based on the volt-second balancing principle, in which the product of the reference $\vec{V}_{ref}$ and the sampling time T_s is equal to the sum of the voltage multiplied by the time of the chosen space vectors, and it is given by

$$\begin{cases} T_a = \dfrac{\sqrt{3}T_s V_{ref}}{V_{DC}} \sin\left(\dfrac{\pi}{3} - \theta\right) & (1.16) \\ T_b = \dfrac{\sqrt{3}T_s V_{ref}}{V_{DC}} \sin(\theta) & (1.17) \\ T_0 = T_s - T_a - T_b & (1.18) \end{cases}$$

where T_a is the time in which the clockwise-most active vector acts, T_b is the time in which

the counterclockwise-most active vector acts and T_0 is the time in which the zero vector acts. valid for $0 \leq \theta < \pi/3$, since $\vec{V}_{ref}$ is located on Sector I. With a $\vec{V}_{ref}$ that is closer to $\vec{V}_1$, it is expected that $T_a > T_b$. If the reference lies right between $\vec{V}_1$ and $\vec{V}_2$ (if $\theta = \pi/6$), $T_a = T_b$, and as the reference approaches $\vec{V}_2$, $T_a < T_b$. In the same manner, if $\vec{V}_{ref}$ lies over $\vec{V}_1$, $T_b = 0$, and it is analogous to the case where $\vec{V}_{ref}$ lies over $\vec{V}_2$, with the consequence of $T_a = 0$.

Even though all derivations so far were made for a case where $\vec{V}_{ref}$ is on Sector I, they can also be used for any other sector, as long as a multiple of $\pi/3$ is subtracted from θ:

$$\theta' = \theta - (k-1)\frac{\pi}{3} \tag{1.19}$$

for $0 \leq \theta' < \pi/3$ where $k = 1, 2, ..., 6$ for Sectors I, II, ..., VI, respectively [20].

It is also proved by [20] that the SVM technique also allows an increase of approximately 15.5% in the maximum output fundamental voltage, or more precisely, [21] demonstrates that a more precise value of $\hat{m}_{aug,a}(t)$ for $\hat{m}(t) = 1$ is $2/\sqrt{3}$, resulting in an increase of approximately 15.47% in the output voltage.

Once the vectors and the dwell times are defined, the sequence in which these vectors and times are applied need to be defined. The choice between different switching sequences is a trade-off between the number of switching actions in one cycle and the harmonic content of the output voltage, such as the 7-Segment Sequence (known as "Continuous SVM") and the 5-Segment Sequence (known as "Discontinuous SVM") [20].

Although not the only existent, the used modulation technique was presented in this chapter. Others can be used or even proposed depending on specific applications.

1.2.3 Permanent Magnet Synchronous Machines

Permanent magnet synchronous machines (PMSMs) are increasingly used in variable speed applications, including electric vehicles, due to their higher power density and efficiency when compared to cage rotor induction machines (CRIMs). According to [22], other benefits include no electrical energy used for magnetic field excitation, better dynamic performance, simplification of construction and maintenance and reduction of lifetime cost.

1.2.3.1 Configurations of PMSMs

The stator of a PMSM is essentially the same of a CRIM. Three-phase stator windings produce an approximately sinusoidal distribution of rotating magnetomotive force (MMF) in the air gap between the stator and the rotor. Even though there are many rotor configurations, PMSMs can be divided between surface permanent magnets (SPM) and interior permanent magnets (IPM).

Even though the distinction between SPM and IPM PMSMs suggests only a constructive difference, the definition is based on the relationship between L_d and L_q, which is a consequence of the rotor's configuration. The inductances in the dq-axes depend on the rotor geometry: a path for the magnetic flux consisting only in soft magnet material (with high permeability: rotor and stator cores) has a higher inductance than a path consisting in hard magnetic materials (with low permeability: permanent magnets) [23]. In this research, PMSMs with $L_d < L_q$ will be denoted as IPMSMs and PMSMs with $L_d = L_q$ will be denoted as SPMSMs. A rotor configuration where $L_d > L_q$ is not common and it will not be approached, although its control strategies can be easily obtained from the IPMSM case.

Opposite to radial-flux PMSMs are the axial-flux PMSMs, where the rotor and stator are discs, and their magnetic fluxes are in the axial direction.

Even though being clearly different constructive topologies, [23], [24] shows that the mathematical modelling is the same for both machine types. Therefore, all the mathematical derivations and control algorithms will be valid for both machines, and will not distinguish them.

1.2.3.2 Mathematical Modelling of a PMSM

For any rotor geometry, the flux linkage per phase in a PMSM is given by

$$\begin{bmatrix} \lambda_a \\ \lambda_b \\ \lambda_c \end{bmatrix} = \mathbf{L} \begin{bmatrix} i_a \\ i_b \\ i_c \end{bmatrix} + \begin{bmatrix} \lambda_{pm} \cos(\theta_e) \\ \lambda_{pm} \cos\left(\theta_e - \frac{2\pi}{3}\right) \\ \lambda_{pm} \cos\left(\theta_e - \frac{4\pi}{3}\right) \end{bmatrix} \tag{1.20}$$

where λ_{abc} is the stator flux linkage, i_{abc} is the stator current, θ_e is the rotor electrical angle and λ_{pm} is the maximum flux linkage generated by the rotor's permanent magnets in the stator windings [15]. As for $\boldsymbol{L}$, the inductance matrix, is given by

$$\mathbf{L} = \frac{2}{3}\begin{bmatrix} a\cos(2\theta_e)+b & a\cos\left(2\left(\theta_e-\frac{\pi}{3}\right)\right)-\frac{b}{2} & a\cos\left(2\left(\theta_e-\frac{2\pi}{3}\right)\right)-\frac{b}{2} \\ a\cos\left(2\left(\theta_e-\frac{\pi}{3}\right)\right)-\frac{b}{2} & a\cos\left(2\left(\theta_e-\frac{2\pi}{3}\right)\right)+b & a\cos(2\theta_e)-\frac{b}{2} \\ a\cos\left(2\left(\theta_e-\frac{2\pi}{3}\right)\right)-\frac{b}{2} & a\cos(2\theta_e)-\frac{b}{2} & a\cos\left(2\left(\theta_e-\frac{4\pi}{3}\right)\right)+b \end{bmatrix} \tag{1.21}$$

where a and b are constants given by

$$a = \frac{L_d - L_q}{2}$$
$$b = \frac{L_d + L_q}{2}$$

and L_d and L_q are the d- and q-axes inductances, respectively, that depend on the rotor geometry [15]. Equations (1.20) and (1.21) show that the stator windings exhibit a variable self-inductance in addition to their mutual inductances with respect to the other phases. According to [15], the flux and terminal voltages are related by

$$\frac{d}{dt}\begin{bmatrix}\lambda_a \\ \lambda_b \\ \lambda_c\end{bmatrix} = \begin{bmatrix}-R_s & 0 & 0 \\ 0 & -R_s & 0 \\ 0 & 0 & -R_s\end{bmatrix}\begin{bmatrix}i_a \\ i_b \\ i_c\end{bmatrix} + \begin{bmatrix}v_a \\ v_b \\ v_c\end{bmatrix} \tag{1.22}$$

where R_s is the stator winding resistance [15]. Equations (1.20)–(1.22) represent the model of a PMSM in the abc-frame. As mentioned in section 1.2.1, the machine model and control are facilitated in the rotating reference frame. Equation (1.20) is transformed to the $\alpha\beta$-frame using (1.7):

$$\boldsymbol{T_C}^T\begin{bmatrix}\lambda_\alpha \\ \lambda_\beta\end{bmatrix} = \boldsymbol{L}\boldsymbol{T_C}^T\begin{bmatrix}i_\alpha \\ i_\beta\end{bmatrix} + \begin{bmatrix}\lambda_{pm}\cos(\theta_e) \\ \lambda_{pm}\cos\left(\theta_e-\frac{2\pi}{3}\right) \\ \lambda_{pm}\cos\left(\theta_e-\frac{4\pi}{3}\right)\end{bmatrix} \tag{1.23}$$

That, according to [15], results in

$$\begin{bmatrix}\lambda_\alpha\\ \lambda_\beta\end{bmatrix} = \frac{2}{3}\boldsymbol{T_C}\boldsymbol{L}\boldsymbol{T_C}^T\begin{bmatrix}i_\alpha\\ i_\beta\end{bmatrix} + \frac{2}{3}\boldsymbol{T_C}\begin{bmatrix}\lambda_{pm}\cos(\theta_e)\\ \lambda_{pm}\cos\left(\theta_e-\frac{2\pi}{3}\right)\\ \lambda_{pm}\cos\left(\theta_e-\frac{4\pi}{3}\right)\end{bmatrix} \tag{1.24}$$

By substituting $\boldsymbol{T_C}$ and $\boldsymbol{L}$ in (1.24), it is possible to obtain

$$\begin{bmatrix}\lambda_\alpha\\ \lambda_\beta\end{bmatrix} = \begin{bmatrix}a\cos(2\theta_e)+b & a\sin(2\theta_e)\\ a\sin(2\theta_e) & -a\cos(2\theta_e)+b\end{bmatrix}\begin{bmatrix}i_\alpha\\ i_\beta\end{bmatrix} + \begin{bmatrix}\lambda_{pm}\cos(\theta_e)\\ \lambda_{pm}\sin(\theta_e)\end{bmatrix} \tag{1.25}$$

According to [15], following a similar procedure, it is possible to represent (1.22) as

$$\frac{d}{dt}\begin{bmatrix}\lambda_\alpha\\ \lambda_\beta\end{bmatrix} = \begin{bmatrix}-R_s & 0\\ 0 & -R_s\end{bmatrix}\begin{bmatrix}i_\alpha\\ i_\beta\end{bmatrix} + \begin{bmatrix}v_\alpha\\ v_\beta\end{bmatrix} \tag{1.26}$$

As already discussed in section 1.2.1, the αβ-frame still presents θ_e as a variable, and the analysis and control design of the machine is not an easy task. The transformation to the dq-frame facilitates the analysis, as long as the frame is synchronized to the rotor angle. This corresponds to $\varepsilon = \theta_e$ in (1.9) [15]. Therefore, it is possible to rewrite (1.25) as

$$\boldsymbol{T_P}^{-1}\begin{bmatrix}\lambda_d\\ \lambda_q\end{bmatrix} = \begin{bmatrix}a\cos(2\theta_e)+b & a\sin(2\theta_e)\\ a\sin(2\theta_e) & -a\cos(2\theta_e)+b\end{bmatrix}\boldsymbol{T_P}^{-1}\begin{bmatrix}i_d\\ i_q\end{bmatrix} + \begin{bmatrix}\lambda_{pm}\cos(\theta_e)\\ \lambda_{pm}\sin(\theta_e)\end{bmatrix} \tag{1.27}$$

Multiplying by $\boldsymbol{T_P}$ on both sides,

$$\begin{bmatrix}\lambda_d\\ \lambda_q\end{bmatrix} = \boldsymbol{T_P}\begin{bmatrix}a\cos(2\theta_e)+b & a\sin(2\theta_e)\\ a\sin(2\theta_e) & -a\cos(2\theta_e)+b\end{bmatrix}\boldsymbol{T_P}^{-1}\begin{bmatrix}i_d\\ i_q\end{bmatrix} + \boldsymbol{T_P}\begin{bmatrix}\lambda_{pm}\cos(\theta_e)\\ \lambda_{pm}\sin(\theta_e)\end{bmatrix} \tag{1.28}$$

that can be simplified to

$$\begin{bmatrix}\lambda_d\\ \lambda_q\end{bmatrix} = \begin{bmatrix}L_d & 0\\ 0 & L_q\end{bmatrix}\begin{bmatrix}i_d\\ i_q\end{bmatrix} + \begin{bmatrix}\lambda_{pm}\\ 0\end{bmatrix} \tag{1.29}$$

According to [15], (1.26) can be similarly rewritten as

$$\frac{d}{dt}\left(\boldsymbol{T_P}^{-1}\begin{bmatrix}\lambda_d\\ \lambda_q\end{bmatrix}\right) = \begin{bmatrix}-R_s & 0\\ 0 & -R_s\end{bmatrix}\boldsymbol{T_P}^{-1}\begin{bmatrix}i_d\\ i_q\end{bmatrix} + \boldsymbol{T_P}^{-1}\begin{bmatrix}v_d\\ v_q\end{bmatrix} \tag{1.30}$$

which can be rearranged as

$$\boldsymbol{T_P}^{-1}\frac{d}{dt}\begin{bmatrix}\lambda_d\\ \lambda_q\end{bmatrix} + \frac{d\boldsymbol{T_P}^{-1}}{dt}\begin{bmatrix}\lambda_d\\ \lambda_q\end{bmatrix} = \begin{bmatrix}-R_s & 0\\ 0 & -R_s\end{bmatrix}\boldsymbol{T_P}^{-1}\begin{bmatrix}i_d\\ i_q\end{bmatrix} + \boldsymbol{T_P}^{-1}\begin{bmatrix}v_d\\ v_q\end{bmatrix} \tag{1.31}$$

Furthermore, [15] shows that by multiplying both sides of (1.31) by $\boldsymbol{T_P}$ and substituting $\boldsymbol{T_P}$ and $\boldsymbol{T_P}^{-1}$ in the result, it can be concluded that

$$\frac{d}{dt}\begin{bmatrix}\lambda_d\\ \lambda_q\end{bmatrix} = \begin{bmatrix}0 & \omega_e\\ -\omega_e & 0\end{bmatrix}\begin{bmatrix}\lambda_d\\ \lambda_q\end{bmatrix} + \begin{bmatrix}-R_s & 0\\ 0 & -R_s\end{bmatrix}\begin{bmatrix}i_d\\ i_q\end{bmatrix} + \begin{bmatrix}v_d\\ v_q\end{bmatrix} \tag{1.32}$$

where the electrical angular speed can be related by the electrical angle by

$$\omega_e = \frac{d\theta_e}{dt} \tag{1.33}$$

According to [15], to derive an expression for the machine torque, the principle of power balance can be used. Based on (1.12), the power delivered to the machine is, in the matrix form,

$$P_e = \frac{3}{2}\begin{bmatrix} i_d \\ i_q \end{bmatrix}^T \begin{bmatrix} v_d \\ v_q \end{bmatrix} \tag{1.34}$$

Substituting the values obtained for v_{dq} obtained in (1.32) into (1.34), we have

$$P_e = \frac{3}{2}\begin{bmatrix} i_d \\ i_q \end{bmatrix}^T \left(\begin{bmatrix} R_s i_d \\ R_s i_q \end{bmatrix} + \frac{d}{dt}\begin{bmatrix} \lambda_d \\ \lambda_q \end{bmatrix} + \begin{bmatrix} -\omega_e \lambda_q \\ \omega_e \lambda_d \end{bmatrix} \right) \tag{1.35}$$

which can be simplified to

$$P_e = \underbrace{\frac{3}{2} R_s \left(i_d^2 + i_q^2\right)}_{P_{loss}} + \underbrace{\frac{3}{2}\left(i_d \frac{d\lambda_d}{dt} + i_q \frac{d\lambda_q}{dt}\right)}_{P_{stored}} + \underbrace{\frac{3}{2}\omega_e \left(\lambda_d i_q - \lambda_q i_d\right)}_{P_{gap}} \tag{1.36}$$

The first term of (1.36) represents the ohmic loss in the stator windings. The second term indicates the power stored in the machine's magnetic field, which can be also negative, indicating power being released. The third and last term indicates the power being delivered to the air gap of the machine, which is responsible for the electrical torque generated [15]. Therefore,

$$T_e = \frac{P_{gap}}{\omega_e} = \frac{3}{2}\left(\lambda_d i_q - \lambda_q i_d\right) \tag{1.37}$$

Replacing λ_{dq} from (1.29) into (1.37), it is possible to finally obtain

$$T_e = \underbrace{\frac{3}{2}\left(L_d - L_q\right) i_d i_q}_{T_{rel}} + \underbrace{\frac{3}{2}\lambda_{pm} i_q}_{T_{pm}} \tag{1.38}$$

The first term of (1.38) indicates the reluctance torque, the torque generated by the

saliency of the rotor. It is zero if $L_d = L_q$, which is the case for a surface-mounted magnets machine, and does not depend on the flux of the permanent magnets. The second term is the magnetic torque, the torque generated by the permanent magnets of the machine.

According to [15], equations (1.29), (1.32) and (1.38) constitute the dq-frame model for the PMSM. Since the dq-frame is synchronized to the rotor angle θ_e, the model presented is also the same as the PMSM model in rotor-field coordinates. As the equations mentioned indicate, the dq-frame model of a PMSM is time-invariant since all parameters are constant, but it is nonlinear, due to the presence of products of the state variables in the equations.

1.2.4 Current Control of Permanent Magnet Synchronous Machines in the Rotating Reference Frame

1.2.4.1 Introduction

As presented in section 1.2.3.2, the model of a PMSM in the dq-frame, in which the d-axis is aligned with the magnetic flux generated by the permanent magnets – thus being called "rotor-field coordinates" –, can be summarized by the following sets of equations:

$$\lambda_d = L_d i_d + \lambda_{pm} \tag{1.39}$$

$$\lambda_q = L_q i_q \tag{1.40}$$

$$v_d = -\omega_e \lambda_q + R_s i_d + \frac{d\lambda_d}{dt} \tag{1.41}$$

$$v_q = \omega_e \lambda_d + R_s i_q - \frac{d\lambda_q}{dt} \tag{1.42}$$

$$T_e = \frac{3}{2}\left(L_d - L_q\right) i_d i_q + \frac{3}{2}\lambda_{pm} i_q \tag{1.43}$$

An illustration for the rotor-field coordinates was already shown in Figure 1.1, in which the direct axis of the PMSM is the direction of its rotor magnetic flux.

The mechanical angular position, angular speed, torque and power are related to their

electrical counterparts by the number of pole pairs p_p of the machine, and are given by

$$\theta_m = \frac{\theta_e}{p_p} \tag{1.44}$$

$$\omega_m = \frac{\omega_e}{p_p} \tag{1.45}$$

$$T_m = p_p T_e \tag{1.46}$$

$$P_m = T_m \omega_m \tag{1.47}$$

There is no consensus between authors if the letter p indicates the number of poles or pole pairs of the machine (the first accompanied by a /2 factor in the equations), generating confusion between sources. Therefore, to avoid misunderstandings, the notation p_p for the pole pairs will be used in this research, although not often employed by other literature.

The equation that dictates the angular acceleration of a rotating system is given by

$$\frac{d\omega_m}{dt} = \frac{T_m - T_{load}}{J_m} \tag{1.48}$$

where T_{load} is the opposing torque generated by the mechanical load and J_m is the system moment of inertia. The load torque from a rotating body can be modelled by [25] as

$$T_{load} = \sqrt{2e}\,(T_{brk} - T_C)\, e^{-\left(\frac{\omega_m}{\omega_{St}}\right)^2} \frac{\omega_m}{\omega_{St}} + T_C \tanh\left(\frac{\omega_m}{\omega_{Coul}}\right) + f\omega_m \tag{1.49}$$

where T_C is the Coulomb friction torque, T_{brk} is the breakaway friction torque, ω_{brk} is the breakaway friction velocity, ω_{St} is the Stribeck velocity threshold, ω_{Coul} is the Coulomb velocity threshold and f is the viscous friction coefficient. The graphical interpretation for (1.49) can be seen in Figure 1.5.

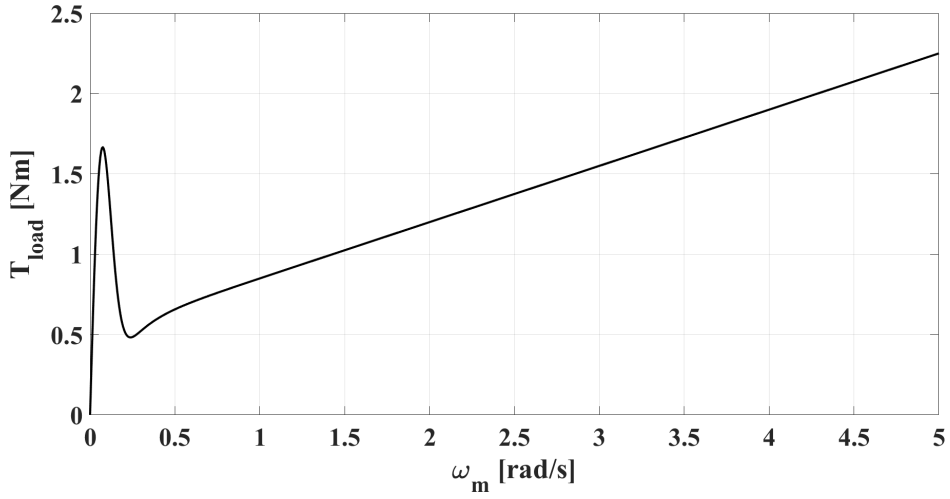

Figure 1.5: Simplified Model of a Friction Torque from a Rotational Load

1.2.4.2 Current Control in Rotor-Field Coordinates

The equations presented in section 1.2.4.1 showed the machine torque being a function of its currents, and it is advised to control them, since it is possible to perform an independent control [15].

To control i_d and i_q, (1.39)–(1.40) are substituted in (1.41)–(1.42), resulting in

$$L_d \frac{di_d}{dt} = v_d - R_s i_d \underbrace{+\omega_e L_q i_q}_{\text{q-axis coupling}} \tag{1.50}$$

$$L_q \frac{di_q}{dt} = v_q - R_s i_q \underbrace{-\omega_e L_d i_d - \omega_e \lambda_{pm}}_{\text{d-axis coupling}} \tag{1.51}$$

which can also be visualized as two electrical circuits, shown in Figure 1.6.

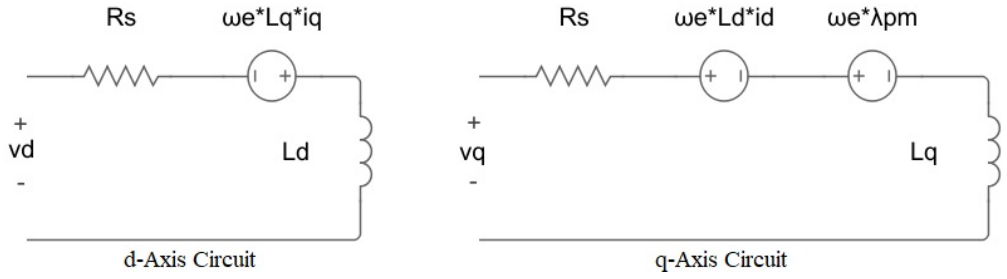

Figure 1.6: Electrical Model of a PMSM in Rotor-Field Coordinates

It is possible to notice in (1.50)–(1.51) that there is a contribution of q-axis quantities in the d-axis model, and contributions of d-axis quantities in the q-axis model. These voltages indicate that the axes are not decoupled. However, since the mentioned contributions can be easily calculated, they will be removed in a feedforward compensation.

According to [15], by introducing two new control variables

$$u_d = v_d + \omega_e L_q i_q \tag{1.52}$$

$$u_q = v_q - \omega_e L_d i_d - \omega_e \lambda_{pm} \tag{1.53}$$

it is possible to simplify (1.50)–(1.51) as

$$L_d \frac{di_d}{dt} + R_s i_d = u_d \tag{1.54}$$

$$L_q \frac{di_q}{dt} + R_s i_q = u_q \tag{1.55}$$

Equations (1.54)–(1.55) show two decoupled, first-order, single input single output (SISO) subsystems. Therefore, two independent control loops can be created to ensure that i_d and i_q will follow their respective references, $i_{d,ref}$ and $i_{q,ref}$ [15], as shown in Figure 1.7.

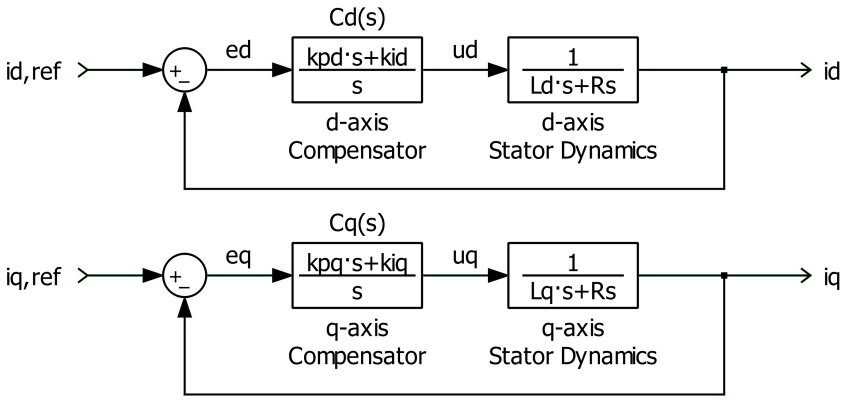

Figure 1.7: Current Control Loops

It is also possible to notice in Figure 1.7 that the d-axis compensator $C_d(s)$ processes the error $e_d = i_{d,ref} - i_d$ and commands $v_{d,ref}$. Similarly, the q-axis compensator $C_q(s)$

processes the error $e_q = i_{q,ref} - i_q$ and commands $v_{q,ref}$. According to [15], assuming that the closed-loop transfer functions ${}^{I_d(s)}/_{I_{d,ref}(s)}$ and ${}^{I_q(s)}/_{I_{q,ref}(s)}$ are of the first order with a time constant τ_i, it is possible to write

$$C_d(s) = \frac{k_{pd}s + k_{id}}{s} \tag{1.56}$$

$$C_q(s) = \frac{k_{pq}s + k_{iq}}{s} \tag{1.57}$$

where k_{pd} is the proportional gain in the d-axis, k_{id} is the integral gain in the d-axis, k_{pq} is the proportional gain in the q-axis and k_{iq} is the integral gain in the q-axis, which can be given by

$$k_{pd} = \frac{L_d}{\tau_i} \qquad k_{pq} = \frac{L_q}{\tau_i} \qquad k_{id} = k_{iq} = \frac{R_s}{\tau_i} \tag{1.58}$$

Since the motor will be driven by a VSC, it is shown by [15] that the on-state resistance of the semiconductor switches in the converter can be modelled as being part of the load. Therefore, to take these nonidealities into consideration by the control system,

$$k_{pd} = \frac{L_d}{\tau_i} \qquad k_{pq} = \frac{L_q}{\tau_i} \qquad k_{id} = k_{iq} = \frac{R_s + 2R_{on}}{\tau_i} \tag{1.59}$$

It is also discussed by [15] that the time constant τ_i should be around ten times higher (*i.e.* slower) than the switching frequency of the VSC, in radians per second. Therefore,

$$\tau_i = \frac{10}{2\pi f_{sw}} \tag{1.60}$$

Even though it is possible to obtain the control parameters by root locus analysis and Bode Plots for phase margin calculation [26], (1.59)–(1.60) are able to quickly produce

satisfactory results, being suitable for simulations and implementations of several different machines.

According to [15], to implement the control with the axes-decoupling, $v_{d,ref}$ and $v_{q,ref}$ must be determined from u_d and u_q based in (1.52)–(1.53), respectively:

$$v_{d,ref} = u_d - \omega_e L_q i_q \tag{1.61}$$

$$v_{q,ref} = u_q + \omega_e L_d i_d + \omega_e \lambda_{pm} \tag{1.62}$$

and it is illustrated in the block diagram in Figure 1.8.

The references $v_{d,ref}$ and $v_{q,ref}$ are then processed to generate the gate signals for the VSC in which the machine is connected to. By using modulation techniques based on the abc-frame, such as the SPWM, the Inverse Park Transformation and the Inverse Clarke Transformation must be done to transform $v_{dq,ref}$ into $v_{abc,ref}$. For modulations based on the αβ-frame, such as SVM, just the Inverse Park Transformation is done to obtain $v_{\alpha\beta,ref}$.

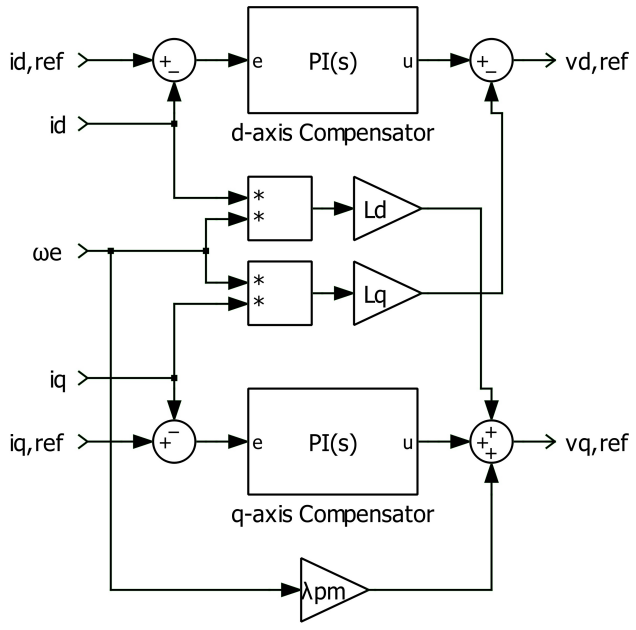

Figure 1.8: Current Control in Rotor-Field Coordinates with Axes-Decoupling

1.3 Objective and Contribution

The objective of this research is to develop a wide speed control algorithm for PMSMs, independently of its configuration, that can be implemented in a digital signal processor (DSP) without requiring a high performance device. Said control algorithm has the goal of optimizing the torque-per-current ratio when in field-weakening, when the current needs to be dedicated to not only generate torque, but to weaken the permanent magnets, taking into consideration the limits imposed by the DC bus voltage and current capability of the system. This optimization shall also be able to operate in all four torque-speed quadrants (*i.e.* forward and backward movement with forward or backward torque, thus implying in both motoring and regenerative braking operations) under a variable input from the operator, including a no torque (also known as "coasting") operation for any operating speed.

This research will also provide an analysis of the torque and power profiles for each PMSM and how a per-unit command can be given to the control system.

1.4 Thesis Structure

After the present chapter, the thesis will have as its main objective developing the optimal current vector placement for PMSMs. It will consist of the author's approach for this research. From the two rotor configurations (surface and internal permanent magnets) and two speed concepts (finite and a theoretically infinite speed), it will be defined four PMSM cases.

- **Chapter 1** consists in the introduction and motivation for the thesis. Background for the development of the wide-speed control of PMSMs. Rotating Reference Frame (RRF) theory, including its mathematical transformations. Three-phase Voltage Source Converters (VSCs) and modulation techniques in the dq-frame. Permanent Magnet Synchronous Machines configurations, constructions and mathematical modelling. Current Control of PMSMs in the RRF. Objective and contribution.

- **Chapter 2** will be the main chapter of this thesis, where all the development and mathematical analysis of the algorithms will happen. Wide Speed Control of the four PMSM cases (surface and internal PMSMs with finite and a theoretically infinite speed operation), including a discussion regarding the in theory infinite speed operation.

Reference current generation. Complete control system. Study of undervoltage and overcurrent operation of PMSM and the impacts on the torque and power profiles of the machine. Impacts of the stator resistance. Practical considerations regarding machine saturation, demagnetization and overheating.

- **Chapter 3** will present the simulation results for the algorithms developed in Chapter 3 for all four PMSM cases defined. Four torque-speed quadrants operation and zero torque operation. Torque and power profiles.
- **Chapter 4** will present the experimental results for a small-scale PMSM.
- **Chapter 5** will be the conclusion of the thesis, as well as a future work to further improve the research presented.

Chapter 2

Wide Speed Operation of Permanent Magnet Synchronous Machines

2.1 Introduction

Section 1.2.4 discussed how the machine currents will follow the desired references, and with the techniques presented, this can be guaranteed. The problem now lies in how these references are generated. This will be done in an algorithm called "reference currents generator" from now on.

First, the considerations and objectives need to be clarified for this task:

- The reference currents generator will have three inputs:
  - A per-unit command from the EV driver/rider, ranging from -1 to +1: from maximum backwards torque to maximum forward torque, including a zero reference of "no torque produced" – also known as "coasting"
  - The machine's speed, to define the machine's operating region and properly calculate the reference currents
  - The DC link voltage, to define the maximum voltage that can be applied to the machine
- The reference currents generator will have two outputs: $i_{d,ref}$ and $i_{q,ref}$, that will be imposed to the machine by a chosen current control method aforementioned
- The reference currents generator will produce its outputs in such a way that the machine's desired torque needs only an optimized amount of voltage and current

- The reference currents generator will not produce its outputs in such a way that forces the machine to operate under overvoltage and/or overcurrent
- The reference currents generator will be created in a DSP-friendly format, having in mind a practical implementation
- The reference currents generator will be able to operate in all the four torque-speed quadrants

The algorithm responsible to generate the references will also take into consideration if the machine is operating below or above its rated speed – also known as base speed, $\omega_{e,base}$ – and the rotor geometry.

For convenience, it is defined the machine's characteristic current as

$$I_{ch} = \frac{\lambda_{pm}}{L_d} \tag{2.1}$$

and the machine's saliency ratio as

$$\xi = \frac{L_q}{L_d} \tag{2.2}$$

Having in mind the torque presented in (1.43) and the electric to mechanical conversion shown in (1.46), it is possible, according to [27] to rewrite the machine's mechanical torque as

$$T_m = \frac{3p_p}{2}\left(L_d - L_q\right) i_d i_q + \frac{3p_p}{2}\lambda_{pm} i_q \tag{2.3}$$

$$= \frac{3p_p L_d}{2}\left[-(\xi - 1) i_d i_q + I_{ch} i_q\right] \tag{2.4}$$

Each of the two terms of (2.4) has a useful physical interpretation, such as presented in (1.38): the first term is the reluctance torque, a torque that is proportional to both i_d and

i_q and the machine's saliency ratio ξ. The second term is the magnetic torque, and it is in quadrature to the magnetic flux generated by the permanent magnets, being proportional to the said flux magnitude and the current i_q.

Although (2.4) is valid for both rotor geometries, the reluctance torque is zero for surface permanent magnets PMSMs, and the second term vanishes. It is noted by [27] that the fact of the reluctance torque being zero for surface permanent magnets PMSMs ($L_d = L_q$) does not denote its inferiority in comparison to internal permanent magnets PMSMs ($L_d < L_q$). The torque and power densities, along with other figures of merit of PMSMs depend on several other constructive factors.

For IPM PMSMs, for both torques to have the contribution towards the same rotational direction, i_d must be negative: otherwise, the reluctance torque would be opposing the magnetic torque.

In order to better visualize the torque production characteristics, it is helpful to use the dq current plane in the rotating reference frame. It can be seen in Figure 2.1.

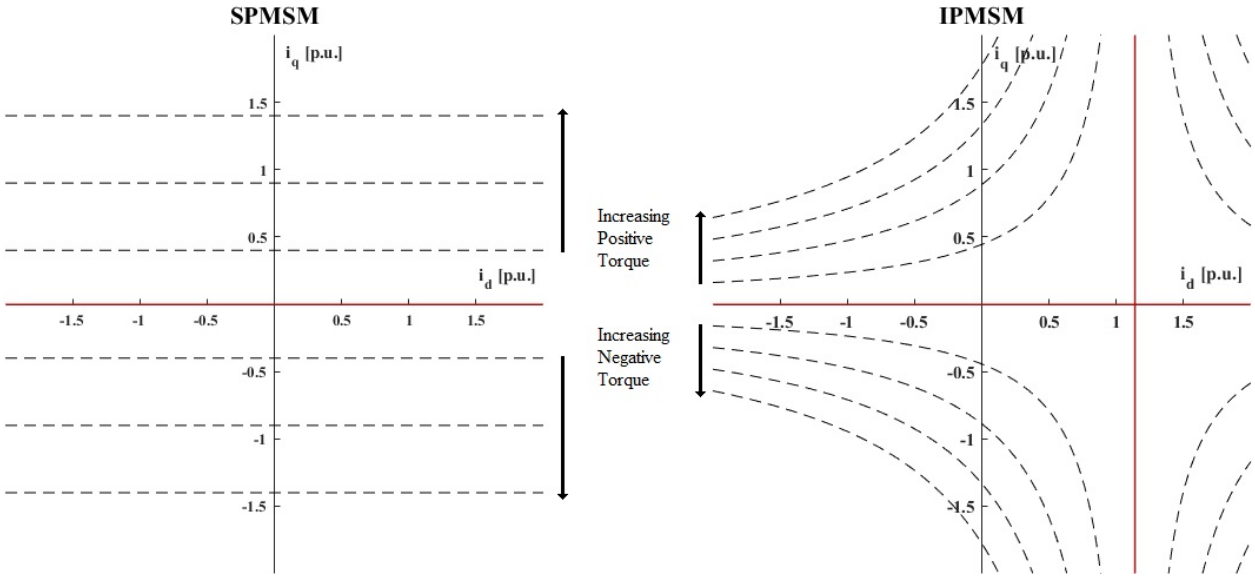

Figure 2.1: Constant-Torque Loci for a PMSM in the dq-Frame

Fugue 2.1 shows several constant-torque lines, represented in dashed black, for both rotor geometries being considered. Any stator current vector i_s terminating on the same constant-torque line will deliver the same torque [27].

For SPMSMs, the constant-torque lines are parallel to the d-axis, and indicate that i_d does not have an impact on torque generation, which is confirmed by (2.3) when $L_d = L_q$

or by (2.4) when $\xi = 1$. The torque is zero if the current vector is located along the d-axis (*i.e.* $i_q = 0$), represented in red. It is also noted that positive values of i_q produce a positive torque, and for negative values of i_q, the machine produces a negative torque.

For an IPMSM, the torque curves have hyperbolic shapes due to the $i_d i_q$ product term that appears in the torque equations (2.3)–(2.4). Another difference with respect to the SPM machines is that there are two lines for zero torque. One is along the d-axis ($i_q = 0$) and the other is parallel to the q-axis, defined by $i_d = {}^{\lambda_{pm}}/_{L_q - L_d}$, represented in red. This represents the case in which the magnetic torque is cancelled by the reluctance torque [27]. Since it is in the region of $i_d > 0$, and it was already mentioned that i_d must be negative to have both torques working together instead of against each other, the machine operation in that line is not a concern.

As stated in one of the objectives for the reference currents generator algorithm, maximizing torque while minimizing the stator current helps to achieve the best performance of the machine while keeping the ohmic losses in the stator as low as possible. This is referred to as Maximum Torque per Ampère (MTPA) operation, and it is valid for both SPM and IPM machines [15][20][27].

The algorithm will consist in generating a current trajectory along the dq-plane to satisfy all the objectives. This will define $i_s = \sqrt{i_d^2 + i_q^2}$ for a desired torque and for any speed of the machine. This is illustrated in Figure 2.2 for a general case, with a current trajectory is predefined based on the machine's parameters, and the stator current i_s follows the trajectory for three instants of time. For each i_s, there is a single combination of i_d and i_q, which are the output of the algorithm.

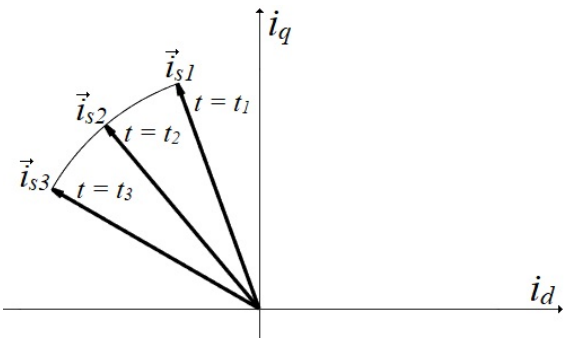

Figure 2.2: Illustration of Current Trajectory

Since it was also defined that the algorithm should not force the machine to operate

under overcurrent, it is defined a current limit circle, in which $i_{s,max} = 1p.u.$ Therefore, since $i_s \leq i_{s,max}$, the vector i_s should be inside of the said circle, represented in blue in Figure 2.3.

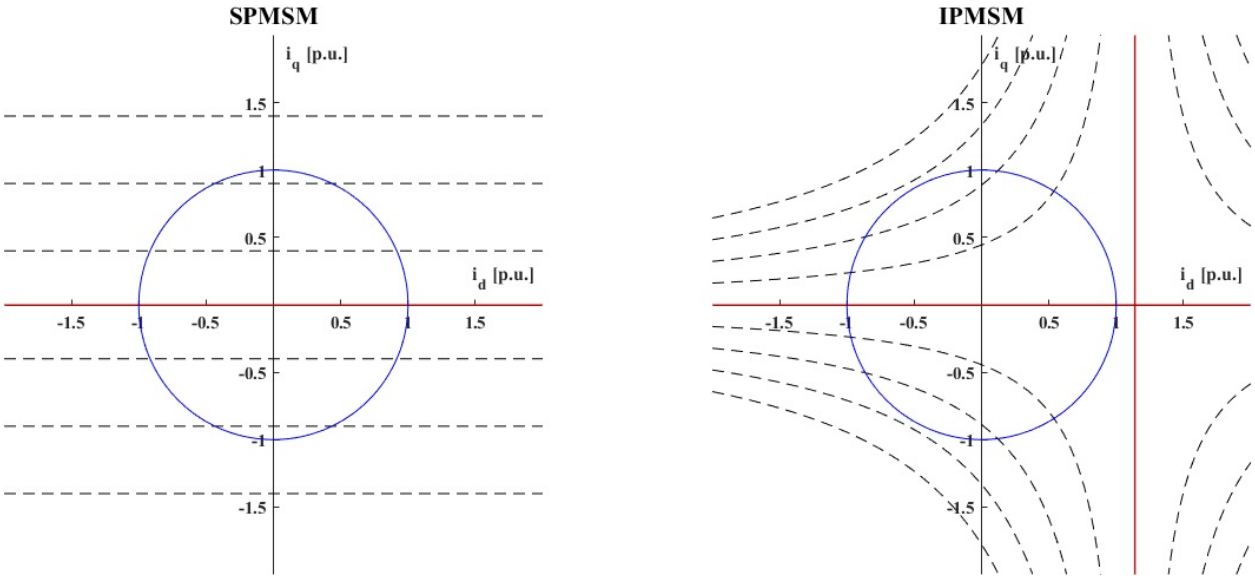

Figure 2.3: Current Limit Circle for a PMSM in the dq-Frame

2.2 Below Base Speed: Maximum Torque per Ampère

For a PMSM operating in a speed $\omega_m \leq \omega_{base}$, the maximum machine torque can be developed at any speed. Figure 2.4 shows the MTPA trajectories, represented in green, for both SPM and IPM machines.

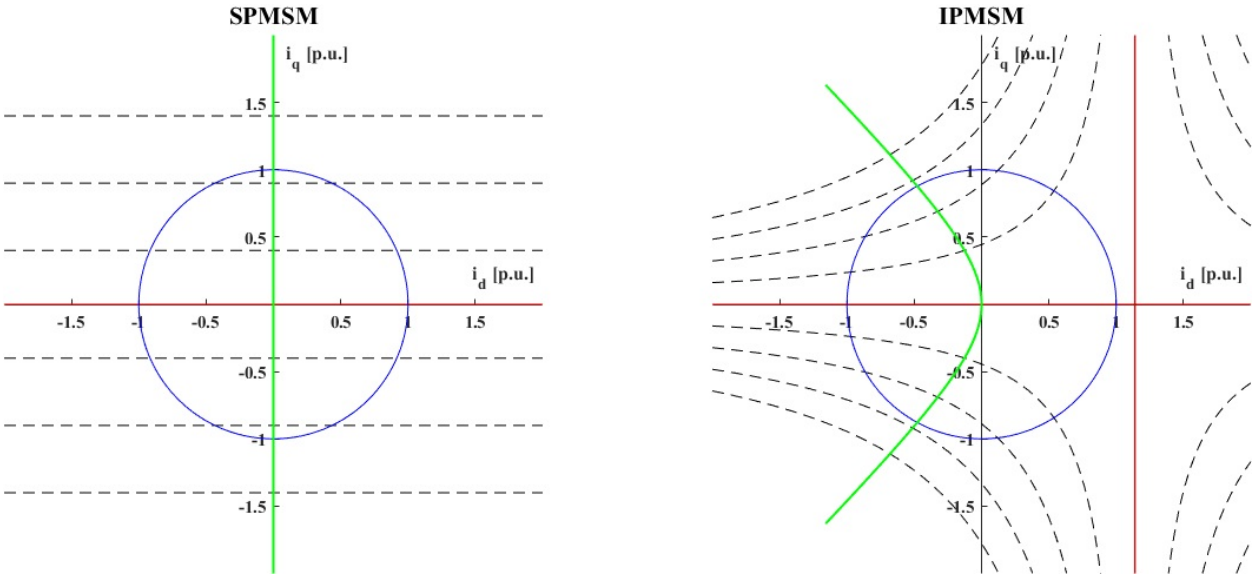

Figure 2.4: Maximum Torque per Ampère Trajectories

2.2.1 SPMSM

For an SPMSM, since i_d does not create any torque, its MTPA trajectory is straightforward: the torque is controlled only via a q-axis current. Since the objective is to reduce the stator current i_s, i_d is constant at zero. This is also referred to by some as Zero d-Axis Current (ZDC).

Therefore, for an SPMSM, the torque equation becomes

$$\text{SPMSM} \begin{cases} T_m = \dfrac{3p_p}{2}\lambda_{pm} i_q \end{cases} \tag{2.5}$$

Where all the stator current is at the q-axis (*i.e.* $i_q = i_s$). Therefore, the MTPA algorithm will be given by

$$\begin{matrix} \text{SPMSM} \\ \text{MTPA} \end{matrix} \begin{cases} i_{d,ref} = 0 \\ i_{q,ref} = i_{s,ref} \end{cases} \tag{2.6}$$

2.2.2 IPMSM

For an IPMSM, the torque equation is not simplified, and remains in its original form shown in (2.3), and the task of obtaining the MTPA algorithm is not straightforward. For convenience, it is defined the torque angle β, which is the angle between the stator current i_s and the d-axis – or the permanent magnet flux.

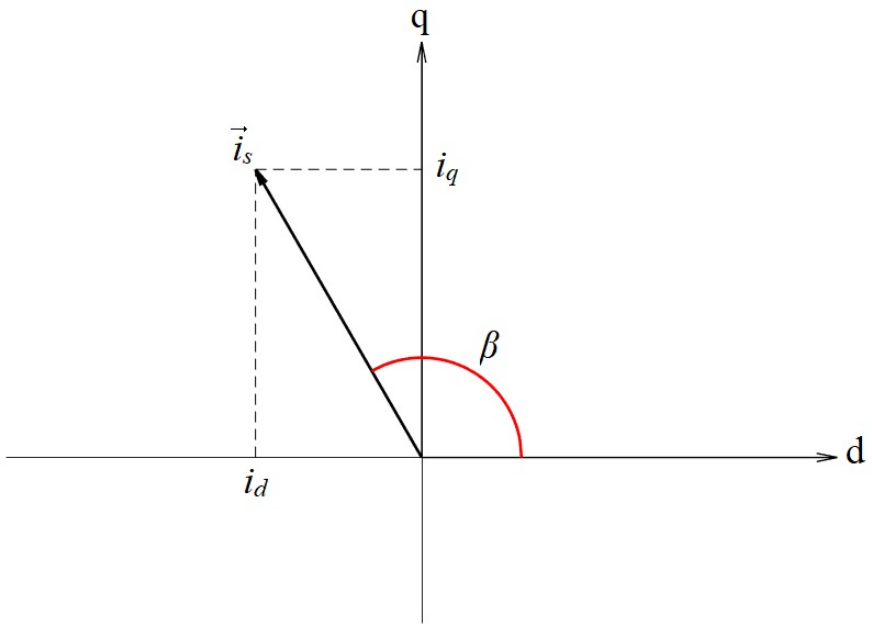

Figure 2.5: Torque Angle Definition

With $i_d = i_s \cos(\beta)$ and $i_q = i_s \sin(\beta)$, it is possible to rewrite (2.3) as

$$T_m = \frac{3p_p}{2}(L_d - L_q) i_s \cos(\beta) i_s \sin(\beta) + \frac{3p_p}{2}\lambda_{pm} i_s \sin(\beta) \tag{2.7}$$

or, with aid of trigonometric identities,

$$T_m = \frac{3p_p}{2}(L_d - L_q) i_s^2 \frac{\sin(2\beta)}{2} + \frac{3p_p}{2}\lambda_{pm} i_s \sin(\beta) \tag{2.8}$$

The first term of (2.8) remains the reluctance torque and the second, the magnetic torque. For illustration purposes, Figure 2.6 shows each torque mentioned and the total torque for an IPMSM whose parameters are seen in Table 2.1 [28], by setting the stator current as its maximum value.

IPMSM Parameters	
L_d	$171\mu H$
L_q	$391\mu H$
λ_{pm}	$103.9mWb$
p_p	6
$i_{s,max}$	$570A$

Table 2.1: Parameters for IPMSM Example

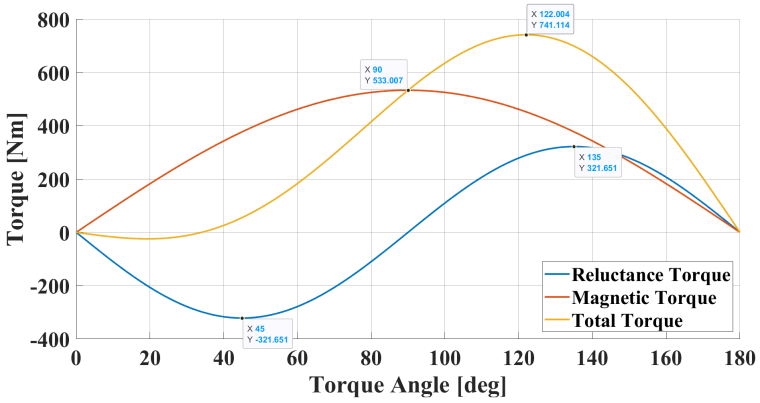

Figure 2.6: Reluctance, Magnetic and Total Torques for the IPMSM Example

It is noticeable in Figure 2.6 that the magnetic torque peaks at 90°, as expected, and the reluctance torque is zero at that angle. The reluctance torque has its negative peak at 45°and positive peak at 135°, and from 0°to 90°, it opposes the magnetic torque, while from 90°to 180°it collaborates with it. Therefore, the total torque peaks at an angle higher than 90°. In this example, the peak torque is $741.114Nm$ for $\beta = 122.004°$.

To determine for which β the total torque peaks, it is simply a matter of deriving T_m with respect to β and equating it to zero.

$$\frac{dT_m}{d\beta} = \frac{3p_p}{2}(L_d - L_q)i_s^2\cos(2\beta) + \frac{3p_p}{2}\lambda_{pm}i_s\cos(\beta) = 0 \tag{2.9}$$

that can be written as

$$(L_d - L_q)\left((i_s\cos(\beta))^2 - (i_s\sin(\beta))^2\right) + \lambda_{pm}i_s\cos(\beta) = 0 \tag{2.10}$$

Since $i_s \cos(\beta) = i_d$ and $i_s \sin(\beta) = i_q$, (2.10) can be expressed as

$$(L_d - L_q)(i_d^2 - i_q^2) + \lambda_{pm} i_d = 0 \tag{2.11}$$

and using the vectorial sum properties, it is possible to use $i_q = \sqrt{i_s^2 - i_d^2}$, resulting in

$$-(L_d - L_q) i_s^2 + 2(L_d - L_q) i_d^2 + \lambda_{pm} i_d = 0 \tag{2.12}$$

It is noticeable that (2.12) is a quadratic function of i_d. Using Bhaskara's Formula, it is possible to identify two solutions for (2.12):

$$\begin{cases} i_{d1} = \dfrac{\lambda_{pm} + \sqrt{\lambda_{pm}^2 + 8(L_q - L_d)^2 i_s^2}}{4(L_q - L_d)} > 0 \\ i_{d2} = \dfrac{\lambda_{pm} - \sqrt{\lambda_{pm}^2 + 8(L_q - L_d)^2 i_s^2}}{4(L_q - L_d)} < 0 \end{cases} \tag{2.13}$$

Since IPM machines are considered to have $L_q > L_d$, to obtain a positive reluctance torque for $90° < \beta < 180°$, i_d must be negative. Therefore, the second solution of (2.13) is adopted for $i_{d,ref}$ in the MTPA algorithm of an IPMSM. As for $i_{q,ref}$, it is simply obtained from the decomposition of $i_{s,ref}$ into the dq-axes, multiplied by the sign of $i_{s,ref}$, to allow regenerative braking.

$$\begin{matrix} \text{IPMSM} \\ \text{MTPA} \end{matrix} \begin{cases} i_{d,ref} = \dfrac{\lambda_{pm} - \sqrt{\lambda_{pm}^2 + 8(L_q - L_d)^2 i_{s,ref}^2}}{4(L_q - L_d)} \\ i_{q,ref} = \text{sgn}(i_{s,ref}) \sqrt{i_{s,ref}^2 - i_{d,ref}^2} \end{cases} \tag{2.14}$$

It is noted that the torque angle $\beta = \arctan(i_q/i_d)$ does not depend only of the machine's parameters, but also the stator current magnitude. Therefore, the MTPA trajectory for an

IPMSM is not a straight line.

Using the example from Figure 2.6, the currents $i_{d,ref}$ and $i_{q,ref}$ are calculated based in (2.14) for $i_{s,ref}$ changing continuously from $0A$ to $570A$, and plotted in the dq-plane, along with the current limiting circle (CLC). The result can be seen in Figure 2.7. Even though all calculations and examples so far considered the machine acting in the motoring region, the equations are also valid for the generating region, setting $i_{s,ref}$ as a negative value, yielding a negative torque with a maximum value equal to the torque in the motoring region.

It is verified in the example of Figure 2.6, for a stator current amplitude of $570A$, the algorithm results in reference currents that, when applied to the machine, give a torque of $741.114Nm$, the maximum obtainable torque.

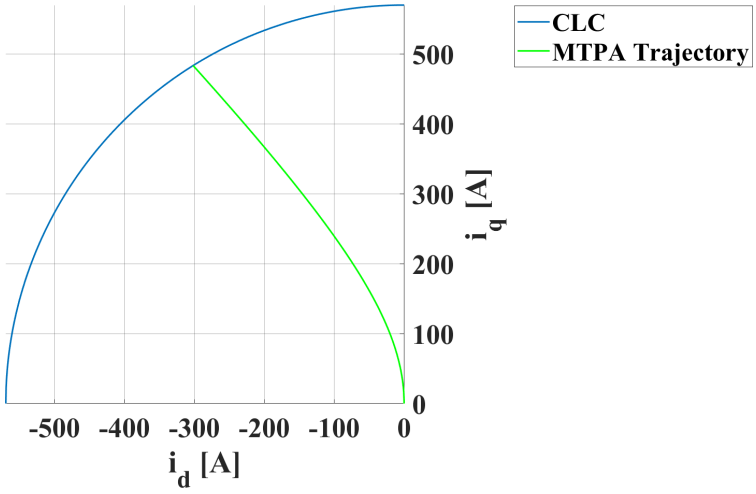

Figure 2.7: MTPA Trajectory for the IPMSM Example

2.3 Above Base Speed: Voltage and Current Limited Maximum Torque

Equations (1.41) and (1.42) can be manipulated to give the dq-axis voltages as

$$v_d = -\omega_e \lambda_q + R_s i_d + \frac{d\lambda_d}{dt} \tag{2.15}$$

$$v_q = \omega_e \lambda_d + R_s i_q + \frac{d\lambda_q}{dt} \tag{2.16}$$

By expanding the magnetic fluxes in the dq-frame using (1.39)–(1.40),

$$v_d = -\omega_e \left(L_q i_q\right) + R_s i_d + L_d \frac{di_d}{dt} \tag{2.17}$$

$$v_q = \omega_e \left(L_d i_d + \lambda_{pm}\right) + R_s i_q + L_q \frac{di_q}{dt} \tag{2.18}$$

Considering a steady state operation, and neglecting the stator resistance R_s – which will have its contribution considered in another moment –, it is possible to simplify the dq-frame voltages as

$$v_d = -\omega_e L_q i_q \tag{2.19}$$

$$v_q = \omega_e L_d i_d + \omega_e \lambda_{pm} \tag{2.20}$$

Since the stator voltage is given by the vectorial sum of v_d and v_q,

$$v_s = \sqrt{v_d^2 + v_q^2} \tag{2.21}$$

it can be written in terms of the variables ω_e, i_d and i_q as

$$v_s = \sqrt{\left(\omega_e L_q i_q\right)^2 + \left(\omega_e L_d i_d + \omega_e \lambda_{pm}\right)^2} \tag{2.22}$$

It is possible to see through (2.22) that the machine voltage is not only dependent on the currents, but also from its speed. Since the VSC acts as a step-down converter when inverting, the voltage on its AC side is limited by the voltage on its DC side. This implies that, for an increasing speed of the machine, the VSC will have to increase its modulation indices. However, once the machine reaches a speed in which the VSC will have its modulation indices at maximum, it cannot be further accelerated, since the converter cannot apply more voltage in its AC side. If no proper measures are taken and the control is

forced to do so, this will result in an overmodulation operation, having a nonlinear distorted response, which will likely compromise the system stability without having the machine's speed increased significantly.

Rewriting (2.22) to give ω_e results in

$$\omega_e = \frac{v_s}{\sqrt{\left(L_q i_q\right)^2 + \left(L_d i_d + \lambda_{pm}\right)^2}} \tag{2.23}$$

Hence, it is defined the based speed, $\omega_{e,base}$, that dictates the maximum speed of the machine that can be obtained with the maximum output voltage of the VSC with the MTPA algorithms presented so far, and it is given by

$$\omega_{e,base} = \frac{v_{s,max}}{\sqrt{\left(L_q i_{q,max}\right)^2 + \left(L_d i_{d,max} + \lambda_{pm}\right)^2}} \tag{2.24}$$

where $i_{d,max}$ and $i_{q,max}$ are the dq-axis currents obtained for the maximum value of the stator current $i_{s,max}$ according to the MTPA algorithms presented so far.

It is worth mentioning that the base speed may or may not be the same as the machine's rated speed, which definition depends on its manufacturer.

While for the MTPA algorithms, valid for below the base speed, the only constraint was the stator current i_s, above the base speed there will also be a constraint regarding the stator voltage v_s.

Therefore, for this range of speed, a new algorithm must be defined. They are called Field-Weakening (FW) algorithms, due to the fact that they will focus on maintaining the back-EMF of the machine constant with an increasing speed by reducing the air gap flux. To reduce the flux generated by the permanent magnets, the algorithm will create a negative d-axis current.

It is important to have in mind that the MTPA algorithm gives a combination of $i_{dq,ref}$ to obtain the maximum torque possible. Once a FW algorithm is implemented and changes the current vector, the torque will decrease, since the focus is to maximize the torque with

another limiting factor. From (2.22) it is possible to derive

$$\left(\frac{i_d + I_{ch}}{v_s/\omega_e L_d}\right)^2 + \left(\frac{i_q}{v_s/\omega_e L_q}\right)^2 = 1 \tag{2.25}$$

where $v_s \leq v_{s,max}$. Since it is still desired the maximum performance of the machine, for a case where $v_s = v_{s,max}$, (2.25) defines a voltage ellipse in the id-iq plane, centred in the point $(i_d = -I_{ch}, i_q = 0)$, with a semi-major axis (also denoted as "horizontal axis") radius of $v_s/\omega_e L_d$, and a semi-minor axis (also denoted as "vertical axis") radius of $v_s/\omega_e L_q$. For better usage of the DC bus voltage, it is desired to fix $v_s = v_{s,max}$. For a current vector i_s located in the ellipse border, the reference currents generated will be such as $v_s = v_{s,max}$, while a current vector inside the ellipse will cause a $v_s \leq v_{s,max}$. By fixing $v_s = v_{s,max}$, the ellipse radii are a function of ω_e. $v_{s,max}$ can be defined as a function of the DC bus voltage as

$$v_{s,max} = \begin{cases} \dfrac{V_{DC}}{\sqrt{3}} - R_s i_{s,max} & \text{for SPWM} \\ \dfrac{2V_{DC}}{3} - R_s i_{s,max} & \text{for SVM} \end{cases} \tag{2.26}$$

For the case where $L_d = L_q$, the ellipse becomes a circle. Therefore, for an SPMSM the voltage-limiting circle reduces its radius as ω_e increases, as seen in Figure 2.8, whereas for an IPMSM, the voltage-limiting ellipse, as seen in Figure 2.9 has the same behaviour. For both figures, $\omega_{e1} < \omega_{e2} < \omega_{e3}$.

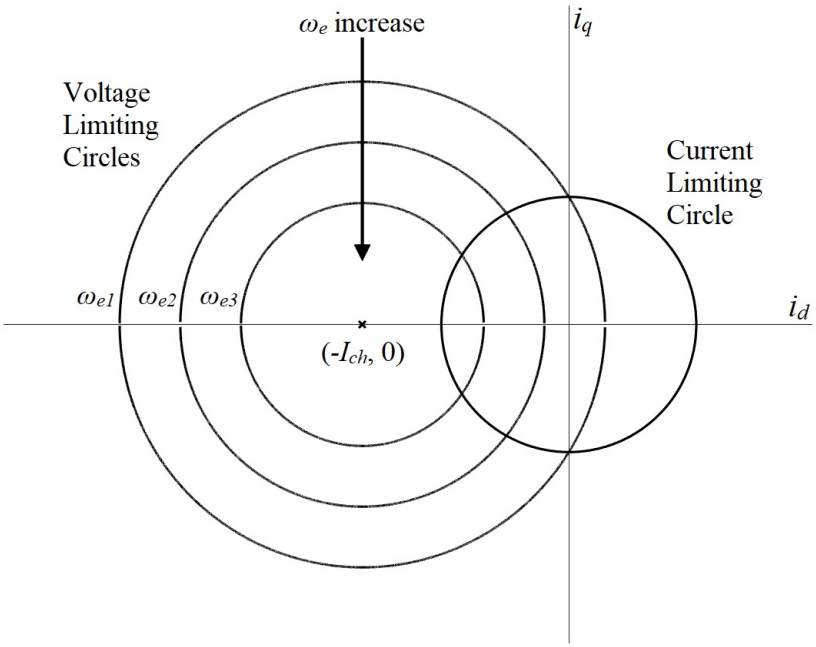

Figure 2.8: Voltage-Limiting Circles for an SPMSM

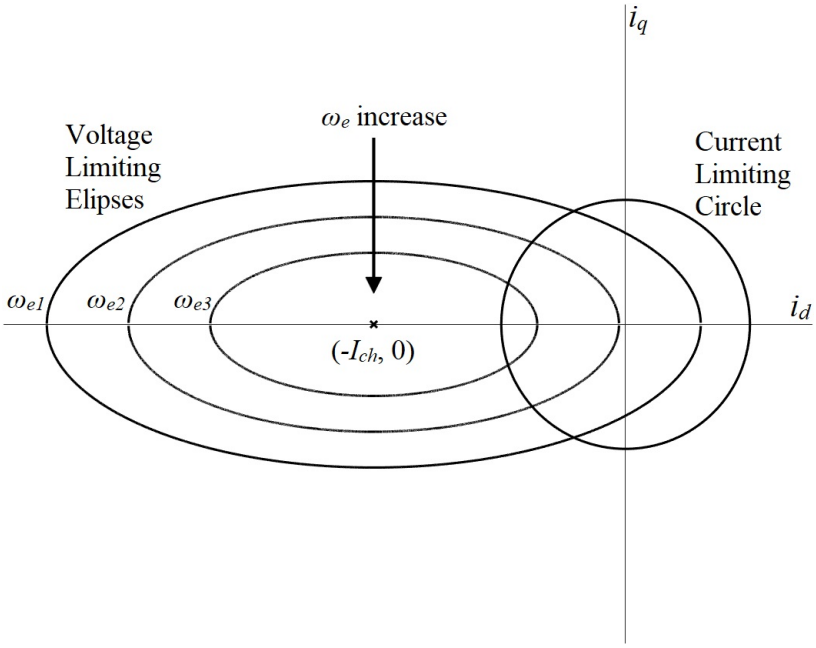

Figure 2.9: Voltage-Limiting Ellipses for an IPMSM

Therefore, the reference current vector $i_{s,ref}$ must be inside or at both the current-limiting circle and the voltage-limiting circle/ellipse to satisfy the current and voltage constraints, respectively. It is also worth mentioning that the voltage-limiting circle/ellipse for the base speed intersects the current-limiting circle in the MTPA point for the maximum current.

Even though Figures 2.8 and 2.9 illustrate a case where $I_{ch} > i_{s,max}$, it is possible to have a case where the circle/ellipse is centered at $(-I_{ch}, 0)$ where $I_{ch} < i_{s,max}$, although not common, since the magnetic flux created by the permanent magnets in modern machines has a large intensity, enough to create a very high characteristic current.

There are some simplified FW algorithms, as studied by [16]–[19], such as the Constant Voltage Constant Power (CVCP) and the Constant Current Constant Power (CCCP). Their names clearly show their purposes. Since the CVCP and CCCP does not limit the machine's current and voltage, respectively, for some speeds the machine will enter in an overcurrent and overvoltage modes of operation, respectively, and for others, the maximum voltages and currents are not be applied, meaning that more torque could be obtained. Although the most complex, the VCLMT is the one that is able to satisfy the voltage and current limits of the machine, and it will be the one studied in this project.

The VCLMT algorithm will be composed by four cases: SPMSM and IPMSM, and each for a case where $I_{ch} > i_{s,max}$ and another for $I_{ch} < i_{s,max}$.

2.3.1 Case 1: SPMSM with $I_{ch} > i_{s,max}$

For illustration purposes, it will be defined a numerical example for a machine fitted in Case 1. It is based on Kollmorgen's AKM 54K-ANCN2-00, and its parameters can be seen in Table 2.2.

SPMSM Case 1	
R_s	$540m\Omega$
L_d	$3.1mH$
L_q	$3.1mH$
λ_{pm}	$150.64mWb$
p_p	5
V_{DC}	$640V$
$i_{s,max}$	$9.7\sqrt{2}A$

Table 2.2: Parameters for Case 1

Based on the machine's data, it is possible to plot its MTPA trajectory, current limiting circle (CLC) and voltage-limiting circle (VLC) for the base speed, based in (2.24) and (2.25), and it is seen in Figure 2.10.

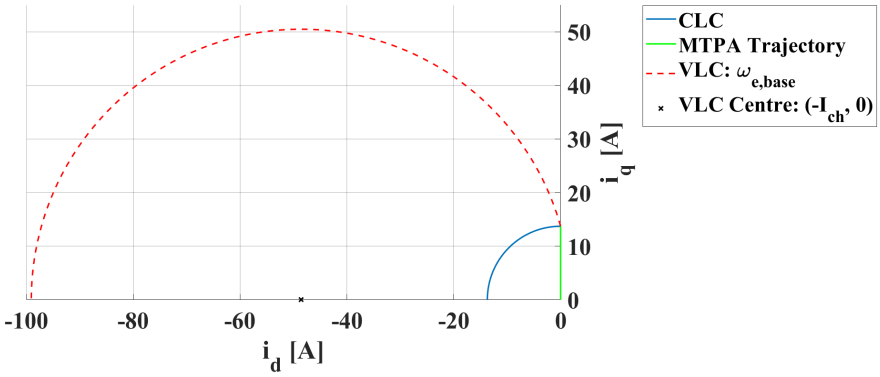

Figure 2.10: Case 1 MTPA, CLC and Base Speed VLC

The base speed dictates the boundary for voltage-limited operation: below the base speed, any point along the MTPA trajectory lies within the VLC. This will be denoted as "Trajectory 1" and its algorithm is given by

$$\begin{array}{r} \text{Case 1} \\ \text{Trajectory 1} \\ \\ \text{MTPA} \end{array} \begin{cases} |\omega_e| \leq \omega_{e,base} \\ 0 \leq |i_{s,ref}| \leq i_{s,max} \\ i_{d,ref} = 0 \\ i_{q,ref} = i_{s,ref} \end{cases} \tag{2.27}$$

The MTPA trajectory for speeds equal to or below the base speed is seen in Figure 2.11.

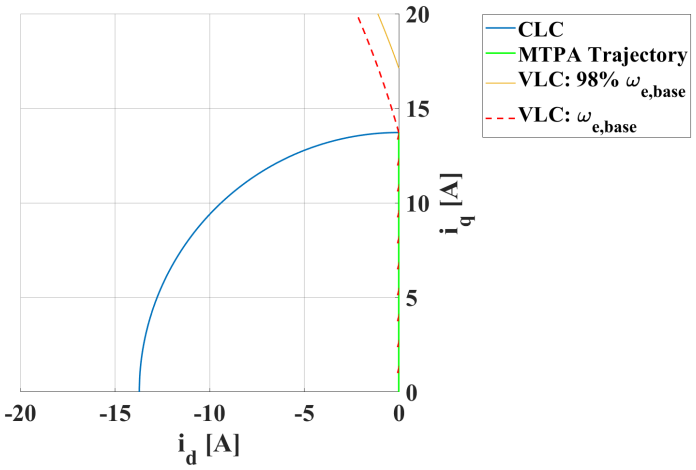

Figure 2.11: Case 1 MTPA Trajectory

However, this is not true for speeds above the base speed, as seen in Figure 2.12.

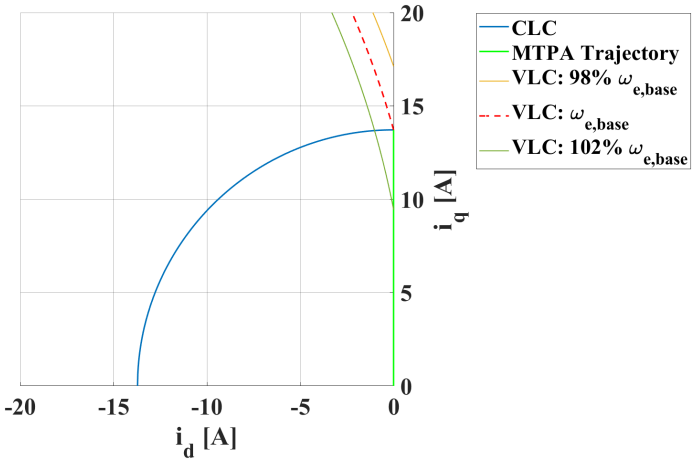

Figure 2.12: Case 1 MTPA, CLC and VLCs

Therefore, for a speed range slightly above the base speed, only a portion of the MTPA trajectory is valid. For a stator current i_s below a certain value, the MTPA trajectory can still be used, and above said value, the trajectory followed must be the VLC itself. This value will be named "cutoff current", and denoted by $i_{s,cut}$, and it is seen in Figure 2.13.

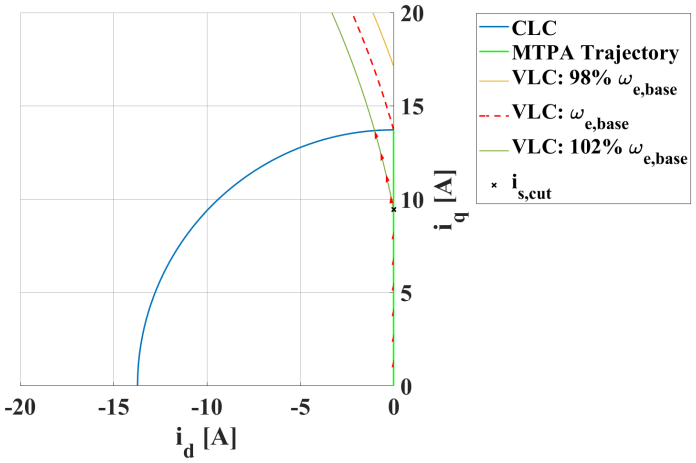

Figure 2.13: Case 1 Cutoff Current

The cutoff current can be defined as the stator current vector that is located at the point in which the voltage-limiting ellipse and the MTPA trajectory intercept each other. Even though (2.25) is in the implicit form, it is possible to solve for i_q by considering only the positive half of the ellipse, which gives

$$i_{q,VLC} = \frac{v_{s,max}}{|\omega_e| L_d} \sqrt{1 - \left(\frac{i_{d,VLC} + I_{ch}}{v_{s,max}/\omega_e L_d} \right)^2} \tag{2.28}$$

Since $i_{d,cut} = 0$, and, due to the fact that the cutoff current still satisfies the MTPA algorithm, $i_{s,cut} = i_{q,cut}$. Therefore, (2.28) can be simplified to

$$i_{s,cut} = \frac{v_{s,max}}{|\omega_e| L_d} \sqrt{1 - \left(\frac{\omega_e \lambda_{pm}}{v_{s,max}} \right)^2} \tag{2.29}$$

With an increasing machine speed, the cutoff current will be reduced, until the point that it will be located at the origin. This can be seen in Figure 2.14, where it can be noticed that $i_{s,cut} = i_{s,max}$ for the base speed, and $i_{s,cut} = 0$ for a certain speed. The speed in which this occurs will be named "critical speed", and denoted by $\omega_{e,crit}$.

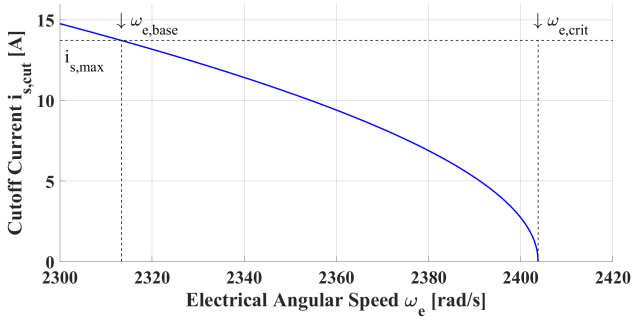

Figure 2.14: Case 1 Cutoff Current

For speeds below the base speed, $i_{s,cut} > i_{s,max}$, however it is worth mentioning that for said speed range the algorithm does not use $i_{s,cut}$, therefore the highest value for $i_{s,cut}$ is $i_{s,max}$, which occurs at $|\omega_e| = \omega_{e,base}$.

The critical speed is the highest speed in which part of the MTPA trajectory is still valid, which is only the origin. For speeds higher than or equal it, the reference current vector should follow only the voltage-limiting circle, and the MTPA is not valid for any reference current vector magnitude. For $|\omega_e| = \omega_{e,crit}$, the voltage-limiting ellipse intercepts the origin of the system. Therefore, its semi-major axis radius (also known as horizontal radius) is equal to the distance between the origin and its center:

$$\frac{v_{s,max}}{\omega_{e,crit} L_d} = I_{ch} \tag{2.30}$$

that yields, with aid from (2.1),

$$\omega_{e,crit} = \frac{v_{s,max}}{\lambda_{pm}} \tag{2.31}$$

The value for $\omega_{e,crit}$ from (2.31) could also be obtained from (2.29) by solving for ω_e with $i_{s,cut} = 0$. The VLC for the critical speed can be seen in Figure 2.15.

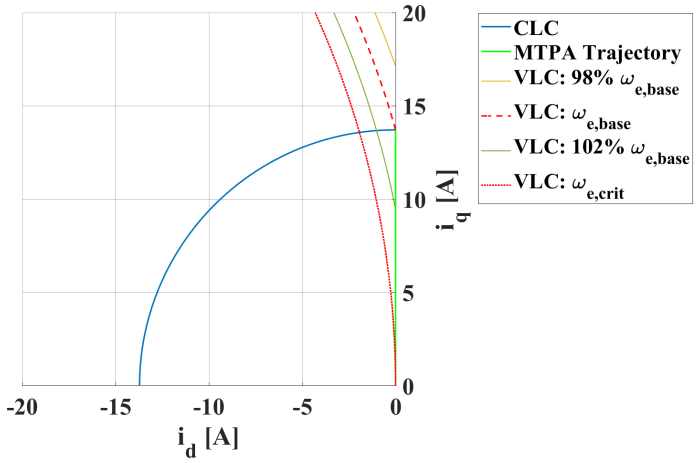

Figure 2.15: Case 1 Critical Speed

For a speed that lies in the range $\omega_{e,base} \leq |\omega_e| \leq \omega_{e,crit}$, the current trajectory will follow the MTPA trajectory from the origin up to $i_{s,cut}$, then follow the VLC up to $i_{s,max}$. To obtain the algorithm for operation at the VLC, it is substituted $i_{q,ref} = \sqrt{i_{s,ref}^2 - i_{d,ref}^2}$ into the VLC equation, resulting in

$$i_{d,ref} = -\frac{i_{s,ref}^2}{2I_{ch}} + \frac{v_{s,max}^2}{2\lambda_{pm} L_d \omega_e^2} - \frac{I_{ch}}{2} \tag{2.32}$$

This will define the operating trajectories 2 and 3 which algorithms are

$$\text{Case 1}\\ \text{Trajectory 2}\\ \text{VCLMT}\begin{cases}\omega_{e,base} \leq |\omega_e| \leq \omega_{e,crit}\\ 0 \leq |i_{s,ref}| \leq i_{s,cut}\\ i_{d,ref} = 0\\ i_{q,ref} = i_{s,ref}\end{cases} \tag{2.33}$$

$$\text{Case 1}\\ \text{Trajectory 3}\\ \text{VCLMT}\begin{cases}\omega_{e,base} \leq |\omega_e| \leq \omega_{e,crit}\\ i_{s,cut} \leq |i_{s,ref}| \leq i_{s,max}\\ i_{d,ref} = -\dfrac{i_{s,ref}^2}{2I_{ch}} + \dfrac{v_{s,max}^2}{2\lambda_{pm}L_d\omega_e^2} - \dfrac{I_{ch}}{2}\\ i_{q,ref} = \text{sgn}(i_{s,ref})\sqrt{i_{s,ref}^2 - i_{d,ref}^2}\end{cases} \tag{2.34}$$

Trajectory 2 can be interpreted as the MTPA trajectory that is still inside of the VLC, and for the same speed, Trajectory 3 is the VLC that needs to be followed since the MTPA for a current higher than the cutoff lies outside the VLC.

For a speed $|\omega_e| > \omega_{e,crit}$, the current trajectory should follow only the VLC. It is also noticeable that, for said speed range, said trajectory does not include the origin anymore. This implies that the current reference range is not $0 \leq |i_{s,ref}| \leq i_{s,max}$ anymore: its lower limit cannot be zero. It is defined the reference stator current lower limit, denoted as $i_{s,lowlim}$, and it can be seen in Figure 2.16.

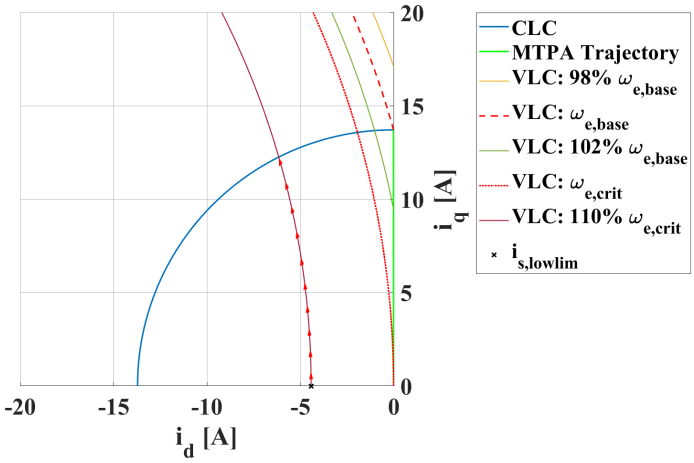

Figure 2.16: Case 1 Above Critical Speed

The lower limit for the stator current reference $i_{s,lowlim}$ can be calculated as the distance between the origin and the point in which the VLC intercepts the d-axis. Knowing the horizontal radius for the VLC,

$$i_{s,lowlim} = I_{ch} - \frac{v_{s,max}}{|\omega_e| L_d} \tag{2.35}$$

The lower limit for the stator current reference $i_{s,lowlim}$ can be seen in Figure 2.17.

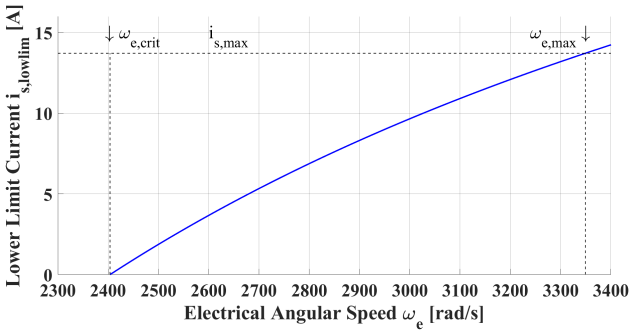

Figure 2.17: Case 1 Lower Limit Current

It is noticed in Figure 2.17 that $i_{s,lowlim} = 0$ for the critical speed, which denotes that the origin can still be used as a reference for said speed, and increases for an increasing speed, until it reaches $i_{s,lowlim} = i_{s,max}$ in a certain speed. This speed will be named "maximum speed", denoted as $\omega_{e,max}$.

In the case where $I_{ch} > i_{s,max}$ can be interpreted as a machine with permanent magnets so strong that there will be a speed in which even the maximum current being dedicated to demagnetize them will not be enough to counter the induced voltage by the permanent magnets. With an increasing speed, the machine will reach $|\omega_e| = \omega_{e,max}$ that gives an i_s vector that lies over the d-axis, which generates no torque. In this case, all the current of the machine is used to reduce the magnetic flux instead of generating torque. The machine can no longer accelerate and stays at $\omega_{e,max}$, where it can be calculated as

$$I_{ch} = \frac{v_{s,max}}{\omega_{e,max} L_d} + i_{s,max} \tag{2.36}$$

Resulting in

$$\omega_{e,max} = \frac{v_{s,max}}{L_d \left(I_{ch} - i_{s,max}\right)} \tag{2.37}$$

The VLC for $\omega_{e,max}$ can be seen in Figure 2.18, along with a VLC for a speed higher than it.

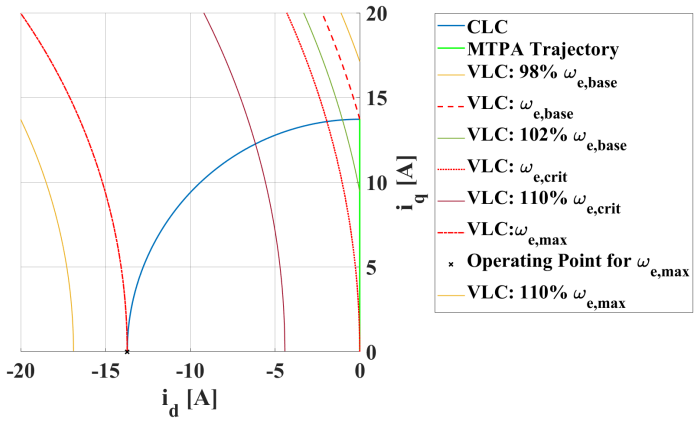

Figure 2.18: Case 1 Maximum Speed

Therefore, it can be defined the fourth – and last – trajectory of operation, denoted as Trajectory 4.

$$\text{Case 1}\\ \text{Trajectory 4}\\ \text{VCLMT}\begin{cases} |\omega_e| > \omega_{e,crit} \\ i_{s,lowlim} \leq |i_{s,ref}| \leq i_{s,max} \\ i_{d,ref} = -\dfrac{i_{s,ref}^2}{2I_{ch}} + \dfrac{v_{s,max}^2}{2\lambda_{pm} L_d \omega_e^2} - \dfrac{I_{ch}}{2} \\ i_{q,ref} = \text{sgn}(i_{s,ref})\sqrt{i_{s,ref}^2 - i_{d,ref}^2} \end{cases} \tag{2.38}$$

For speeds between the critical and the maximum, the current trajectory goes from $i_{s,lowlim}$ to $i_{s,max}$, following only the VLC for that speed. Reference currents below $i_{s,lowlim}$ will not be able to be located at the VLC, therefore would violate the voltage constraint. It is also noticed that for any speed above the maximum speed, the VLC will lie completely out of the CLC, as seen in Figure 2.18, thus a voltage and current limited operation is simply not possible.

Case 1 is also referred as "finite speed SPMSM". Keeping in mind that the closer to $\omega_{e,max}$ the machine is, less torque it will have. At $|\omega_e| = \omega_{e,max}$, the only operating point possible is $(-i_{s,max}, 0)$, which yields no torque. For a frictionless case, the machine will be able to reach $\omega_{e,max}$, however will have no torque to accelerate further. As seen in Figure 1.5, the load torque increases with higher speed, and (1.48) shows that the acceleration is zero if $T_m = T_{load}$. Therefore the machine will reach a steady state speed $|\omega_{e,ss}| < \omega_{e,max}$ and cannot accelerate further. If the machine has no mechanical system attached to its shaft and it has a very small friction coefficient, $|\omega_{e,ss}| \approx \omega_{e,max}$. Only for a frictionless ideal case $|\omega_{e,ss}| = \omega_{e,max}$.

Having i_{dq} from the algorithm, by manipulating (1.39)–(1.43), considering steady state and having in mind that the resistive voltage drop was already considered to calculate $v_{s,max}$, one can write

$$i_s = \sqrt{i_d^2 + i_q^2} \tag{2.39}$$

$$v_d = -\omega_e L_q i_q \tag{2.40}$$

$$v_q = \omega_e (L_d i_d + \lambda_{pm}) \tag{2.41}$$

$$v_s = \sqrt{v_d^2 + v_q^2} \tag{2.42}$$

By using (2.39)–(2.42) together with (1.46)–(1.47), it is created a MATLAB script to verify the algorithm. It calculates the voltages, currents, torque and power for each speed for a certain current reference. It can be seen in Appendix A. For maximum torque desired, the currents and voltages are seen in Figures 2.19a and 2.19b, respectively.

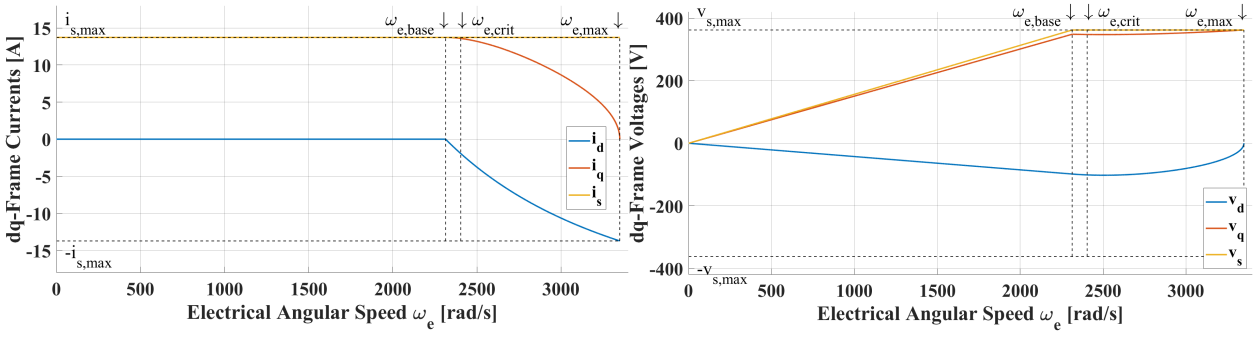

(a) Currents (b) Voltages

Figure 2.19: Case 1 dq-Frame Currents and Voltages for Maximum Torque

For the case in which $i_{s,ref} = i_{s,max}$, the machine operates in Trajectory 1 up to $\omega_{e,base}$, then enters in Trajectory 3, since for any $\omega_{e,base} \leq \omega_e \leq \omega_{e,base}$ the reference current $i_{s,ref} = i_{s,max}$ is higher than the cutoff current $i_{s,cut}$. The machine operates in Trajectory 4 for $\omega_e > \omega_{e,crit}$, until it reaches its maximum speed. It is noticeable in Figure 2.19a that there is no d-axis current up to the base speed, in which field weakening is necessary. After that, the stator voltage is kept constant for the whole range of $\omega_e > \omega_{e,base}$. The resulting torque and power are seen in Figures 2.20a and 2.20b, respectively.

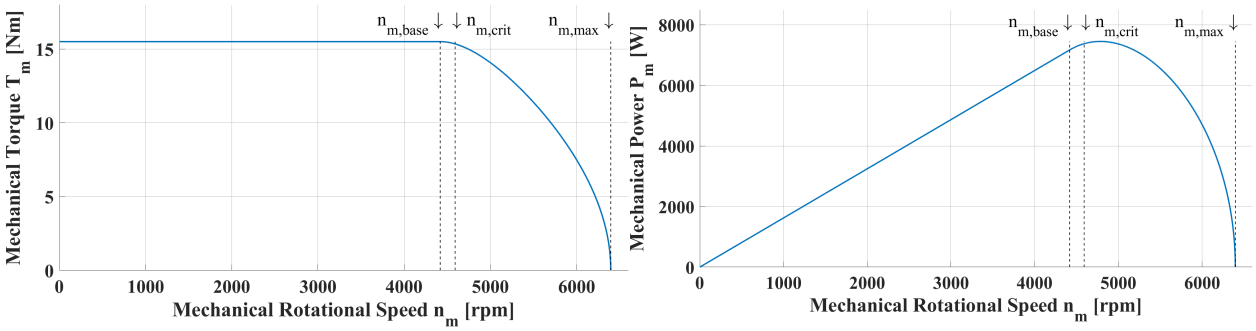

(a) Torque (b) Power

Figure 2.20: Case 1 Torque and Power for Maximum Torque

As expected, the machine torque is constant up to $\omega_e = \omega_{e,base}$, and falls after said speed.

For a zero torque reference, the currents and voltages are seen in Figures 2.21a and 2.21b, respectively.

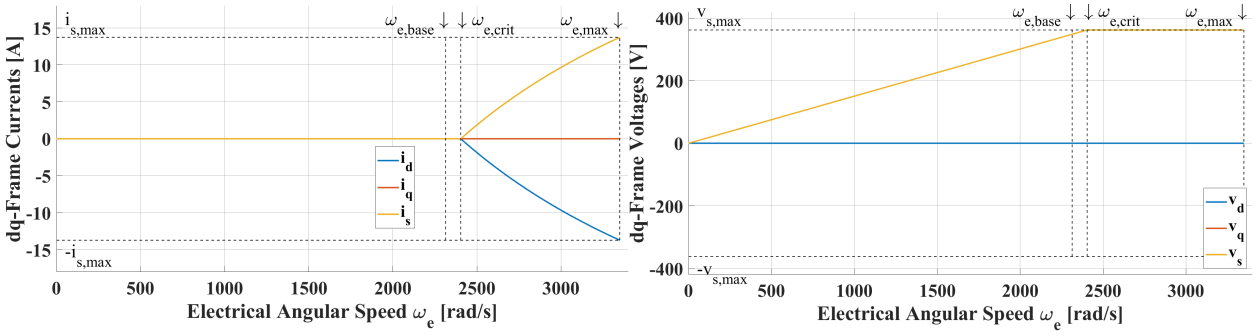

(a) Currents

(b) Voltages

Figure 2.21: Case 1 dq-Frame Currents and Voltages for Zero Torque

It is possible to notice in Figure 2.21b that the stator voltage stays within its limit up to $\omega_e = \omega_{e,crit}$, as opposed to the maximum torque case, seen in Figure 2.19b, where $v_s = v_{s,max}$ for $\omega_e = \omega_{e,base}$. Therefore, the algorithm proposed does not create a negative value for the reference d-axis current up to the critical speed, proving that the zero current vector satisfies the voltage constraint up to the critical speed. Due to the fact that $i_q = 0$ for all speeds, the machine's torque – and, consequently, its power – are constant at zero. It is also noticeable that $i_s = i_{s,max}$ for $\omega_e = \omega_{e,max}$, due to the sole contribution of the negative d-axis current, meaning that the current constraint should be violated for $\omega_e > \omega_{e,max}$ to keep $v_s = v_{s,max}$.

2.3.2 Case 2: SPMSM with $I_{ch} < i_{s,max}$

For illustration purposes, it will be defined a numerical example for a machine fitted in Case 2. It is based on a multi-MW wind turbine, and its parameters can be seen in Table 2.3.

SPMSM Case 2	
R_s	$821\mu\Omega$
L_d	$1.573mH$
L_q	$1.573mH$
λ_{pm}	$4.971Wb$
p_p	26
V_{DC}	$1.2kV$
$i_{s,max}$	$4kA$

Table 2.3: Parameters for Case 2

Similarly to Case 1, for Case 2 it is possible to plot its MTPA trajectory, current limiting circle (CLC) and voltage-limiting circle (VLC) for the base and critical speeds, based in (2.24), (2.31) and (2.25), and it is seen in Figure 2.22.

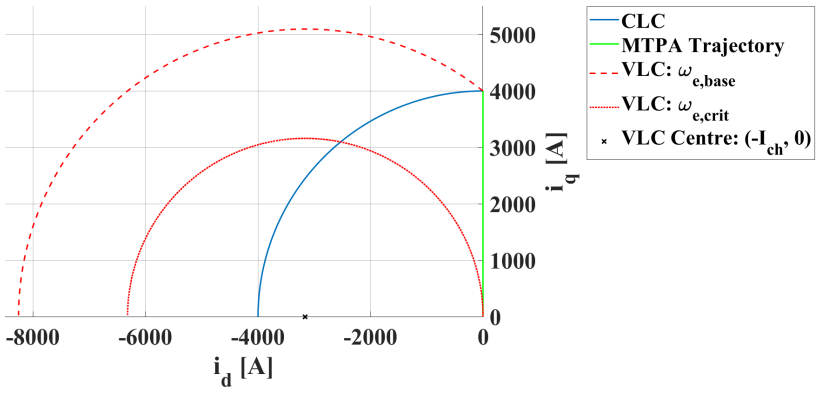

Figure 2.22: Case 2 MTPA, CLC and VLCs

For Case 2, the concepts of base speed and critical speed are the same from Case 1. The trajectory for $|\omega_e| \leq \omega_{e,base}$ is along the MTPA line, for $\omega_{e,base} \leq |\omega_e| \leq \omega_{e,crit}$ is along the MTPA line up to the cutoff current, and then along the VLC, and for $\omega_{e,crit}$ it is only over the VLC, as already discussed for Case 1.

One can notice that for an increasing machine speed, the VLC will shrink, however it will always have a portion of its circumference inside the CLC, therefore the maximum speed cannot be defined. For $|\omega_e| = \infty$, the VLC will shrink into a point – its own center, $(-I_{ch}, 0)$ – that will become the only operating point possible for said speed: and only at said speed the machine will lose all its torque.

It is plotted in Figure 2.23 the VLC for a speed of 322.19% of $\omega_{e,crit}$ (the reason for this peculiar value will be discussed later) and along with it two torque lines, for torques T_{e1} and T_{e2}, where $T_{e1} > T_{e2}$, that cross said VLC – thus being achievable at that speed.

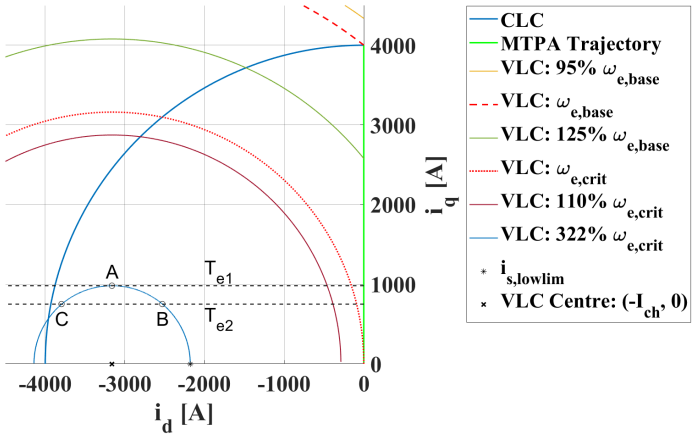

Figure 2.23: Case 2 MTPA, CLC and VLCs

For Case 1, the current trajectory would start from $i_{s,lowlim}$ and follow the VLC up to $i_{s,max}$: for a higher current, a higher torque would be produced. However, for Case 2, this is not true for a certain speed range. In Figure 2.23, it is possible to observe that by starting the current trajectory in $i_{s,lowlim}$ and following the VLC, the peak torque occurs at Point A, but said point is not located at $i_s = i_{s,max}$, thus, after Point A, a higher current will imply in a lower torque. Points B and C are located in the same VLC, thus will need the same stator voltage $v_s = v_{s,max}$ for the same speed $|\omega_e| = 3.2219\omega_{e,crit}$ and are located in the same torque line, thus will produce the same torque $T_e = T_{e2}$, however the stator current for Point C is higher than the current for Point B. For every operating point located between $i_{s,lowlim}$ and Point A there is an equivalent point located between Point A and $i_{s,max}$ that will have the same voltage, speed and torque, but with higher current. Therefore, it is defined the *upper limit current*, $i_{s,upplim}$, as the stator current that produces the maximum torque, as shown by Point A in Figure 2.23. A torque plot for the VLC from Figure 2.23 can be seen in Figure 2.24.

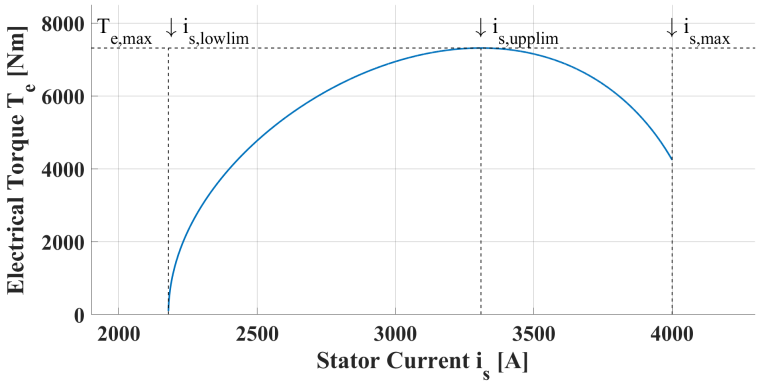

Figure 2.24: Case 2 Torque and Definition of $i_{s,upplim}$

The upper limit current $i_{s,upplim}$ will be located along the maximum torque per Volt (MTPV) trajectory, a trajectory that starts at the centre of the VLCs, located at $(-I_{ch}, 0)$. Similarly to the MTPA for operation below the base speed, it is perpendicular to the torque lines, and due to the fact that said lines are completely horizontal, the MTPV trajectory is a vertical line located at the centre of the VLCs, and can be seen in Figure 2.25.

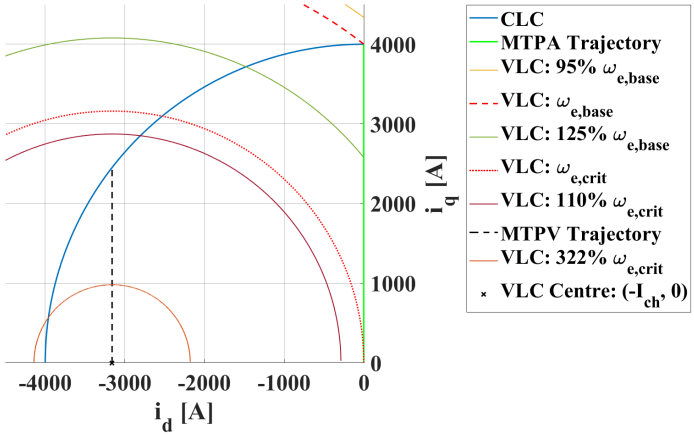

Figure 2.25: Case 2 VLMT Trajectory

The upper limit current $i_{s,upplim}$ can be calculated as the point in which the VLC intercepts the MTPV line. In this case, its d-axis value will be $-I_{ch}$, and its q-axis value will be the vertical radius of the VLC, or $v_{s,max}/\omega_e L_d$. Therefore,

$$i_{s,upplim} = \sqrt{I_{ch}^2 + \left(\frac{v_{s,max}}{\omega_e L_d}\right)^2} \tag{2.43}$$

However, not all VLCs are limited by the MTPV line. The lowest speed in which this occurs is the VLC that intercepts the point where the MTPV and the CLC intercept each other. This speed will be defined as *demagnetizing speed*, and denoted as $\omega_{e,demag}$, due to the fact that the d-axis component for $i_{s,upplim}$ will be equal to $-I_{ch}$ for any speed $|\omega_e| \geq \omega_{e,demag}$, thus demagnetizing the permanent magnets completely. At $|\omega_e| = \omega_{e,demag}$ for $i_{s,ref} = i_{s,max}$, from (2.38),

$$\begin{cases} i_{d,ref} = -I_{ch} \\ i_{q,ref} = \sqrt{i_{s,max}^2 - I_{ch}^2} \end{cases} \tag{2.44}$$

From (2.44) into (2.23),

$$\omega_{e,demag} = \frac{v_{s,max}}{L_q \sqrt{i_{s,max}^2 - I_{ch}^2}} \tag{2.45}$$

The upper limit current $i_{s,upplim}$ can be seen as a function of ω_e in Figure 2.26. For $|\omega_e| = \omega_{e,demag}$, $i_{s,upplim} = i_{s,max}$, denoting that said speed dictates the transition towards a MTPV operation. Even though getting smaller for an increasing speed, the minimum value for said current is $i_{s,upplim} = I_{ch}$ for $|\omega_e| = \infty$, where the machine loses its torque.

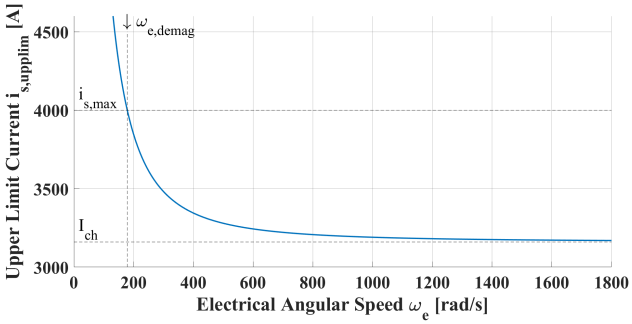

Figure 2.26: Case 2 Upper Limit Current

The VLC for $\omega_{e,demag}$ can be plotted, and seen in Figure 2.27. It is pointed out that the VLC being studied so far, previously denoted as 322.19% of $\omega_{e,crit}$ is actually 250% of $\omega_{e,demag}$, and it was plotted with the intention of showing a VLC for a speed above $\omega_{e,demag}$.

It is also shown a VLC which lies completely inside of the CLC, 500% of $\omega_{e,demag}$: for this speed, operation with $i_{s,ref} = i_{s,max}$ is not only disadvantageous, but will violate the voltage constraint, since no point that belongs to its VLC is lying at the CLC.

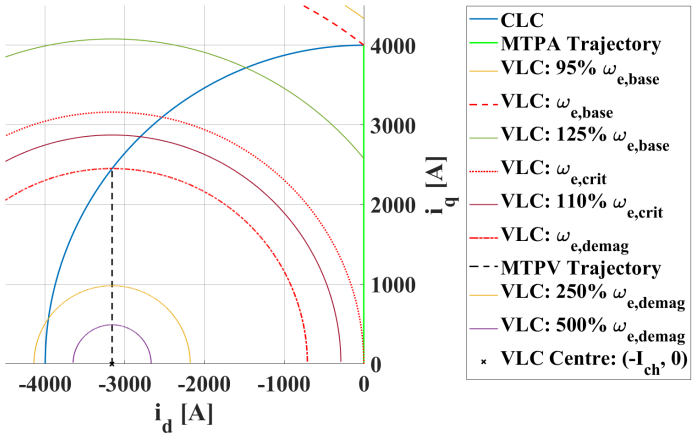

Figure 2.27: Case 2 Demagnetizing Speed

Therefore, for a speed $|\omega_e| \geq \omega_{e,demag}$, the current trajectory starts from $i_{s,lowlim}$ and follows the VLC up to $i_{s,upplim}$, defining the MTPV trajectory of operation for Case 2,

$$\text{Case 2 MTPV} \begin{cases} |\omega_e| \geq \omega_{e,demag} \\ i_{s,lowlim} \leq |i_{s,ref}| \leq i_{s,upplim} \\ i_{d,ref} = -\dfrac{i_{s,ref}^2}{2I_{ch}} + \dfrac{v_{s,max}^2}{2\lambda_{pm} L_d \omega_e^2} - \dfrac{I_{ch}}{2} \\ i_{q,ref} = \text{sgn}(i_{s,ref}) \sqrt{i_{s,ref}^2 - i_{d,ref}^2} \end{cases} \tag{2.46}$$

It is possible to visualize all the current trajectories for the speeds shown in Figure 2.27 in Figure 2.28.

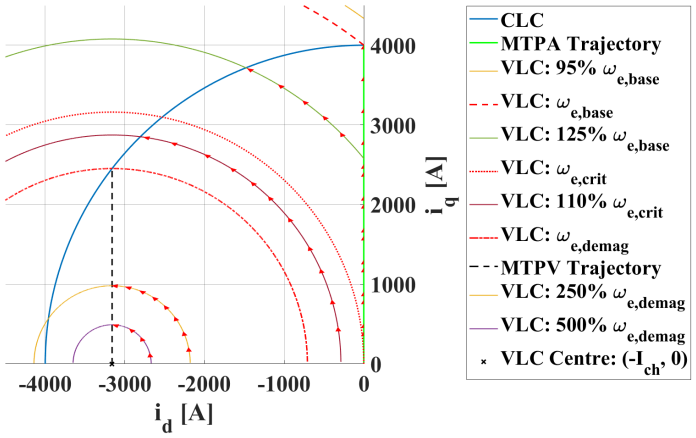

Figure 2.28: Case 2 Current Trajectories

For Case 1, the finite speed SPMSM, it is possible to conclude that $\omega_{e,base} < \omega_{e,crit} < \omega_{e,max}$. For Case 2, the theoretically infinite speed SPMSM, it can be concluded that $\omega_{e,base} < \omega_{e,crit}$ and $\omega_{e,base} < \omega_{e,demag}$, however no relation can be established between $\omega_{e,crit}$ and $\omega_{e,demag}$ – one can be higher, lower or even equal than the other. So far, the case studied was for a machine in which $\omega_{e,crit} < \omega_{e,demag}$, however in order to create an algorithm that can serve to any machine fitted in Case 2, the scenario of a machine in which $\omega_{e,crit} > \omega_{e,demag}$ must be studied. By changing the maximum current $i_{s,max}$ from the SPMSM Example 2 from $4kA$ to $5kA$ – or simply submitting the machine to a 25% overcurrent operation – the machine now has $\omega_{e,crit} > \omega_{e,demag}$, as can be seen in Figure 2.29.

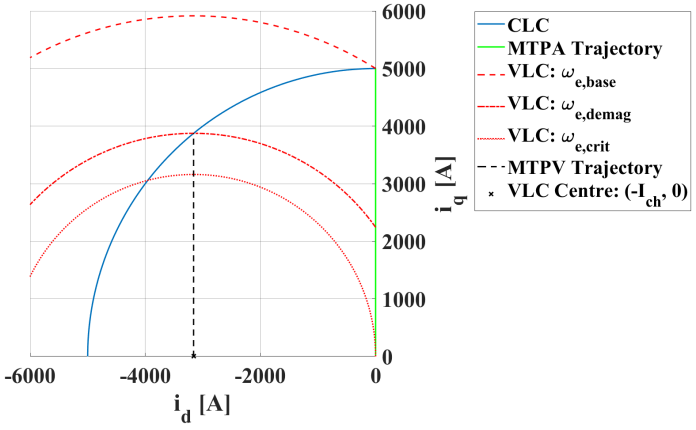

Figure 2.29: Modified Case 2

It is then possible to have a speed $\omega_{e,demag} < |\omega_e| < \omega_{e,crit}$, and it is visualized in Figure 2.30.

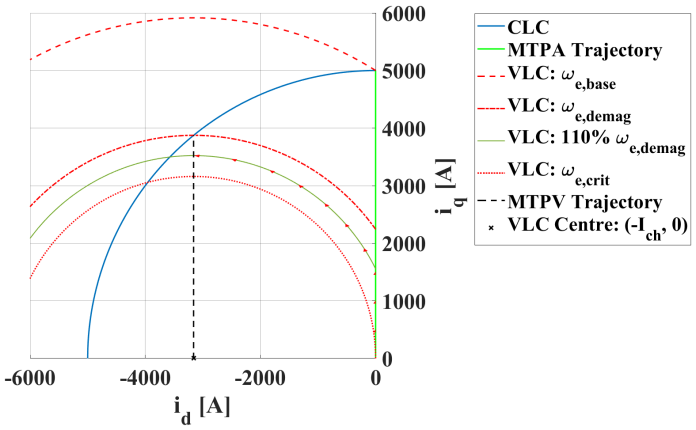

Figure 2.30: Modified Case 2 Trajectory

The fact that $\omega_{e,crit}$ can be higher, equal to or lower than $\omega_{e,demag}$ implies that a certain speed can have an $i_{s,upplim} < i_{s,max}$ and $i_{s,lowlim} > 0$ independently from each other. Therefore, $i_{s,upplim} < i_{s,max}$ must be calculated for every $|\omega_e| > \omega_{e,demag}$ and, concurrently, $i_{s,lowlim} > 0$ must be calculated for every $|\omega_e| > \omega_{e,crit}$, thus the MTPV region of operation will not be denoted as Region 5, to not suggest the existence of a relationship between $\omega_{e,crit}$ and $\omega_{e,demag}$. Both Regions 3, 4 and the MTPV operation will have their currents limited to $i_{s,lowlim} \leq |i_{s,ref}| \leq i_{s,upplim}$, however it is possible to have $i_{s,lowlim} = 0$ and/or $i_{s,upplim} = i_{s,max}$. If $|\omega_e| > \omega_{e,demag}$ it will be calculated $i_{s,upplim}$, but the equations used to decompose $i_{s,ref}$ into $i_{dq,ref}$ will depend on one of the cases for $|\omega_e| > \omega_{e,base}$. Finally, similarly to Case 1, the regions of operation for Case 2 can be defined as the following:

$$\begin{matrix}\text{Case 2} \\ \text{Trajectory 1} \\ \text{MTPA}\end{matrix}\begin{cases}|\omega_e| \leq \omega_{e,base} \\ 0 \leq |i_{s,ref}| \leq i_{s,max} \\ i_{d,ref} = 0 \\ i_{q,ref} = i_{s,ref}\end{cases} \tag{2.47}$$

$$\begin{matrix}\text{Case 2} \\ \text{MTPV}\end{matrix}\begin{cases}|\omega_e| \geq \omega_{e,demag} \\ i_{s,upplim} = \sqrt{I_{ch}^2 + \left(\dfrac{v_{s,max}}{\omega_e L_d}\right)^2}\end{cases} \tag{2.48}$$

$$\text{Case 2 Trajectory 2 VCLMT} \begin{cases} \omega_{e,base} \leq |\omega|_e \leq \omega_{e,crit} \\ 0 \leq |i_{s,ref}| \leq i_{s,cut} \\ i_{d,ref} = 0 \\ i_{q,ref} = i_{s,ref} \end{cases} \tag{2.49}$$

$$\text{Case 2 Trajectory 3 VCLMT} \begin{cases} \omega_{e,base} \leq |\omega_e| \leq \omega_{e,crit} \\ i_{s,cut} \leq |i_{s,ref}| \leq i_{s,upplim} \leq i_{s,max} \\ i_{d,ref} = -\dfrac{i_{s,ref}^2}{2I_{ch}} + \dfrac{v_{s,max}^2}{2\lambda_{pm} L_d \omega_e^2} - \dfrac{I_{ch}}{2} \\ i_{q,ref} = \text{sgn}(i_{s,ref}) \sqrt{i_{s,ref}^2 - i_{d,ref}^2} \end{cases} \tag{2.50}$$

$$\text{Case 2 Trajectory 4 VCLMT} \begin{cases} |\omega_e| \geq \omega_{e,crit} \\ i_{s,lowlim} \leq |i_{s,ref}| \leq i_{s,upplim} \leq i_{s,max} \\ i_{d,ref} = -\dfrac{i_{s,ref}^2}{2I_{ch}} + \dfrac{v_{s,max}^2}{2\lambda_{pm} L_d \omega_e^2} - \dfrac{I_{ch}}{2} \\ i_{q,ref} = \text{sgn}(i_{s,ref}) \sqrt{i_{s,ref}^2 - i_{d,ref}^2} \end{cases} \tag{2.51}$$

According to the lower limit equation (2.35) and the upper limit current equation (2.43), for $|\omega_e| = \infty$, $i_{s,lowlim} = i_{s,upplim} = I_{ch}$, indicating that the only magnitude for the stator current possible is equal to the characteristic current. By setting $|i_{s,ref}| = I_{ch}$ in (2.51), the algorithm decomposes the reference stator current into $i_{d,ref} = -I_{ch}$ and $i_{q,ref} = 0$, indicating that $(-I_{ch}, 0)$ is the only operating point possible for $|\omega_e| = \infty$, and that for said speed there is no torque produced. For any $|\omega_e| < \infty$, $i_{s,upplim} > I_{ch}$, which allows for a $|i_{q,ref}| > 0$, thus allowing a non-zero torque to be produced at any speed. This validates the "infinite speed" PMSM concept, a machine that has a valid operating point for any rotational speeds. However, in a practical implementation, a PMSM will have a maximum speed dictated by other factors, such as the converter's switching frequency, stress on the machine's bearings,

centrifugal forces on the rotor, and rotational friction.

Similarly to Case 1, the algorithm for Case 2 is implemented in a MATLAB script to evaluate the voltages, currents, torque and power for the machine at different speeds. For maximum torque, the currents and voltages can be seen in Figures 2.31a and 2.31b, respectively.

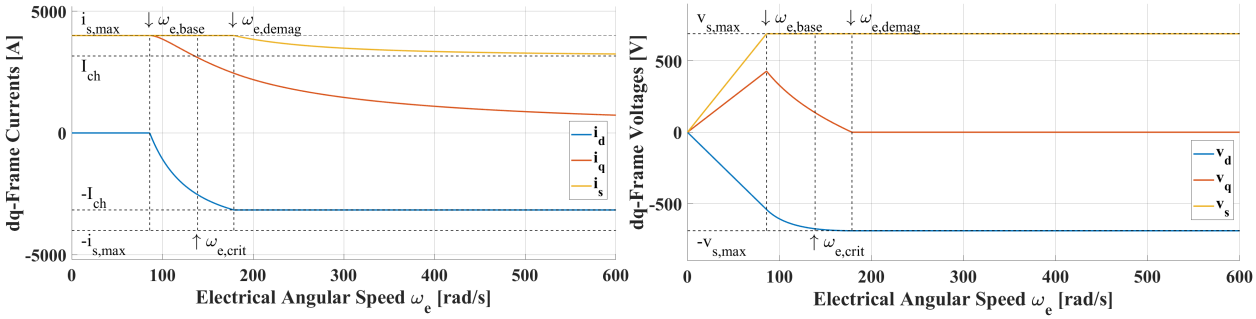

(a) Currents (b) Voltages

Figure 2.31: Case 2 dq-Frame Currents and Voltages for Maximum Torque

Similarly to Case 1, the maximum voltage for the maximum current is achieved at $\omega_e = \omega_{e,base}$. The machine is able to receive $i_s = i_{s,max}$ up to $\omega_e = \omega_{e,demag}$, when the MTPV trajectory needs to be followed and limit the machine's maximum current. $\omega_e = \omega_{e,demag}$ also marks the speed in which the permanent magnets are completely demagnetized, and it can be seen as a zero q-axis voltage. As its speed increases, i_q keeps decreasing towards zero, and i_s towards I_{ch}. The torque and power for this scenario can be seen in Figures 2.32a and 2.32b, respectively.

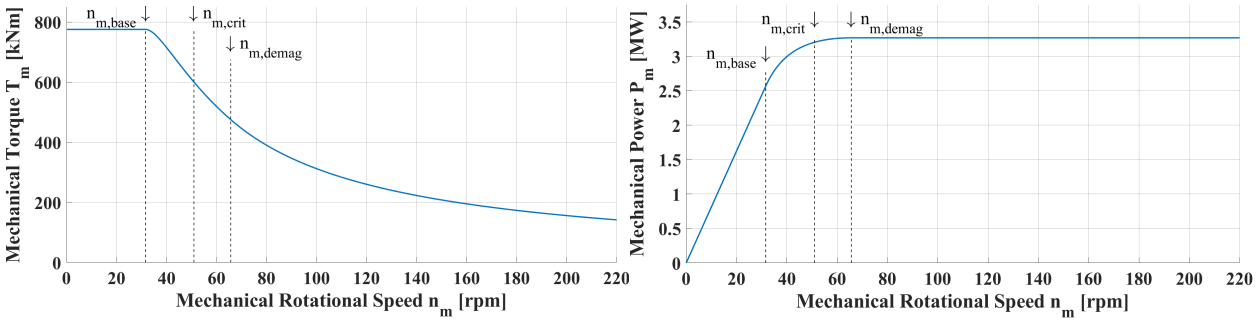

(a) Torque (b) Power

Figure 2.32: Case 2 Torque and Power for Maximum Torque

Case 2 is very distinct with respect to Case 1 for their torque curves. While a finite speed PMSM loses its torque completely at $\omega_e = \omega_{e,max}$, the in theory infinite speed PMSM is able

to maintain a non-zero torque for any speed, even though it decreases as its speed increases. It is also able to maintain a constant maximum power for $\omega_e \geq \omega_{e,demag}$.

For a zero torque reference, the currents and voltages can be seen in Figures 2.33a and 2.33b, respectively.

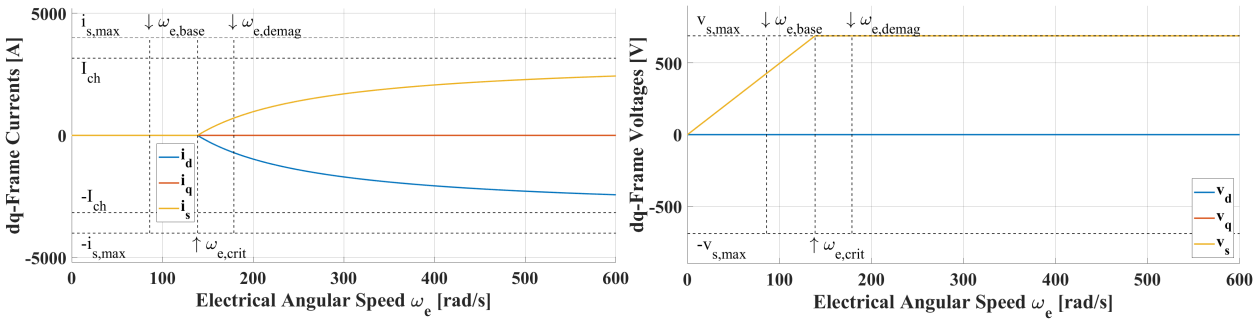

(a) Currents (b) Voltages

Figure 2.33: Case 2 dq-Frame Currents and Voltages for Zero Torque

Similarly to Case 1, the maximum voltage is achieved at $\omega_e = \omega_{e,crit}$ instead of $\omega_e = \omega_{e,base}$. The critical speed also marks the speed in which a negative d-axis current needs to be generated to counter the machine's induced voltage. Said current increases with magnitude with an increasing machine speed, moving towards the characteristic current, therefore $i_{d,ref} = -I_{ch}$ for $\omega_e = \infty$.

The case where $\omega_{e,crit} > \omega_{e,demag}$, the "Modified Case 2" is also studied. For maximum torque, the machine's currents and voltages can be seen in Figures 2.34a and 2.34b, respectively.

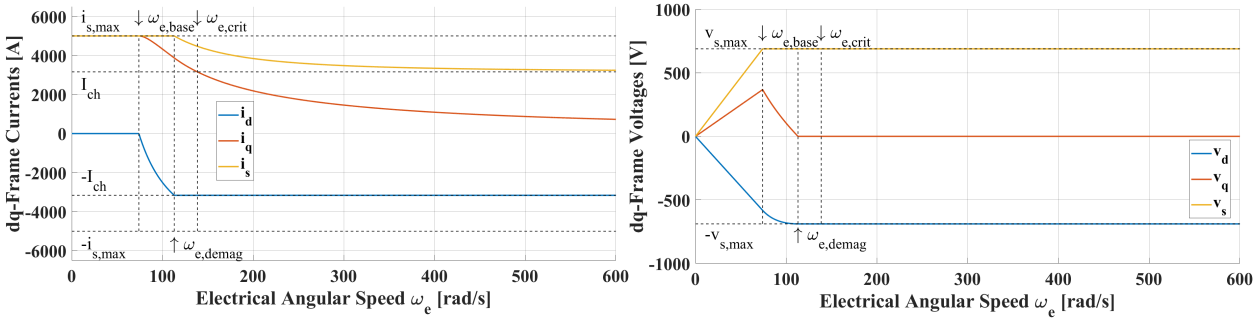

(a) Currents (b) Voltages

Figure 2.34: Modified Case 2 dq-Frame Currents and Voltages for Maximum Torque

Similarly to a machine where $\omega_{e,crit} < \omega_{e,demag}$, a case where $\omega_{e,crit} > \omega_{e,demag}$ also presents

a d-axis current of $-I_{ch}$ at $\omega_{e,crit} = \omega_{e,demag}$. The torque and power curves can be seen in Figures 2.35a and 2.35b, respectively.

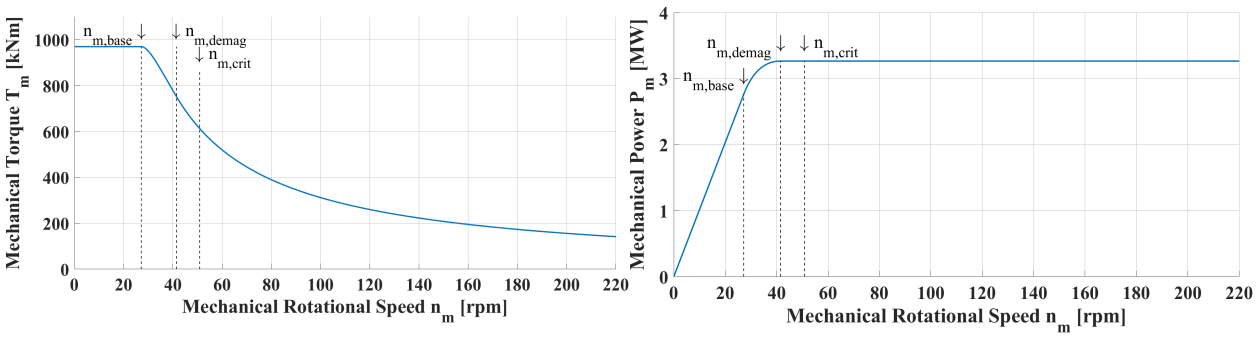

(a) Torque

(b) Power

Figure 2.35: Modified Case 2 Torque and Power for Maximum Torque

Similarly to the unmodified Case 2, the modified Case 2 presents maximum power for $\omega_e \geq \omega_{e,demag}$. For a zero torque reference, the currents and voltages are seen in Figures 2.33a and 2.33b, respectively.

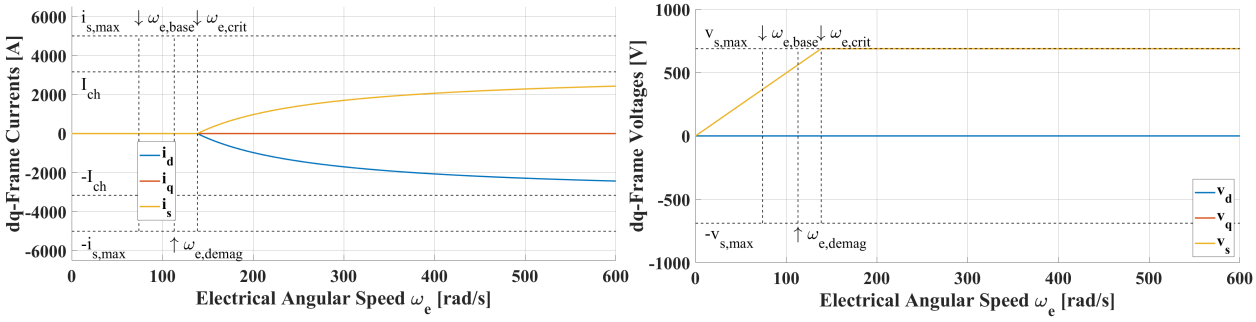

(a) Torque

(b) Power

Figure 2.36: Modified Case 2 Torque and Power for Zero Torque

The case where $\omega_{e,crit} > \omega_{e,demag}$ behaves similarly to the case where $\omega_{e,crit} < \omega_{e,demag}$: both present a maximum power at $\omega_{e,crit} = \omega_{e,demag}$, which remains constant for any speed over the demagnetizing one, and both cases also display $i_{d,ref} = -I_{ch}$ for $\omega_{e,crit} \geq \omega_{e,demag}$ at maximum torque and $i_{d,ref} < 0$ for $\omega_{e,crit} \geq \omega_{e,crit}$ for zero torque. It can be concluded that, as long as both the $|\omega_e| > \omega_{e,crit}$ and $|\omega_e| > \omega_{e,demag}$ operation modes are considered, the relationship between $\omega_{e,crit}$ and $\omega_{e,demag}$ does not impact the machine operation.

2.3.3 Case 3: IPMSM with $I_{ch} > i_{s,max}$

Similarly to Cases 1 and 2, it will be defined a machine to illustrate Case 3, which parameters are seen in Table 2.4. It is the same machine used as an example in subsection 2.2.2.

IPMSM Case 3	
R_s	$4.23m\Omega$
L_d	$171\mu H$
L_q	$391\mu H$
λ_{pm}	$103.9mWb$
p_p	6
V_{DC}	$288V$
$i_{s,max}$	$570A$

Table 2.4: Parameters for Case 3

Case 3 is similar to Case 1 in terms of trajectories and definitions, however some equations change. Similarly to the previous cases, it is possible to draw the CLC, MTPA trajectory and the voltage-limiting Ellipse (VLE) for the base speed, which are seen in Figure 2.37.

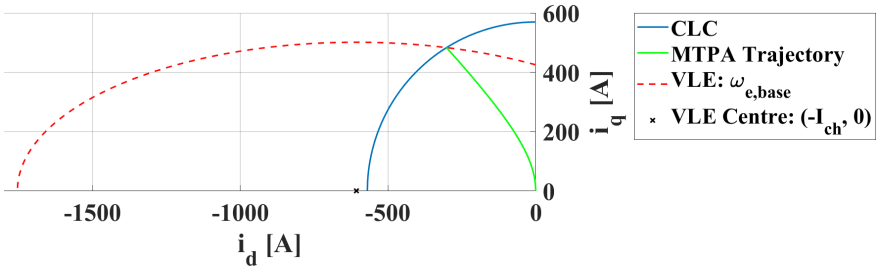

Figure 2.37: Case 3 MTPA, CLC and Base Speed VLE

Below the base speed, the operation is given by

$$\begin{cases} \text{Case 3} \\ \text{Trajectory 1} \\ \text{MTPA} \end{cases} \begin{cases} |\omega_e| \leq \omega_{e,base} \\ 0 \leq |i_{s,ref}| \leq i_{s,max} \\ i_{d,ref} = \dfrac{\lambda_{pm} - \sqrt{\lambda_{pm}^2 + 8(L_q - L_d)^2 i_{s,ref}^2}}{4(L_q - L_d)} \\ i_{q,ref} = \text{sgn}(i_{s,ref}) \sqrt{i_{s,ref}^2 - i_{d,ref}^2} \end{cases} \tag{2.52}$$

The critical speed $\omega_{e,crit}$ was already defined in (2.31) and, since said definition uses the

horizontal radius of the VLE, it remains the same for Case 3. However, the cutoff current $i_{s,cut}$ needs to be recalculated for the IPMSM case, since the MTPA and VLE equations change.

Even though (2.25) is in the implicit form, it is possible to solve for i_q by considering only the positive half of the ellipse, which gives

$$i_{q,VLE} = \frac{v_{s,max}}{\omega_e L_q}\sqrt{1 - \left(\frac{i_{d,VLE} + I_{ch}}{v_{s,max}/\omega_e L_d}\right)^2} \tag{2.53}$$

Similarly, i_q is obtained from the MTPA algorithm (2.14) as

$$i_{q,MTPA} = \sqrt{i_{d,MTPA}^2 - \frac{\lambda_{pm}}{L_q - L_d} i_{d,MTPA}} \tag{2.54}$$

Since the cutoff point satisfies both the MTPA and the voltage-limiting ellipse equations, $i_{q,VLE} = i_{q,MTPA}$. Therefore, equation (2.54) with (2.53) results in

$$\sqrt{i_{d,cut}^2 - \frac{\lambda_{pm}}{L_q - L_d} i_{d,cut}} = \frac{v_{s,max}}{\omega_e L_q}\sqrt{1 - \left(\frac{i_{d,cut} + I_{ch}}{v_{s,max}/\omega_e L_d}\right)^2} \tag{2.55}$$

While solving (2.55) for $i_{d,cut}$, one notices that it results in a quadratic equation in the form

$$k_1 i_{d,cut}^2 + k_2 i_{d,cut} + k_3 = 0 \tag{2.56}$$

with coefficients

$$\begin{cases} k_1 = 1 + \dfrac{L_d^2}{L_q^2} \\ k_2 = \dfrac{2L_d\lambda_{pm}}{L_q^2} - \dfrac{\lambda_{pm}}{L_q - L_d} \\ k_3 = \dfrac{\lambda_{pm}^2}{L_q^2} - \left(\dfrac{v_{s,max}}{\omega_e L_q}\right)^2 \end{cases} \tag{2.57}$$

Therefore, two solutions exist:

$$\begin{cases} i_{d,cut,1} = \dfrac{-k_2 + \sqrt{k_2^2 - 4k_1k_3}}{2k_1} > 0 \\ i_{d,cut,2} = \dfrac{-k_2 - \sqrt{k_2^2 - 4k_1k_3}}{2k_1} < 0 \end{cases} \tag{2.58}$$

Since the machine will operate either in the second or third quadrant of the d-q plane (for forward and backward torque operations, respectively), all d-axis currents must be negative. Therefore, the negative solution for (2.58) is chosen, thus

$$i_{d,cut} = \frac{-k_2 - \sqrt{k_2^2 - 4k_1k_3}}{2k_1} \tag{2.59}$$

To obtain $i_{q,cut}$, the solution from (2.58) is used in either (2.53) or (2.54): they will produce the same result, since the point is common to both curves, thus satisfies both equations. Due to its simplicity, (2.54) is chosen. Therefore,

$$i_{q,cut} = \sqrt{i_{d,cut}^2 - \frac{\lambda_{pm}}{L_q - L_d} i_{d,cut}} \tag{2.60}$$

Finally,

$$i_{s,cut} = \sqrt{i_{d,cut}^2 + i_{q,cut}^2} \tag{2.61}$$

Within the range $\omega_{e,base} \leq |\omega_e| \leq \omega_{e,crit}$, for a stator current $i_{s,ref} \leq i_{s,cut}$, the current trajectory can still follow the MTPA trajectory. For $i_{s,ref} \geq i_{s,cut}$, it must follow the VLE. To obtain the equations for the VLE, it is substituted $i_{q,ref} = \sqrt{i_{s,ref}^2 - i_{d,ref}^2}$ into (2.25), and obtained

$$\left(\frac{i_{d,ref} + I_{ch}}{v_{s,max}/\omega_e L_d}\right)^2 + \left(\frac{\sqrt{i_{s,ref}^2 - i_{d,ref}^2}}{v_{s,max}/\omega_e L_q}\right)^2 = 1 \tag{2.62}$$

and, once more, by solving (2.62) for $i_{d,ref}$, it yields a quadratic function in the form

$$k_4 i_{d,ref}^2 + k_5 i_{d,ref} + k_6 = 0 \tag{2.63}$$

with coefficients

$$\begin{cases} k_4 = \left(\dfrac{\omega_e L_d}{v_{s,max}}\right)^2 - \left(\dfrac{\omega_e L_q}{v_{s,max}}\right)^2 \\ k_5 = 2 I_{ch} \left(\dfrac{\omega_e L_d}{v_{s,max}}\right)^2 \\ k_6 = I_{ch}^2 \left(\dfrac{\omega_e L_d}{v_{s,max}}\right)^2 + i_{s,ref}^2 \left(\dfrac{\omega_e L_q}{v_{s,max}}\right)^2 - 1 \end{cases} \tag{2.64}$$

Therefore, two solutions exist:

$$\begin{cases} i_{d,ref,1} = \dfrac{-k_5 + \sqrt{k_5^2 - 4k_4k_6}}{2k_4} < 0 \\ i_{d,ref,2} = \dfrac{-k_5 - \sqrt{k_5^2 - 4k_4k_6}}{2k_4} > 0 \end{cases} \tag{2.65}$$

Since the first solution of (2.65) is the negative one,

$$i_{d,ref} = \frac{-k_5 + \sqrt{k_5^2 - 4k_4k_6}}{2k_4} \tag{2.66}$$

and, for $i_{q,ref}$, it is simply the remaining part of the current vector, multiplied my the sign of $i_{s,ref}$ to allow regenerative braking. Therefore, similarly to Case 1, trajectories of operation 2 and 3 can be defined as

$$\text{Case 3 Trajectory 2 VCLTM} \begin{cases} \omega_{e,base} \leq |\omega_e| \leq \omega_{e,crit} \\ 0 \leq |i_{s,ref}| \leq i_{s,cut} \\ i_{d,ref} = \dfrac{\lambda_{pm} - \sqrt{\lambda_{pm}^2 + 8(L_q - L_d)^2 i_{s,ref}^2}}{4(L_q - L_d)} \\ i_{q,ref} = \text{sgn}(i_{s,ref})\sqrt{i_{s,ref}^2 - i_{d,ref}^2} \end{cases} \tag{2.67}$$

$$\text{Case 3 Trajectory 3 VCLTM} \begin{cases} \omega_{e,base} \leq |\omega_e| \leq \omega_{e,crit} \\ i_{s,cut} \leq |i_{s,ref}| \leq i_{s,max} \\ i_{d,ref} = \dfrac{-k_5 + \sqrt{k_5^2 - 4k_4k_6}}{2k_4} \\ i_{q,ref} = \text{sgn}(i_{s,ref})\sqrt{i_{s,ref}^2 - i_{d,ref}^2} \end{cases} \tag{2.68}$$

For an operation above the critical speed, the current trajectory is limited only to the VLE, and the lower limit of the stator current $i_{s,lowlim}$ is the same from the SPMSM case as seen in Equation (2.35). Thus, it is possible to define the fourth region of operation as

$$\text{Case 3 Trajectory 4 VCLTM} \begin{cases} |\omega_e| \geq \omega_{e,crit} \\ i_{s,lowlim} \leq |i_{s,ref}| \leq i_{s,max} \\ i_{d,ref} = \dfrac{-k_5 + \sqrt{k_5^2 - 4k_4k_6}}{2k_4} \\ i_{q,ref} = \text{sgn}(i_{s,ref})\sqrt{i_{s,ref}^2 - i_{d,ref}^2} \end{cases} \tag{2.69}$$

Similarly to Case 1, the trajectories for different speeds for Case 3 can be seen in Figure 2.38.

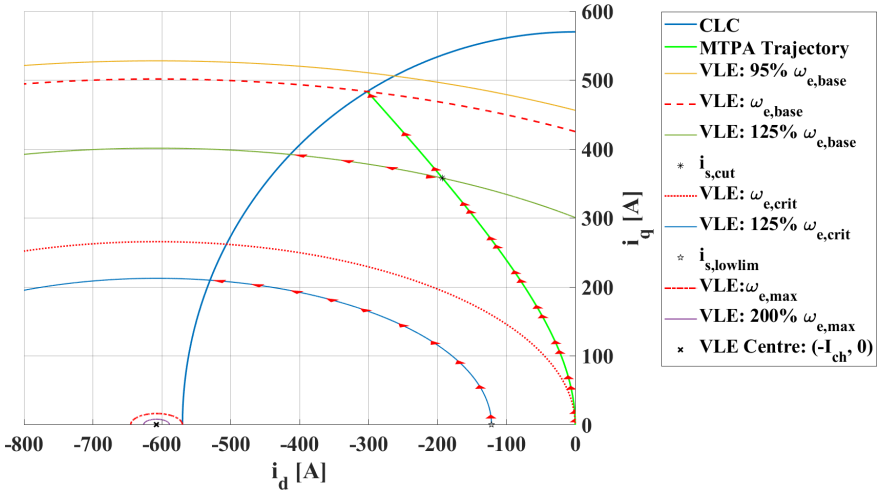

Figure 2.38: Case 3 Current Trajectories

Also similarly to the previous cases, the machine currents and voltages are calculated for the maximum torque case, and seen in Figures 2.39a and 2.39b, respectively.

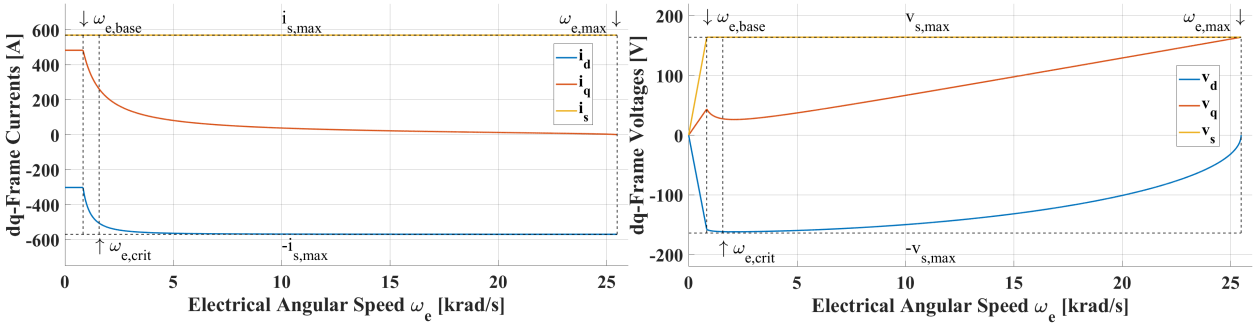

(a) Currents (b) Voltages

Figure 2.39: Case 3 dq-Frame Currents and Voltages for Maximum Torque

For the maximum torque scenario, the mechanical torque and power are seen in Figures 2.40a and 2.40b, respectively.

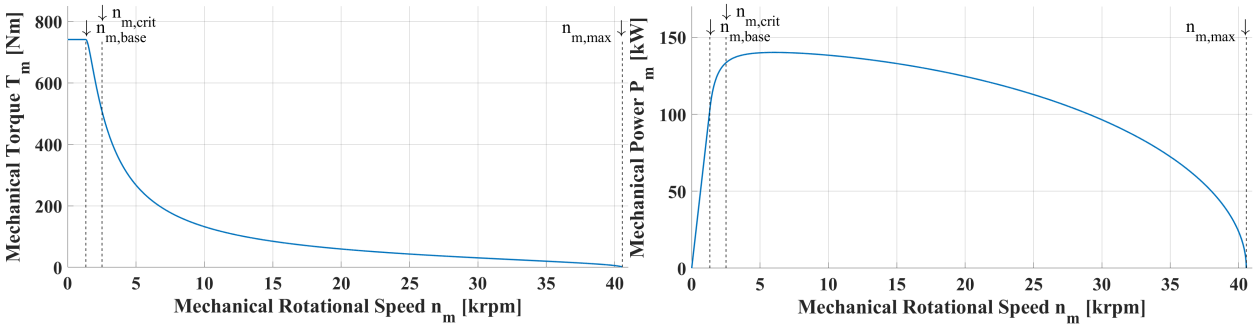

(a) Torque (b) Power

Figure 2.40: Case 3 Torque and Power for Maximum Torque

For a no torque production, the currents and voltages are seen in Figures 2.41a and 2.41b, respectively.

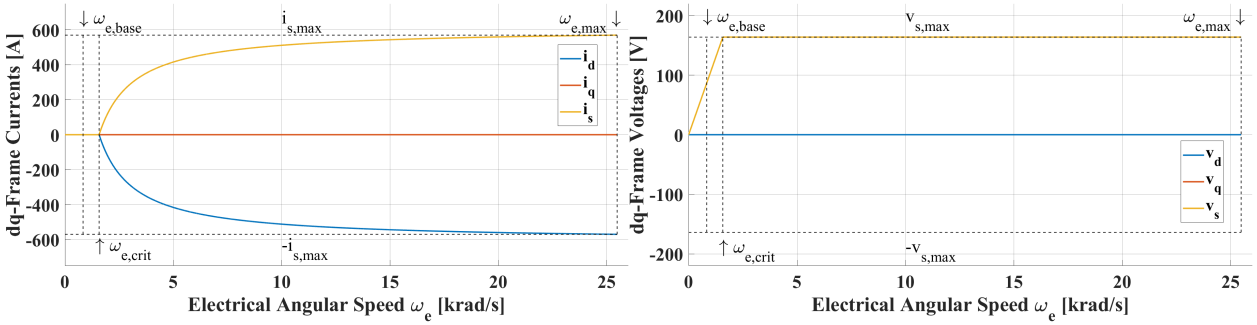

(a) Currents (b) Voltages

Figure 2.41: Case 3 dq-Frame Currents and Voltages for Zero Torque

It is noticeable that the machine for Case 3 has a much higher ratio between its maximum and base speed than the machine Case 1. This is due to the fact that the ratio $I_{ch}/i_{s,max} \approx 1.06$ for Case 3 is much lower than for Case 1. A $I_{ch}/i_{s,max} \approx 1.06$ for the machine studied in Case 3 is much closer to 1 then the ratio $I_{ch}/i_{s,max} \approx 3.54$ for the machine studied in Case 1, thus justifying the high $\omega_{e,max}$ for the machine in Case 3.

2.3.4 Case 4: IPMSM with $I_{ch} < i_{s,max}$

The machine used as an example for Case 4 is the same from Case 3, operating in an overcurrent mode. Thus, $i_{s,max}$ will be increased by 50%, and its parameters are seen in

Table 2.5. Even though the present research focuses on PMSMs, a permanent magnet assisted synchronous reluctance machine (PMASRM) is likely to be fitted in Case 4, and the algorithm that will be developed is also valid for it [29].

IPMSM Case 4	
R_s	$4.23m\Omega$
L_d	$171\mu H$
L_q	$391\mu H$
λ_{pm}	$103.9mWb$
p_p	6
V_{DC}	$288V$
$i_{s,max}$	$855A$

Table 2.5: Parameters for Case 4

In the same way that Case 2 has the same set of equations from Case 1, but defining the demagnetizing speed instead of the maximum speed, Case 4 is related to Case 3 in the same way, however the calculations are not trivial as they were in Case 2. The torque lines for an IPMSM have a hyperbolic shape rather than being horizontal straight lines, thus the MTPV curve will not be a vertical straight line. To illustrate this scenario, the VLE for $\omega_e = 6\omega_{e,base}$ is show in Figure 2.42 with two torque lines: one for the maximum torque achievable for that speed (denoted as T_{e1}) and a lower one, (denoted as T_{e2}). The maximum torque achievable is tangent to the VLE (Point A), in the same way as Case 2, and any torque lower than that will intercept the VLE twice (Points B and C). It is worth noticing that, since the maximum torque point with respect to the VLE lies inside of the CLC, it is safe to assume that $6\omega_{e,base} > \omega_{e,demag}$, even though the demagnetizing speed was not yet discussed for Case 4.

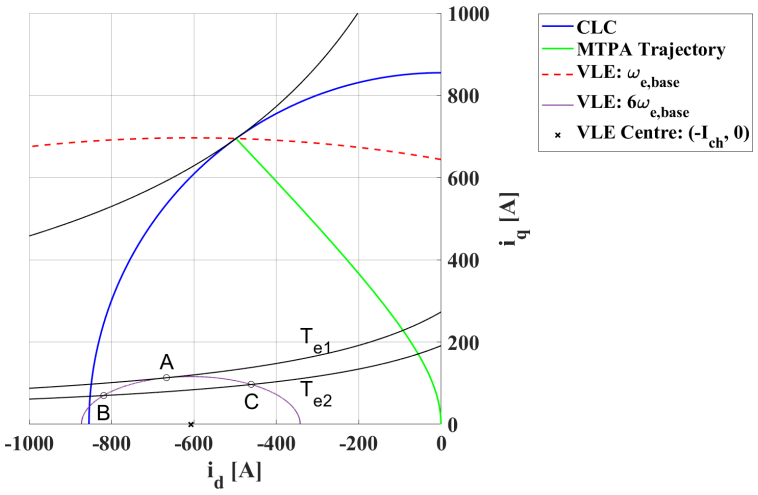

Figure 2.42: Case 4 MTPA, CLC, VLEs and Torque Lines

To obtain the point in which the torque curve is tangential to the VLE, the problem can be summarized as

$$\begin{cases} \text{maximize } T_e = \dfrac{3}{2}(L_d - L_q) i_d i_q + \dfrac{3}{2}\lambda_{pm} i_q \\ \text{with respect to } \left(\dfrac{i_d + I_{ch}}{v_{s,max}/\omega_e L_d} \right)^2 + \left(\dfrac{i_q}{v_{s,max}/\omega_e L_q} \right)^2 = 1 \end{cases} \tag{2.70}$$

Therefore, it is used the method of Lagrange Multipliers, where it states that the gradient of the torque curve is proportional to the gradient of the VLE at the tangential point by a factor of λ_{LM}, the Lagrange multiplier. The subscript "LM" was used to help distinguish the Lagrange multiplier from the magnetic flux linkages, which also use the lambda notation. Thus

$$\nabla T_e = \lambda_{LM} \nabla v_s \tag{2.71}$$

can be expressed as

$$\begin{bmatrix} \dfrac{\partial T_e}{\partial i_{d,MTPV}} \\ \dfrac{\partial T_e}{\partial i_{q,MTPV}} \end{bmatrix} = \lambda_{LM} \begin{bmatrix} \dfrac{\partial v_s}{\partial i_{d,MTPV}} \\ \dfrac{\partial v_s}{\partial i_{q,MTPV}} \end{bmatrix} \tag{2.72}$$

and expanded as

$$\begin{bmatrix} \dfrac{3}{2}(L_d - L_q) i_{q,MTPV} \\ \dfrac{3}{2}(L_d - L_q) i_{d,MTPV} + \dfrac{3}{2}\lambda_{pm} \end{bmatrix} = \lambda_{LM} \begin{bmatrix} \dfrac{2i_{d,MTPV}}{\left(v_{s,max}/\omega_e L_d\right)^2} + \dfrac{2I_{ch}}{\left(v_{s,max}/\omega_e L_d\right)^2} \\ \dfrac{2i_{q,MTPV}}{\left(v_{s,max}/\omega_e L_d\right)^2} \end{bmatrix} \tag{2.73}$$

that can be rewritten as

$$\begin{cases} \dfrac{3}{2}(L_d - L_q) i_{q,MTPV} = \dfrac{2i_{d,MTPV}\lambda_{LM}}{\left(v_{s,max}/\omega_e L_d\right)^2} + \dfrac{2I_{ch}\lambda_{LM}}{\left(v_{s,max}/\omega_e L_d\right)^2} \\ \dfrac{3}{2}(L_d - L_q) i_{d,MTPV} + \dfrac{3}{2}\lambda_{pm} = \dfrac{2i_{q,MTPV}\lambda_{LM}}{\left(v_{s,max}/\omega_e L_d\right)^2} \end{cases} \tag{2.74}$$

or

$$\begin{cases} \dfrac{3}{4}\left(\dfrac{v_{s,max}}{\omega_e L_d}\right)^2 \dfrac{(L_d - L_q) i_{q,MTPV}}{i_{d,MTPV} + I_{ch}} = \lambda_{LM} \\ \dfrac{3}{4i_{q,MTPV}}\left(\dfrac{v_{s,max}}{\omega_e L_q}\right)^2 ((L_d - L_q) i_{d,MTPV} + \lambda_{pm}) = \lambda_{LM} \end{cases} \tag{2.75}$$

Since the right sides of (2.75) are only the Lagrange multiplier, its left sides can be equated to each other. It is then possible to solve the resulting equation for $i_{q,MTPV}$, that becomes only a function of $i_{d,MTPV}$ given by

$$i_{q,MTPV} = \sqrt{\frac{L_d^2 i_{d,MTPV}(i_{d,MTPV} + I_{ch})}{L_q^2} + \frac{L_d \lambda_{pm}(L_d i_{d,MTPV} + \lambda_{pm})}{L_q^2 (L_d - L_q)}} \tag{2.76}$$

By substituting (2.76) into the VLE equation, it is possible to obtain the i_{dq} values as a function of ω_e that compose the MTPV trajectory. To allow a four speed-torque quadrant operation, the absolute value of ω_e is used, thus resulting in

$$\text{MTPV Trajectory} \begin{cases} i_{d,MTPV} = \dfrac{-k_8 - \sqrt{k_8^2 - 4k_7k_9}}{2k_7} \\ i_{q,MTPV} = \dfrac{v_{s,max}}{|\omega_e| L_q} \sqrt{1 - \left(\dfrac{i_{d,MTPV} + I_{ch}}{v_{s,max}/\omega_e L_d} \right)^2} \end{cases} \tag{2.77}$$

with

$$\begin{cases} k_7 = 2L_d^2 \\ k_8 = L_d \lambda_{pm} \left(\dfrac{L_d}{L_d - L_q} + 3 \right) \\ k_9 = \lambda_{pm}^2 \left(\dfrac{L_d}{L_d - L_q} + 1 \right) - \left(\dfrac{v_{s,max}}{\omega_e} \right)^2 \end{cases} \tag{2.78}$$

Therefore, for any $0 \leq |\omega_e| \leq \infty$, the MTPV curve can be plotted, and it is seen in Figure 2.43.

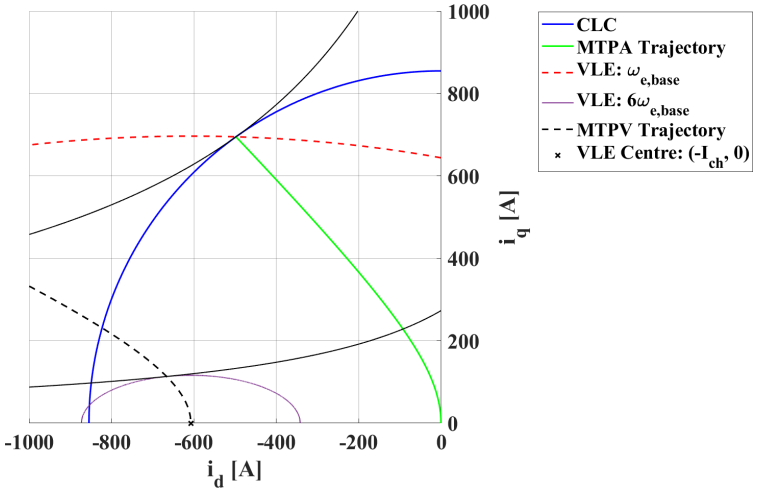

Figure 2.43: Case 4 MTPV Trajectory

It is seen in Figure 2.43 that the MTPV trajectory intercepts the maximum torque point

for the VLE shown, as expected. Similarly to the MTPA trajectory that has its meaning only for $0 \leq i_{s,ref} \leq i_{s,max}$, the MTPV will only be used for $\omega_{e,demag} \leq |\omega_e| \leq \infty$, even though mathematically existing for $|\omega_e| < \omega_{e,demag}$ as well, as shown in Figure 2.43.

The last step is to calculate $\omega_{e,demag}$ for Case 4. This is the speed in which the MTPV trajectory intercepts the CLC, and can be obtained by solving

$$i_{d,MTPV}^2 + i_{q,MTPV}^2 = i_{s,max}^2 \tag{2.79}$$

for ω_e, resulting in $\omega_{e,demag}$. However, when proceeding to solve (2.79), one notices that it yields a quartic equation (*i.e.* a fourth order polynomial equation), which solution is not trivial or a small expression. Proposed methods are shown by [30]–[32], including the use of Ferrari's Method for solving quartic equations, as used by [33], but all of those methods lead to unwieldy expressions that will consume a great amount of computational resources: both memory to store it and time to execute it within a switching cycle.

Instead of solving (2.79) and obtaining an expression for $\omega_{e,demag}$, it is proposed some alternatives. The first is valid only for constant $v_{s,max}$, $i_{s,max}$ and machine parameters, thus not allowing undervoltage or overcurrent operations, where $\omega_{e,demag}$ can be calculated beforehand through computational graphical or iterative methods and implemented as a constant in the code that will execute the PMSM control. Since all the machine parameters, maximum stator voltage and maximum stator current are constant, $\omega_{e,demag}$ will also be constant, and the control will be possible. However, a constant $v_{s,max}$ is not a good assumption, since in traction applications, the DC bus voltage changes according to the battery state of charge.

Another proposed solution, the one that will be used in this research, is to not calculate $\omega_{e,demag}$ and use other means to determine if $|\omega_e| \leq \omega_{e,demag}$ or $|\omega_e| > \omega_{e,demag}$ without making this direct comparison. It is defined the MTPV stator current as

$$i_{s,MTPV} = \sqrt{i_{d,MTPV}^2 + i_{q,MTPV}^2} \tag{2.80}$$

that indicates the magnitude of the stator current necessary to follow the MTPV trajectory for a certain known ω_e. It is worth noticing that $i_{s,MTPV}$ is only a function of the machine parameters, $v_{s,max}$, $i_{s,max}$ and ω_e, and it is independent of the reference current $i_{s,ref}$. As seen in Figure 2.43, for any $|\omega_e| < \omega_{e,demag}$, $i_{s,MTPV} > i_{s,max}$, for $|\omega_e| = \omega_{e,demag}$, $i_{s,MTPV} = i_{s,max}$, and for any $|\omega_e| > \omega_{e,demag}$, $i_{s,MTPV} < i_{s,max}$. Therefore, even though the exact value of $\omega_{e,demag}$ is still unknown, the easily calculable $i_{s,MTPV}$ can be used to determine if the MTPV trajectory must be followed or not, similarly to Case 2. The MTPV current $i_{s,MTPV}$ as a function of the speed can be seen in Figure 2.44, being similar in shape to the upper limit current $i_{s,upplim}$ from Case 2, with a similar interpretation as well. To plot the vertical line indicating $\omega_{e,demag}$, said speed was calculated beforehand by using computational methods, and it is valid for this case with the specific parameters already given.

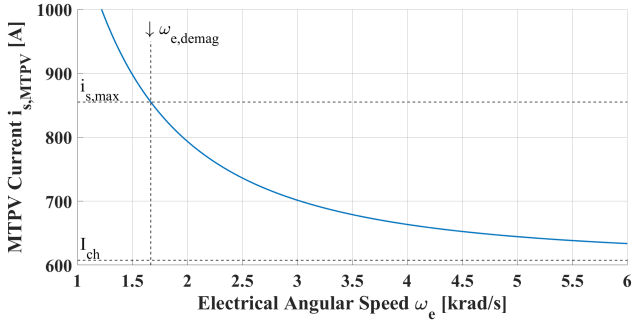

Figure 2.44: Case 4 MTPV Current

The CLC, MTPA and MTPV trajectories along with the VLEs for the base, critical and demagnetizing speeds are seen in Figure 2.45, along with the trajectories for some representative speeds. For illustration purposes, $\omega_{e,demag}$ was calculated through computational methods for its VLE to be plotted accurately.

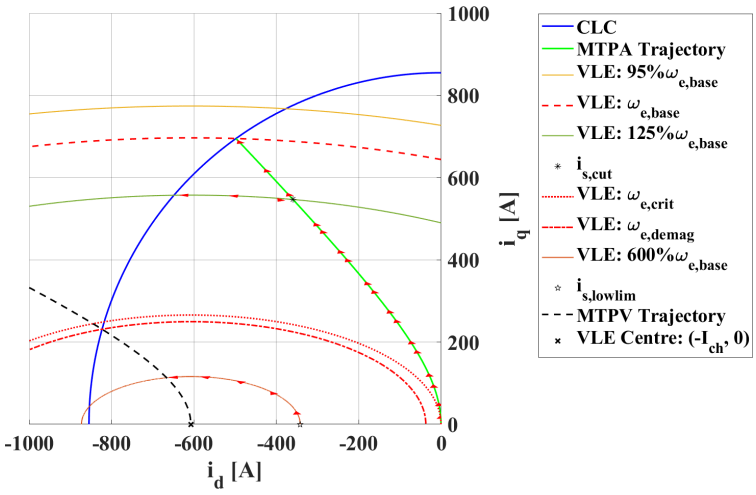

Figure 2.45: Case 4 Trajectories

Even though the expression for $\omega_{e,demag}$ for Case 4 is not known, it can be concluded graphically that it is proportional to $v_{s,max}$, and inversely proportional to $i_{s,max}-I_{ch}$, similarly to the expression for the demagnetizing speed for Case 2 from (2.45).

The discussion of the independence between $\omega_{e,demag}$ and $\omega_{e,crit}$ from Case 2 is also valid for Case 4, and the current speed must be compared to the demagnetizing speed for any speed above the base – having in mind that for Case 4 this evaluation will be done by comparing $i_{s,MTPV}$ to $i_{s,max}$. Therefore, the algorithm for Case 4 can be presented as

$$\text{Case 4 Trajectory 1 MTPA} \begin{cases} |\omega_e| \leq \omega_{e,base} \\ 0 \leq |i_{s,ref}| \leq i_{s,max} \\ i_{d,ref} = \dfrac{\lambda_{pm} - \sqrt{\lambda_{pm}^2 + 8(L_q - L_d)^2 i_{s,ref}^2}}{4(L_q - L_d)} \\ i_{q,ref} = \text{sgn}(i_{s,ref})\sqrt{i_{s,ref}^2 - i_{d,ref}^2} \end{cases} \tag{2.81}$$

$$\text{Case 4 MTPV} \begin{cases} |\omega_e| > \omega_{e,base} \\ i_{s,MTPV} < i_{s,max} \\ i_{s,upplim} = i_{s,MTPV} \end{cases} \tag{2.82}$$

$$\text{Case 4 Trajectory 2 VCLTM} \begin{cases} \omega_{e,base} \leq |\omega_e| \leq \omega_{e,crit} \\ 0 \leq |i_{s,ref}| \leq i_{s,cut} \\ i_{d,ref} = \dfrac{\lambda_{pm} - \sqrt{\lambda_{pm}^2 + 8(L_q - L_d)^2 i_{s,ref}^2}}{4(L_q - L_d)} \\ i_{q,ref} = \text{sgn}(i_{s,ref})\sqrt{i_{s,ref}^2 - i_{d,ref}^2} \end{cases} \tag{2.83}$$

$$\text{Case 4 Trajectory 3 VCLTM} \begin{cases} \omega_{e,base} \leq |\omega_e| \leq \omega_{e,crit} \\ i_{s,cut} \leq |i_{s,ref}| \leq i_{s,upplim} \\ i_{d,ref} = \dfrac{-k_5 + \sqrt{k_5^2 - 4k_4k_6}}{2k_4} \\ i_{q,ref} = \text{sgn}(i_{s,ref})\sqrt{i_{s,ref}^2 - i_{d,ref}^2} \end{cases} \tag{2.84}$$

$$\text{Case 4 Trajectory 4 VCLTM} \begin{cases} |\omega_e| \geq \omega_{e,crit} \\ i_{s,lowlim} \leq |i_{s,ref}| \leq i_{s,upplim} \\ i_{d,ref} = \dfrac{-k_5 + \sqrt{k_5^2 - 4k_4k_6}}{2k_4} \\ i_{q,ref} = \text{sgn}(i_{s,ref})\sqrt{i_{s,ref}^2 - i_{d,ref}^2} \end{cases} \tag{2.85}$$

In a similar way to all the other cases, the currents, voltages, torque and power for Case 4 will be evaluated. However, for this case only, the demagnetizing speed was calculated beforehand by solving (2.79) in MATLAB's equation solver only to plot the vertical line that denotes it. The current references were obtained by comparing $i_{s,MTPV}$ with $i_{s,max}$ for all $\omega_e > \omega_{e,base}$, as proposed. Even though plotted in the same figures, the algorithm does not have the value of $\omega_{e,demag}$. For the maximum torque scenario, the dq-frame currents and voltages are seen in Figures 2.46a and 2.46b, respectively.

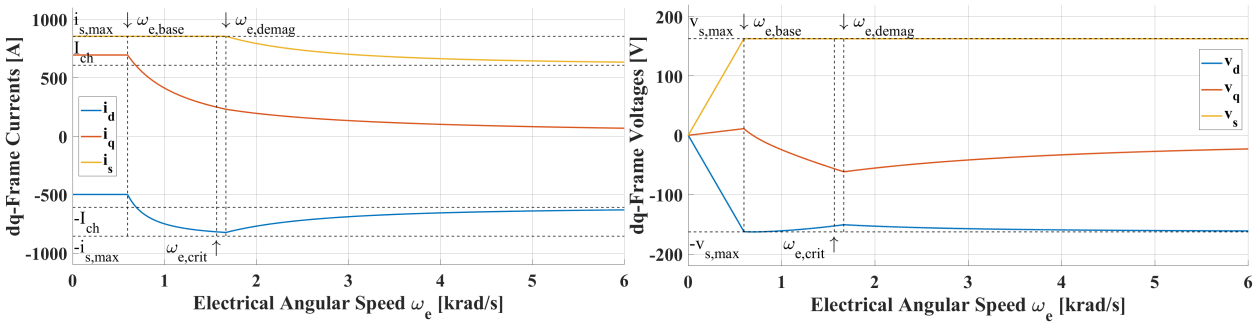

(a) Currents (b) Voltages

Figure 2.46: Case 4 dq-Frame Currents and Voltages for Maximum Torque

Still the maximum torque scenario, the mechanical torque and power are seen in Figures 2.47a and 2.47b, respectively.

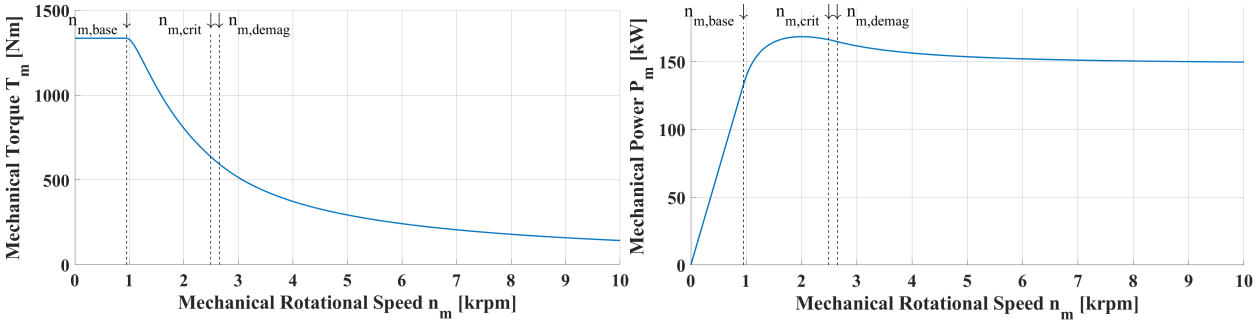

(a) Torque (b) Power

Figure 2.47: Case 4 Torque and Power for Maximum Torque

For a no torque production, the currents and voltages are seen in Figures 2.48a and 2.48b, respectively.

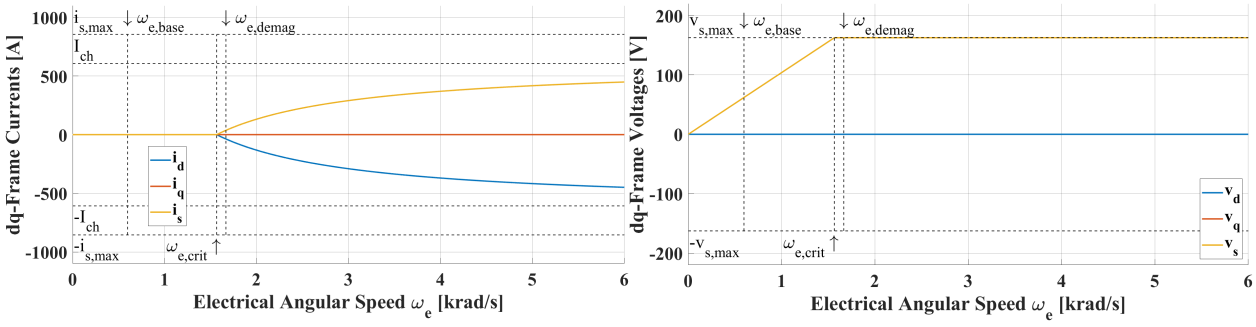

(a) Currents (b) Voltages

Figure 2.48: Case 4 dq-Frame Currents and Voltages for Zero Torque

It can be noticed in Figure 2.47b that the power does not peak at $\omega_e = \omega_{e,demag}$ and stays constant after, in contrast to Case 2, but rather peaks at $\omega_e < \omega_{e,demag}$. It is seen in Figure 2.46a that the peak negative value for i_d is higher in magnitude than I_{ch}, meaning that the permanent magnets will not only be demagnetized, but also remagnetized in the opposite polarity.

2.3.5 Special Case: PMSM with $I_{ch} = i_{s,max}$

For any rotor configuration, if $I_{ch} = i_{s,max}$, it can be interpreted either as a finite speed machine with $\omega_{e,max} = \infty$, according to (2.37), or a theoretically infinite speed machine with $\omega_{e,demag} = \infty$, according to (2.45). Therefore, any of the two algorithms presented can be used: if the finite speed algorithm is employed, the machine will never be able to reach its maximum speed; if the theoretically infinite speed algorithm is employed, the machine will never reach its demagnetizing speed. Its torque and power profiles are similar to the ones from a high speed machine. For practical applications, the PMSM with $I_{ch} = i_{s,max}$ can be considered an in theory infinite speed machine that can be controlled with the finite speed machine algorithm.

2.3.6 Finite Speed PMSM Operation At or Above the Maximum Speed

It was already discussed that a finite speed PMSM (Cases 1 and 3) will reach a speed $|\omega_e| = \omega_{e,max}$ in which no torque can be produced, thus the machine can no longer accelerate, even in the ideal frictionless scenario. Having no torque also means that the machine cannot brake, thus a frictionless ideal load that allows $|\omega_{e,ss}| = \omega_{e,max}$ will not allow the machine to leave said operation point. This operating point, however, is unachievable in practice, and even with low friction, $|\omega_{e,ss}| < \omega_{e,max}$, allowing the machine to generate a torque that opposes $\omega_{e,ss}$.

A zero torque operation does not prevent the machine from being accelerated by external forces. If this happens, and the machine operates at $|\omega_e| > \omega_{e,max}$, the voltage and current constraints can no longer be simultaneously satisfied, since the voltage-limiting circle/ellipse will be located completely out of the current limiting circle, thus there will be no possible VCLMT operating point.

To maintain a non-saturated control of the machine, the present research will create a

current reference $i_{s,ref} = i_{s,lowlim} > i_{s,max}$, thus violating the current constraint. By operating also above the critical speed, the algorithm will use Region 4 to decompose $i_{s,ref} = i_{s,lowlim}$ into $i_{d,ref} = -i_{s,lowlim}$ and $i_{q,ref} = 0$, being able to respect the voltage limit and maintain a proper control.

2.4 User Input and the Generation of $i_{s,ref}$

So far, Chapter 2 discussed how to optimally decompose $i_{s,ref}$ into $i_{dq,ref}$, however it was implied that $i_{s,ref}$ was already existing. This section will discuss how to obtain $i_{s,ref}$ from an user input u_i. The user input will be defined as a per-unit value $-1 \leq u_i \leq 1$, where $u_i = 0$ indicates a command for the machine to not produce any torque (also known as "coasting"), $u_i = 1$ indicates a command for the machine to produce the maximum torque available for its current speed (or maximum positive acceleration possible), and $u_i = -1$ indicates the maximum negative torque available for its current speed (or maximum negative acceleration possible). "Positive acceleration" denotes an acceleration towards the positive rotation, and "negative acceleration" denotes an acceleration towards the negative rotation. The operation of the machine as a motor or as a generator will depend if the torque and speed have the same direction of rotation or not, respectively.

It must be taken into consideration the fact that the minimum and maximum values for $i_{s,ref}$ are not constant, since depending on the region of operation it can assume $i_{s,lowlim} > 0$ and/or $i_{s,upplim} < i_{s,max}$, as already discussed in the present chapter. Therefore $i_{s,ref} = u_i i_{s,max}$ might generate a reference current that lies outside of its possible limits. By simply limiting the generated $i_{s,ref}$ to its two limits, it will create "dead zones" in the user input, meaning that if $i_{s,lowlim} > 0$, an user input in the range $0 \leq |u_i| \leq {}^{i_{s,lowlim}}/_{i_{s,max}}$ will create the same zero torque reference, and if $i_{s,upplim} < i_{s,max}$ an user input in the range ${}^{i_{s,upplim}}/_{i_{s,max}} \leq |u_i| \leq i_{s,max}$ will create the same maximum torque reference. To overcome this issue, it is desired that $0 \leq |u_i| \leq 1$ will create $i_{s,lowlim} \leq |i_{s,ref}| \leq i_{s,upplim}$, where $0 \leq i_{s,lowlim}$ and $i_{s,upplim} \leq i_{s,max}$. Therefore, considering the four-quadrant operation, $i_{s,ref}$ can be related to u_i for a finite speed PMSM as

$$i_{s,ref} = \begin{cases} \text{sgn}(u_i)\left(|u_i|\left(i_{s,upplim} - i_{s,lowlim}\right) + i_{s,lowlim}\right) & \text{for } u_i \neq 0 \\ & \text{and } |\omega_e| \leq \omega_{e,max} \\ i_{s,lowlim} & \text{for } u_i = 0 \\ & \text{or } |\omega_e| > \omega_{e,max} \end{cases} \tag{2.86}$$

and for an in theory infinite speed PMSM as

$$i_{s,ref} = \begin{cases} \text{sgn}(u_i)\left(|u_i|\left(i_{s,upplim} - i_{s,lowlim}\right) + i_{s,lowlim}\right) & \text{for } u_i \neq 0 \\ i_{s,lowlim} & \text{for } u_i = 0 \end{cases} \tag{2.87}$$

For the purposes of generating the reference current, $i_{s,upplim}$ is set as $i_{s,max}$ for a finite speed PMSM or if $|\omega_e| \leq \omega_{e,demag}$ for a theoretically infinite speed PMSM, and $i_{s,lowlim}$ is set as 0 for any machine if $|\omega_e| \leq \omega_{e,crit}$.

2.5 Complete Wide Speed Operation Algorithm

Having how to generate $i_{s,ref}$ and how to decompose it in $i_{dq,ref}$, the complete algorithm for a wide speed operation of a finite speed PMSM can be seen in Figure 2.49, while for an in theory infinite speed PMSM can be seen in Figure 2.50

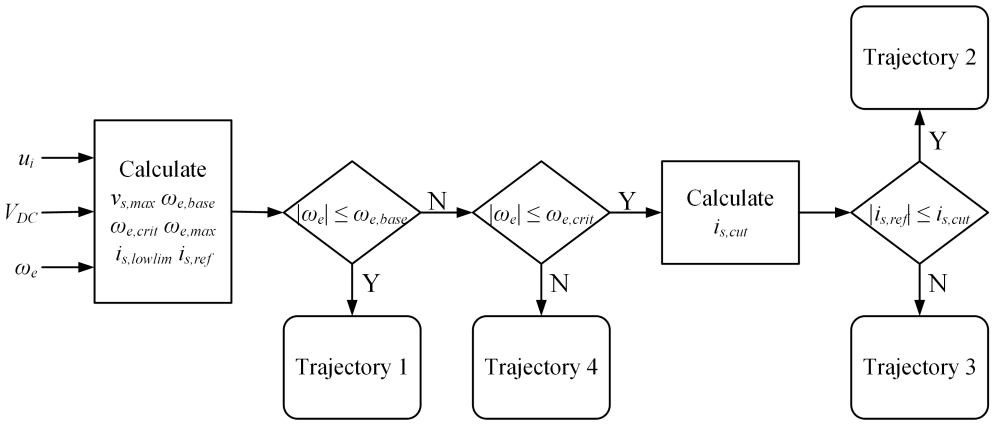

Figure 2.49: Finite Speed PMSM Algorithm

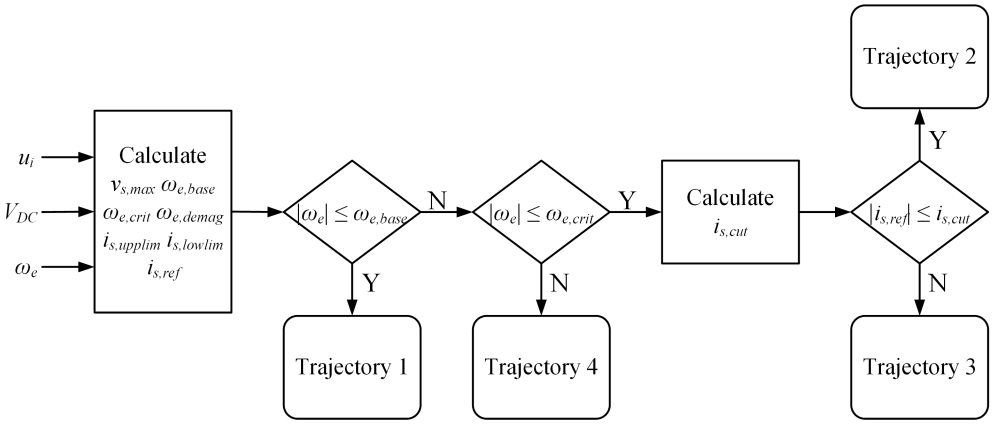

Figure 2.50: Theoretically Infinite Speed PMSM Algorithm

2.6 Complete Control System

The last signal processing that needs to be done is how to obtain the machine speed by having its position information. It is known that the angular speed is the variation of the angular position with respect to time:

$$\omega_m = \frac{d\theta_m}{dt} \tag{2.88}$$

In a discrete domain, with a sufficiently high-rate sampling, (2.88) can be discretized as

$$\omega_m(k) = \frac{\theta_m(k) - \theta_m(k-1)}{T_s} \tag{2.89}$$

With all parts of the control system discussed, it can be shown in its complete form in Figure 2.51.

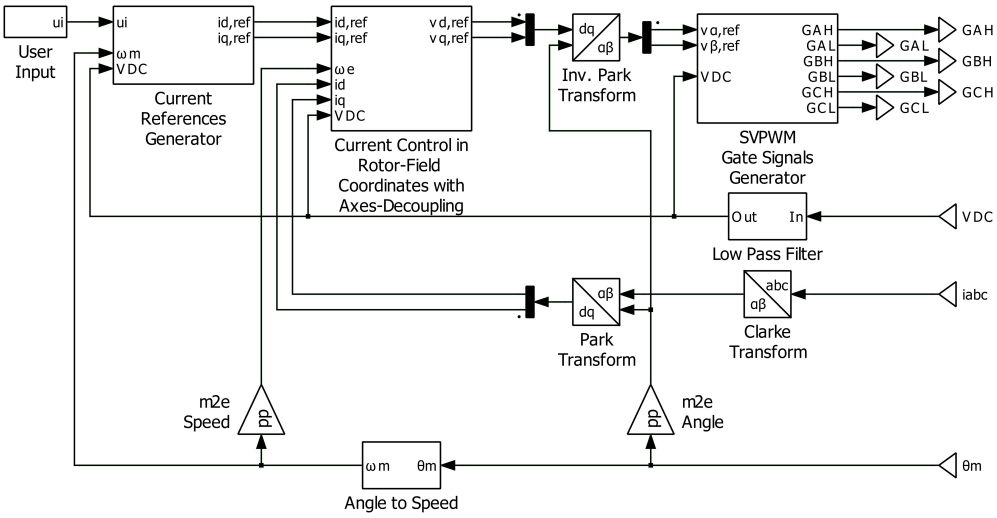

Figure 2.51: Complete Control System

On the left side of Figure 2.51 is where the driver/rider input is, and on the right side is where the signals to/from the VSC and machine are located. The subsystems denoted by boxes with inputs and outputs were discussed previously:

- Current References Generator: discussed in Chapter 2
- Clarke, Park, and Inverse Park Transforms: matrix operations shown in Equations (1.6), (1.8) and (1.9), respectively
- Current Control in Rotor Field Coordinates with Axes-Decoupling: shown in Figure 1.8
- SVM Gate Signals Generator: shown in section 1.2.2.1
- Angle to Speed: from Equation (2.89)
- Mechanical to Electrical Angle and Speed: shown in Equations (1.44) and (1.45), respectively

2.7 Impacts of Lower DC Link Voltage: Undervoltage Operation

So far, the currents, voltages, torque and power curves were shown for a machine operation with a DC link voltage equals to its rated – therefore maximum – value, $V_{DC,max}$. However it

is possible for the algorithm to generate the reference dq-currents for a DC link voltage V_{DC} that has a value lower than its maximum, as long as the V_{DC} value is used to recalculate $v_{s,max}$ from (2.26). If V_{DC} is kept at its maximum value in the algorithm while its real value is lower, the algorithm will create current references that will not be possible to be followed due to the lack of voltage, creating an overmodulation operation or even system instability.

For a lower DC link voltage, there will be less voltage that the VSC can impose to the PMSM to counter its back-EMF, therefore the field-weakening region will happen in a lower speed than for a higher V_{DC}. The base speed $\omega_{e,base}$ for a lower DC link voltage will also be lower, and the torque will start to decrease at lower speeds, also making that the maximum speed $\omega_{e,max}$ is lower.

Even though the base speed $\omega_{e,base}$ (2.24), critical speed $\omega_{e,crit}$ (2.31), maximum speed $\omega_{e,max}$ (2.37) and demagnetizing speed $\omega_{e,demag}$ (2.45) are all linearly proportional to $v_{s,max}$, it is worth mentioning that a decrease of the DC link voltage V_{DC} by a certain factor will not result in a decrease of the maximum stator voltage $v_{s,max}$ by the same factor, since the resistive voltage drop given by $R_s i_{s,max}$ in (2.26) remains constant. Therefore, a decrease of the DC link voltage V_{DC} by a certain factor will also not result in a decrease of all mentioned speeds by the same factor – but it can be similar, especially for high-powered machines characterized by a low resistive voltage drop.

Due to the resistive voltage drop, there is a minimum DC link voltage for the machine to develop its full torque. It is given by

$$V_{DC,min} = \begin{cases} \sqrt{3} R_s i_{s,max} & \text{for SPWM} \\ \dfrac{3}{2} R_s i_{s,max} & \text{for SVM} \end{cases} \tag{2.90}$$

For $V_{DC} = V_{DC,min}$, the machine will achieve its full torque at zero speed, however will lose all its torque for any non-zero speed. For any $V_{DC} < V_{DC,min}$, the maximum stator current will be limited to $i_{s,max,lim} = {}^{V_{DC}}/_{\sqrt{3}R_s}$ for SPWM or $i_{s,max,lim} = {}^{2V_{DC}}/_{3R_s}$ for SVM, and the machine will also lose all its already reduced torque for any non-zero speed.

The maximum torques and powers obtained from the machine from Case 1 for a changing DC link voltage are seen in Figures 2.52a and 2.52b, respectively.

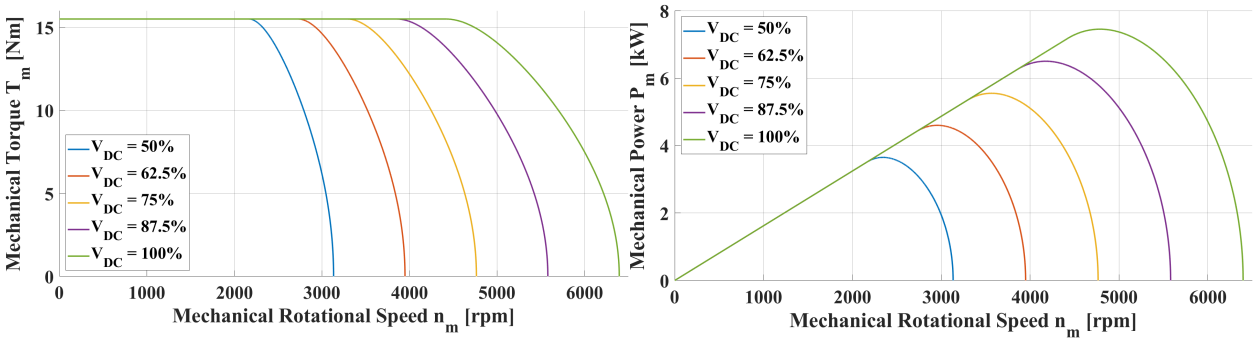

(a) Torque

(b) Power

Figure 2.52: Undervoltage Operation Effect on the PMSM Performance

2.8 Impacts of Higher Stator Current: Overcurrent Operation

It is also possible to submit the machine to overcurrents to achieve a higher momentary performance. PMSM manufacturers usually dictates how much overcurrent their machines can be submitted to, and for how long – usually in the tens of seconds range.

The algorithm presented in this research will not violate $i_{s,max}$, unless for a finite speed PMSM operating over $\omega_{e,max}$. To allow the machine to operate in an overcurrent mode, $i_{s,max}$ needs to be changed and all the parameters recalculated. The maximum stator voltage $v_{s,max}$ will be slightly reduced due to an increased resistive voltage drop, as seen in (2.26). The base and critical speeds $\omega_{e,base}$ and $\omega_{e,crit}$ will also be reduced, meaning that the machine will enter the field-weakening mode at lower speeds. However, the change in the maximum speed $\omega_{e,max}$ cannot be guaranteed to increase or decrease. If the PMSM has a high resistive voltage drop, the numerator on the maximum speed equation (2.37) will decrease more than its denominator, thus reducing $\omega_{e,max}$. For PMSMs with low resistive voltage drop, which are likely to be used in traction applications, $\omega_{e,max}$ is likely to rise within reasonable overcurrent values.

Since the definition that dictates if a PMSM has a maximum speed or not is given by the ratio $I_{ch}/i_{s,max}$, increasing the maximum stator current can move an SPMSM from Case 1 to Case 2, and an IPMSM from Case 3 to Case 4. Since this can occur, the code implemented in the DSP controlling the PMSM must take the case-change scenario into consideration and be programmed to switch between algorithms. The machine used as example in Case

1 is unlikely to suffer this case-change, since $^{I_{ch}}/_{i_{s,max}} \approx 3.542$ indicates that it needs to be submitted to an overcurrent of 254.2% to change to Case 2, while the machine used as example in Case 3 has $^{I_{ch}}/_{i_{s,max}} \approx 1.066$, meaning that a small 6.6% overcurrent operation will change it to Case 4, as demonstrated previously.

The machine fitted in Case 1 will be used to discuss the impacts of overcurrent operation, as it does not have a high resistive voltage drop or change cases when submitted to a 100% overcurrent operation. Its torque and power profiles can be seen in Figures 2.53a and 2.53b, respectively.

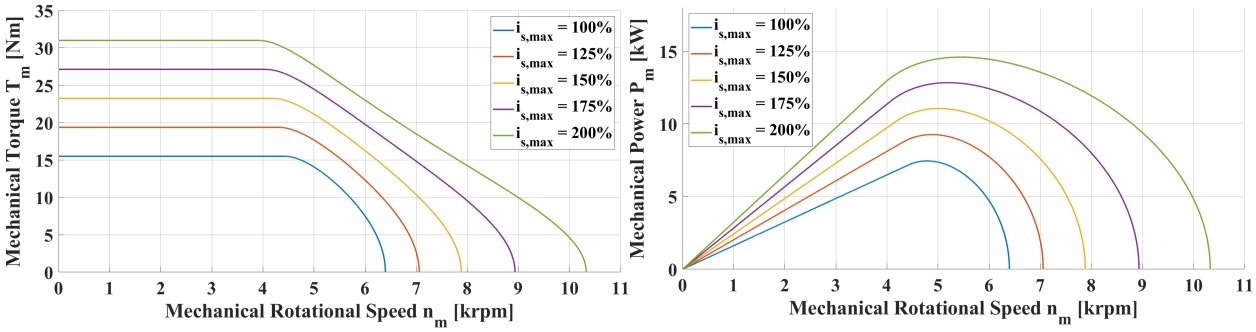

(a) Torque (b) Power

Figure 2.53: Overcurrent Operation Effect on the PMSM Performance

2.9 Impacts of the Resistive Voltage Drop

It was defined that $v_{s,max}$ is the maximum stator voltage considering the maximum resistive voltage drop by the term $R_s i_{s,max}$ that subtracts $^{V_{DC}}/_{\sqrt{3}}$ or $^{2V_{DC}}/_{3}$ in (2.26). It is defined the stator voltages in the dq-frame considering the voltage drop from (2.17)–(2.18) in steady state as

$$v_{dr} = -\omega_e L_q i_q + R_s i_d \tag{2.91}$$

$$v_{qr} = \omega_e \left(L_d i_d + \lambda_{pm}\right) + R_s i_q \tag{2.92}$$

$$v_{sr} = \sqrt{v_{dr}^2 + v_{qr}^2} \tag{2.93}$$

and the steady state stator voltages without the resistive voltage drops as

$$v_{dnr} = -\omega_e L_q i_q \tag{2.94}$$

$$v_{qnr} = \omega_e \left(L_d i_d + \lambda_{pm} \right) \tag{2.95}$$

$$v_{snr} = \sqrt{v_{dnr}^2 + v_{qnr}^2} \tag{2.96}$$

Then, the stator voltage drop caused by the stator resistance is defined as

$$v_r = v_{sr} - v_{snr} \tag{2.97}$$

For Case 1, v_r is plotted as a function of ω_e in the four torque-speed quadrants, and it is seen in Figure 2.54. For this case, the maximum resistive voltage drop is around $7.41V$, which represents around 2% of $v_{s,max}$ when the DC-link voltage is the maximum $640V$.

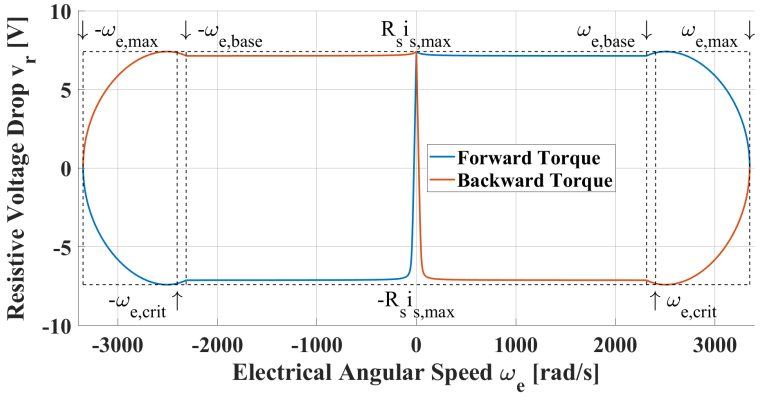

Figure 2.54: Resistive Voltage Drop for Maximum Torques

It can be seen in Figure 2.54 that the voltage drop caused by the stator resistance is not constant for the entire machine speed range. This is due to the fact that the terms $R_s i_d$ and $R_s i_q$ do not increase v_d and v_q in magnitude in the same manner, respectively, mainly because the resistive voltage drops does not necessarily have the same polarity as the other terms in (2.91) and (2.92).

It is noticeable that even though not constant, the voltage drop peaks at $R_s i_{s,max}$, resulting in a spare stator voltage for any other speeds. It is also interesting the fact

that the voltage drops almost reaches zero at $|\omega_e| = \omega_{e,max}$. However, the voltage drop at the maximum speed is a small positive value, around $75.7mV$ equal for both forward and backward torque plots, since the dq-frame currents at the maximum speed are the same for both torque directions. While in the generator mode, the machine presents mostly a negative voltage drop, meaning that the voltage needed to impose the dq-frame currents generated by the presented algorithm for maximum torque will be less than the voltage needed to keep said currents at zero torque. If the PMSM is used as only a generator the maximum resistive voltage drop used to calculate $v_{s,max}$ is not equal to $R_s i_{s,max}$, but rather a smaller value.

2.10 Practical Considerations

So far, all calculations were based without considering magnetic saturation, demagnetization of the permanent magnets and machine overheating. When implementing the algorithms presented, these factors need to be taken into consideration.

2.10.1 Magnetic Saturation

When operating with nominal current and voltage values, the PMSM will not suffer from excessive magnetic saturation in its stator and rotor soft magnetic materials, since the machine fluxes will either have nominal values (when operating below the base speed) or reduced values (when operating over the base speed). However, when operating under overcurrent, as discussed in section 2.8, its magnetic fluxes will reach values higher than their nominal ones. The overcurrent operation needs to be verified with the PMSM manufacturer to prevent excessive magnetic saturation.

2.10.2 Permanent Magnet Demagnetization

When operating above the base speed, the negative d-axis current creates a d-axis magnetic flux that opposes the one naturally present in the permanent magnets. For Case 2, the permanent magnets can be completely demagnetized when operating above the demagnetizing speed $\omega_{e,demag}$, and, for Case 4, there will be a negative d-axis current greater in magnitude than I_{ch}, meaning that the permanent magnets will not only be demagnetized, but remagnetized on the opposite polarity. The PMSM machine needs to be verified if able to suffer demagnetization, and, if so, how much. This information is provided by its

manufacturer.

2.10.3 Thermal Constraints

The heat caused by internal friction, ohmic losses and iron losses needs to be extracted for a proper machine operation. Even with proper cooling under nominal conditions, overcurrent operation can cause an excessive temperature increase, thus the PMSM manufacturers usually allow an overcurrent operation for a limited amount of time, then require the machine to return to its nominal temperature before being submitted to another overcurrent operation.

Chapter 3

Simulation Results

The algorithms presented and mathematically tested in Chapter 2 will be implemented in the software PLECS. For all four cases, a 2-level VSC will be used along a voltage source, and the measurements taken will be the DC link voltage V_{DC}, the abc-frame currents i_{abc} and the mechanical position of the rotor θ_m. The model can be seen in Figure 3.1.

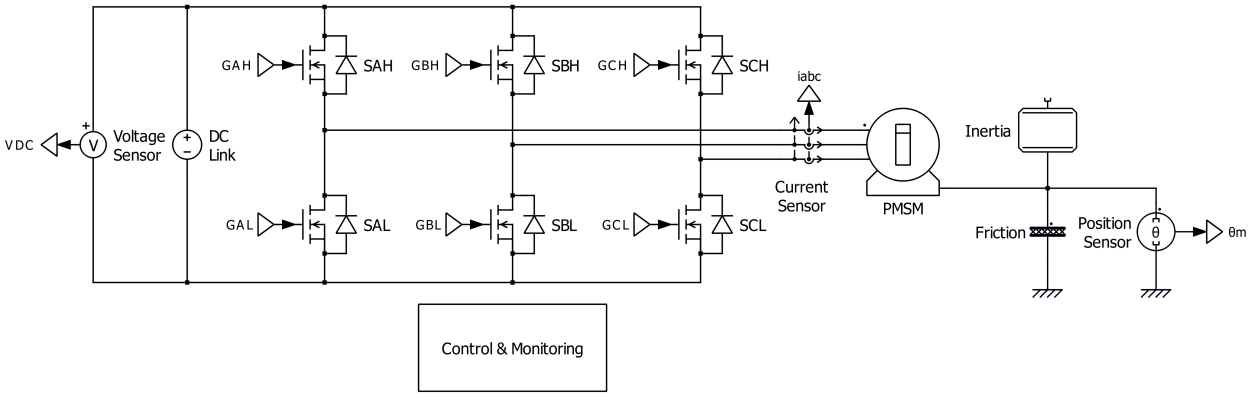

Figure 3.1: PLECS Simulation Model

The mechanical load is a friction-inertia load. For analysis purposes, in most of the simulations the friction will be set to zero, allowing the algorithm to be tested for high speeds, up to $\omega_{e,max}$ for the finite PMSMs. The inertia will be prioritized, having a value that dictates the desired acceleration. The subsystem "Control & Monitoring" contains the control system, already shown in Figure 2.51. All four cases will be simulated using the same system, with the only change being the system parameters and control algorithm.

It is worth noticing that the algorithm is load-independent, and the mechanical load behaviour does not impact the generation of reference currents, thus the values for the friction and inertia are for illustration purposes only.

3.1 Case 1: Finite Speed SPMSM

The machine used to illustrate Case 1 in Chapter 2 will be used for the simulation as well. However, since it will also be used for the experimental setup, the DC link voltage and the maximum stator current were reduced, from $640V$ to $200V$ and from $13.72A$ to $10A$, in order to reduce the base speed to mechanically achievable levels and to not overload the mechanical load, respectively. The new dq-frame currents, torque and power profiles are seen in Figures 3.2, 3.3a and 3.3b, respectively.

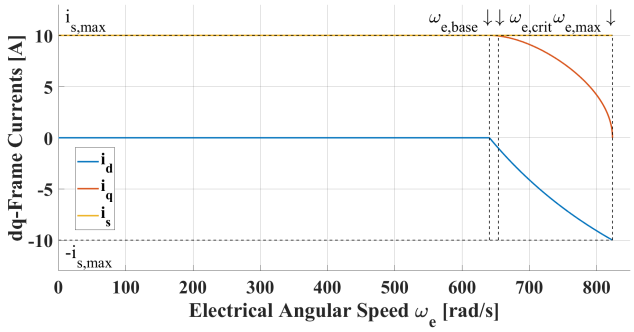

Figure 3.2: Case 1 Simulation Calculated Currents for Maximum Torque

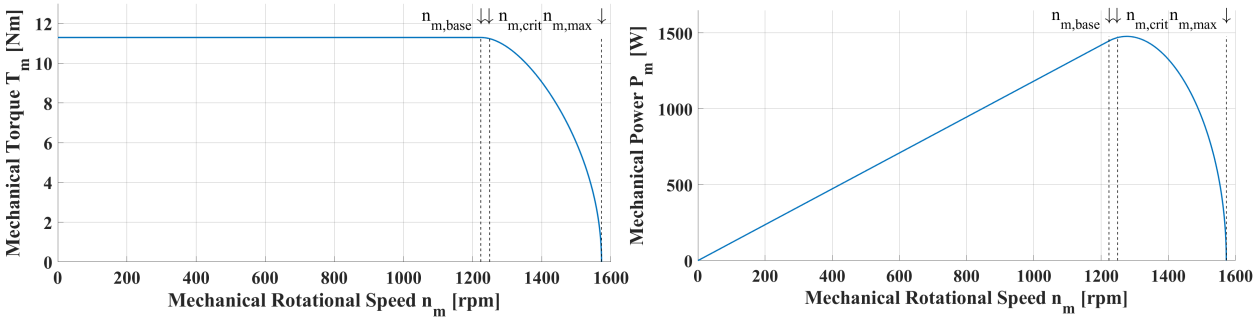

(a) Torque

(b) Power

Figure 3.3: Case 1 Simulation Calculated Torque and Power for Maximum Torque

3.1.1 Simulation 1: Four Quadrant Operation

The first simulation will test the algorithm's ability to operate in all torque-speed quadrants. The simulation begins with the system stopped, and, at $t = 100ms$, u_i is set to 1, to generate maximum forward torque. At $t = 500ms$, after the system reached $\omega_{e,ss} = \omega_{e,max}$, u_i is set to -1, to generate maximum backward torque. After reaching $\omega_{e,ss} = -\omega_{e,max}$, u_i is set to 1 at $t = 1.2s$, and the simulation stops shortly after at $t = 1.6s$ when the machine speed

is positive again. This covers all four torque-speed quadrants. The dq-frame currents are shown in Figure 3.5a, along with the machine speed in Figure 3.4. For better understanding, the dq-frame currents are plotted as a function of the machine speed, as seen in Figure 3.5b.

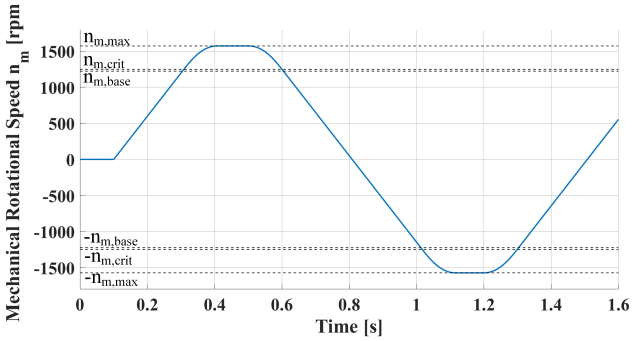

Figure 3.4: Case 1 Simulation 1 PMSM Speed

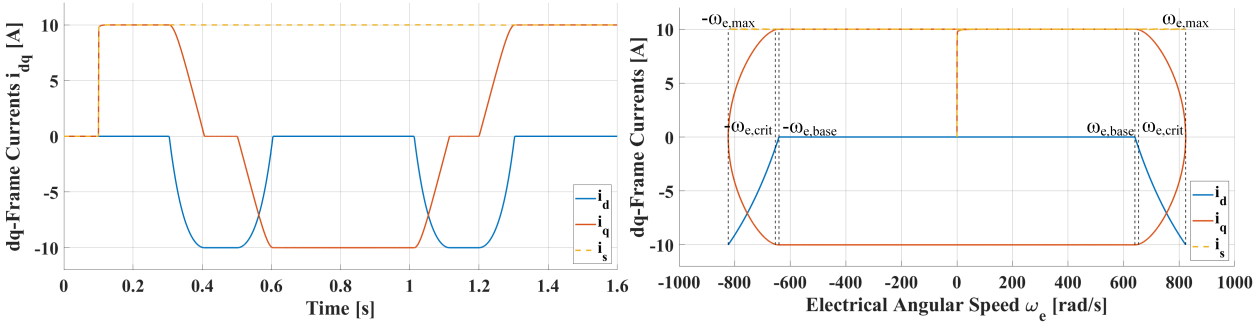

(a) Time Domain

(b) Speed Domain

Figure 3.5: Case 1 Simulation 1 dq-Frame Currents

Figure 3.5b shows the behaviour of the dq-frame currents with respect to the speed. As expected, the stator current is dedicated only to the q-axis current to generate torque for any speed $|\omega_e| < \omega_{e,base}$. For speeds $\omega_{e,base} < |\omega_e| < \omega_{e,max}$ there is a d-axis current being used for field-weakening purposes, proportional to the speed, up to the point where $|\omega_e| = \omega_{e,max}$, when the stator current is entirely used for field-weakening, and no torque is generated, and the machine reaches its steady state speed. The torque, being only a function of i_q, is reduced for speeds over the base, as seen in Figure 3.6a, and, similarly, the machine power in Figure 3.6b.

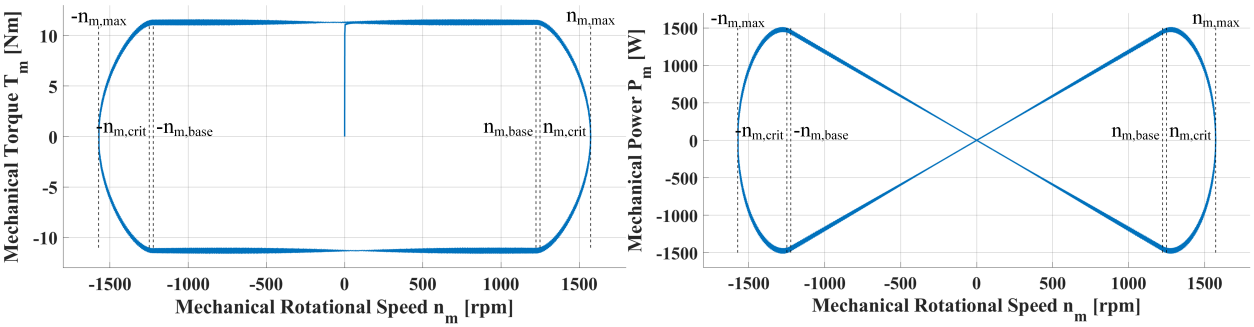

(a) Torque (b) Power

Figure 3.6: Case 1 Simulation 1 Four Quadrants Operation

To verify the machine voltages, it is plotted the reference voltages in the αβ-frame, the signals used for the SVM block. These voltages are seen in Figure 3.7.

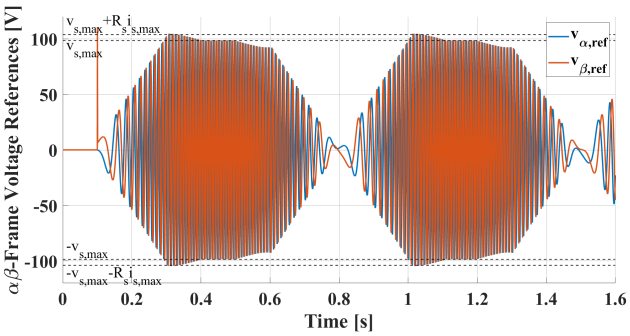

Figure 3.7: Case 1 Simulation 1 αβ-Frame Voltage References

It is noticeable in Figure 3.7 that the voltage references – the voltages needed to impose the reference currents generated by the algorithm – do not behave exactly like the ones calculated in Chapter 2. This is due to the fact that the voltages were calculated assuming a steady state, thus neglecting the derivative of the magnetic fluxes and the resistive voltage drop in (1.41)–(1.42).

3.1.2 Simulation 2: Coasting at the Field Weakening Region

The second simulation will test the algorithm's capability of producing zero torque at the field weakening region. For this simulation, the load friction will be higher than zero, so the steady state speed is below the maximum and the system will decelerate when no torque is produced. For this, u_i is set to 1 at $t = 100ms$, and to 0 at $t = 1s$. The dq-frame currents are seen in Figure 3.8a, and the system speed is seen in Figure 3.8b.

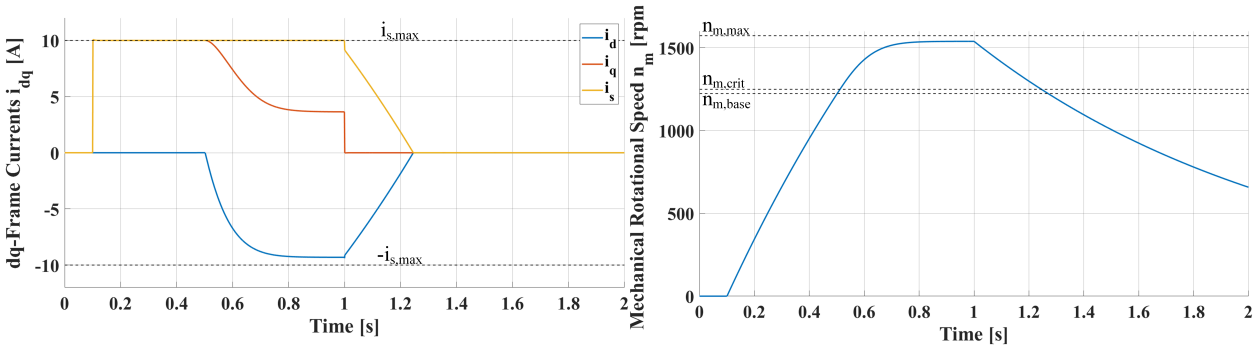

(a) dq-Frame Currents in the Time Domain

(b) System Speed

Figure 3.8: Case 1 Simulation 2

It is noticeable in Figures 3.8a and 3.8b that the d-axis current starts to be negative when the system reaches the base speed while under $u_i = 1$, and it returns to zero when the system goes below the critical speed while under $u_i = 0$, as expected. This is clearly seen when the dq-frame currents are plotted in the machine speed domain in Figure 3.9, where the arrows point the direction in which the dq-frame currents move with respect to time.

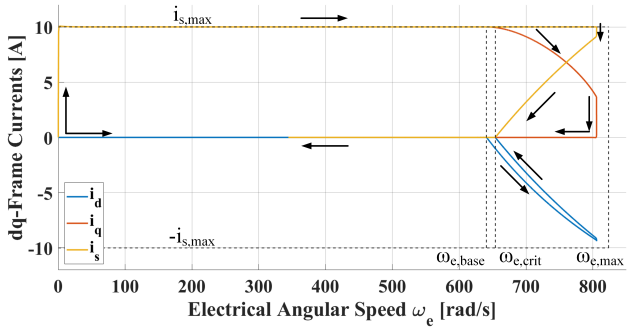

Figure 3.9: Case 1 Simulation 2 dq-Frame Currents in the Speed Domain

Similarly to Simulation 1, the reference voltages in the αβ-frame are seen in Figure 3.10.

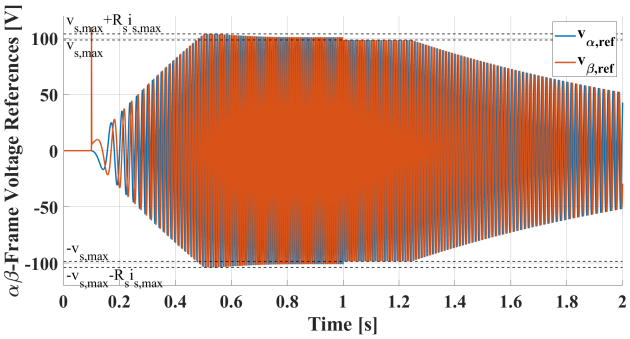

Figure 3.10: Case 1 Simulation 2 αβ-Frame Voltage References

Figures 3.7 and 3.10 shows that the voltages needed to impose the currents are within $v_{s,max} + R_s i_{s,max}$ and $v_{s,max}$, as expected, except for the transient at $t = 100ms$ due to the high magnetic flux change. The machine's torque and power profiles, dq-frame currents and base, critical and maximum speeds are the same as the calculated quantities.

3.2 Case 2: Theoretically Infinite Speed SPMSM

For Case 2, the dq-frame currents in the speed domain are seen in Figure 3.11, while the torque and power profiles are seen in Figures 3.12a and 3.12b, respectively. The switching frequency adopted is $2.7kHz$.

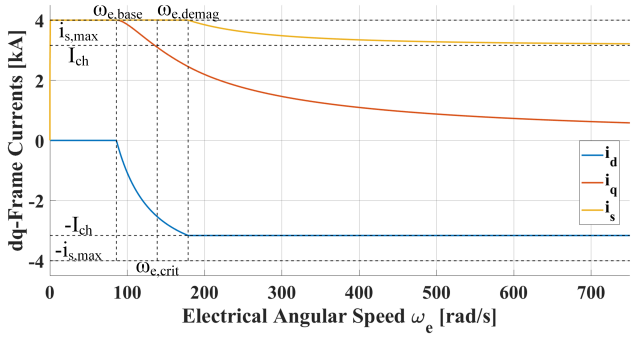

Figure 3.11: Case 2 Simulation dq-Frame Currents

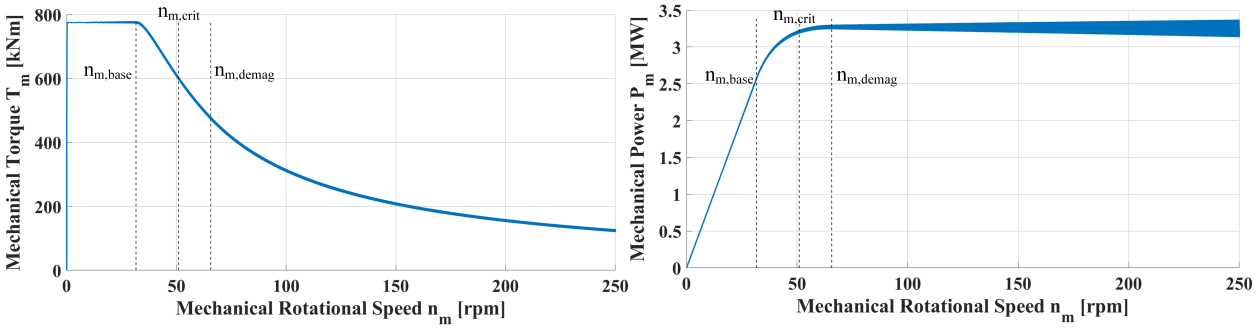

(a) Torque Profile

(b) Power Profile

Figure 3.12: Case 2 Simulation Torque and Power Profiles

All the simulated quantities are the same as the calculated ones.

3.3 Case 3: Finite Speed IPMSM

In a similar way for Case 3, the dq-frame currents in the speed domain are seen in Figure 3.13, while the torque and power profiles are seen in Figures 3.14a and 3.14b, respectively. The switching frequency adopted is $5kHz$.

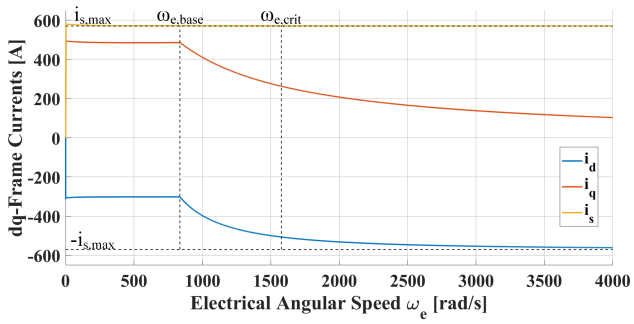

Figure 3.13: Case 3 Simulation dq-Frame Currents

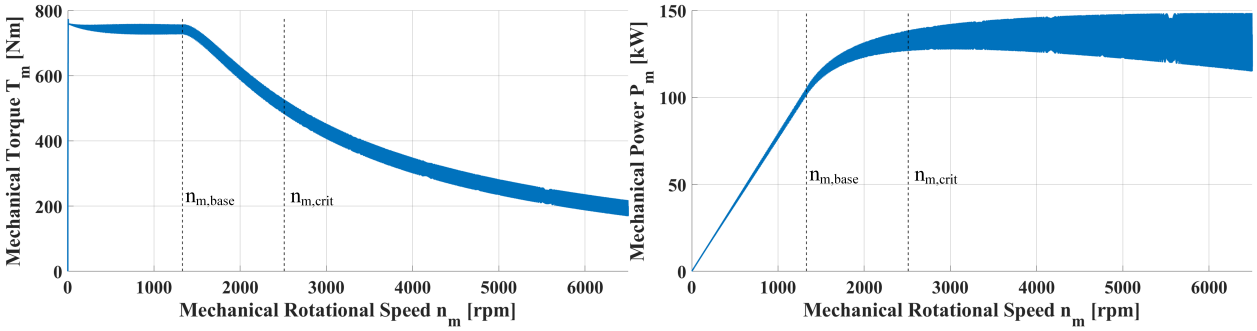

(a) Torque Profile

(b) Power Profile

Figure 3.14: Case 3 Simulation Torque and Power Profiles

All the simulated quantities are the same as the calculated ones for the speed range simulated. It is worth mentioning that even though being a finite speed PMSM, the machine used in Case 3 has a maximum speed so high that cannot be achieved by a converter using a switching frequency of $5kHz$, since its fundamental waves would be around $4.06kHz$ for the maximum speed. In the simulations, the control system collapsed when operating around $8200rpm$ with a frequency modulation index of around 6.1.

3.4 Case 4: Theoretically Infinite Speed IPMSM

Finally, for Case 4, the dq-frame currents in the speed domain are seen in Figure 3.15, while the torque and power profiles are seen in Figures 3.16a and 3.16b, respectively. The switching frequency adopted is $5kHz$, the same as Case 3.

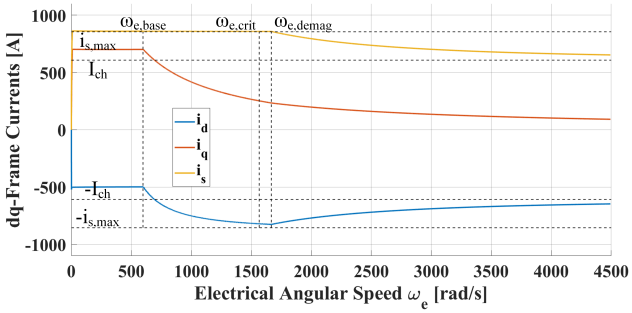

Figure 3.15: Case 4 Simulation dq-Frame Currents

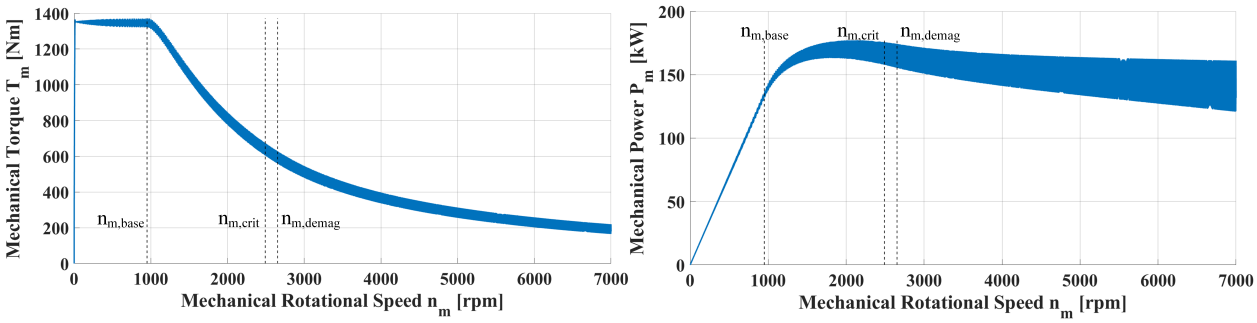

(a) Torque Profile

(b) Power Profile

Figure 3.16: Case 4 Simulation Torque and Power Profiles

All the simulated quantities are the same as the calculated ones for the speed range simulated.

Chapter 4

Experimental Results

The studied algorithm is implemented in a Kollmorgen AKM 54K-ANCN2-00 SPMSM, the same studied for Case 1 in this research. For the machine acceleration under maximum torque to be in the order of seconds, it will be used a mechanical load, composed by an induction machine operating as a dynamometer: its torque will be equal to the torque applied on it up to a programmable level, and above said level it will be kept constant at it.

To have a base, critical and maximum speeds within reasonable and safe levels, the DC link voltage is set at $200V$ instead of the maximum $640V$. For the maximum torque to be within values that the load machine can safely handle, the maximum stator current will be set at $10A$ instead of $9.7\sqrt{2}A$.

The algorithm will be implemented in a MicroLabBox, a development system by the manufacturer dSPACE, which can be interfaced with a computer using MATLAB Simulink. The complete experimental setup can be seen in Figure 4.1.

The experimental validation will consist in two parts: an acceleration with a variable load and a deceleration with a fixed load.

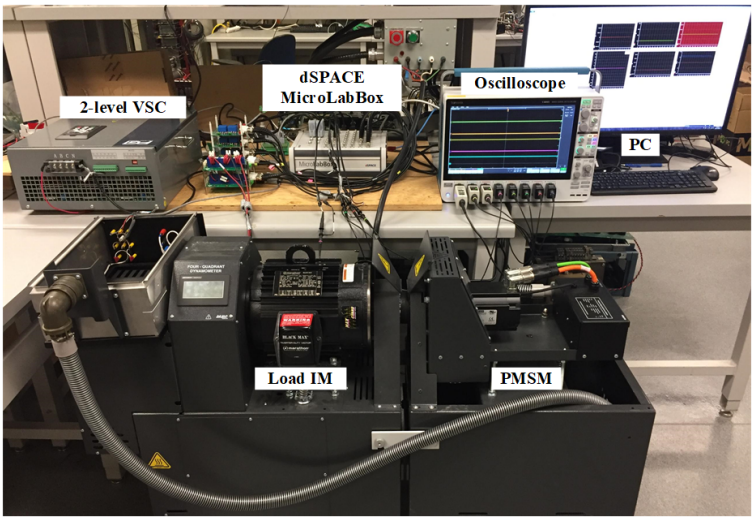

Figure 4.1: Experimental Setup

4.1 Experiment 1: System Startup at Maximum Torque

For this experiment, the system will start from a standstill with the induction machine operating as a dynamometer with a constant torque of $8Nm$. After reaching a steady state, the load torque will decrease to $2Nm$ in steps of $2Nm$, allowing the system to reach a new steady state after each load change. The system speed can be seen in Figure 4.2a. For the same experiment, the dq-frame currents in the time domain are seen in Figure 4.2b.

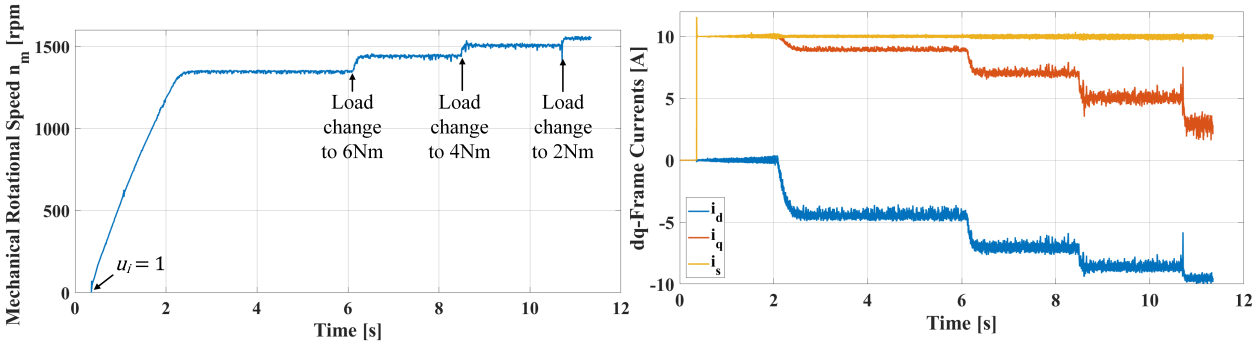

(a) System Speed

(b) dq-Frame Currents in the Time Domain

Figure 4.2: Experiment 1 Results

And, in a similar way, the dq-frame currents can be seen in the machine speed domain in Figure 4.3a. The thick dashed lines inside the experimental dq-frame currents are the currents calculated by the algorithm presented in the previous chapters. The fact that the

calculated and real currents are overlapping each other for all the speed range reached shows that the algorithm behaves properly. The currents plotted in the dq-plane are seen in Figure 4.3b, along with the current limiting circle as a dashed line.

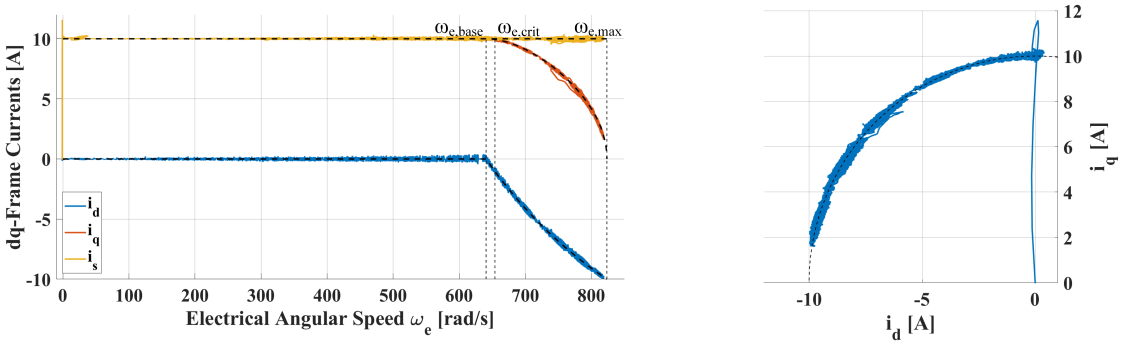

(a) In the Speed Domain

(b) In the dq-Plane

Figure 4.3: Experiment 1 dq-Frame Currents

It is also possible to see in Figure 4.4 that the abc-frame currents have a constant magnitude throughout the entire expriment, as expected.

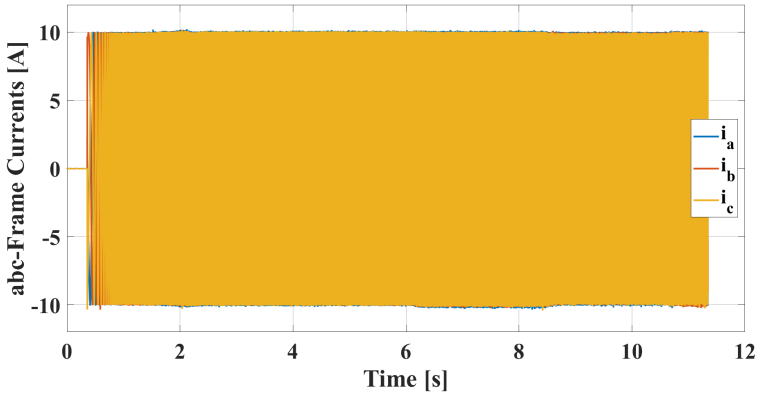

Figure 4.4: Experiment 1 abc-Frame Currents

Finally, the torque and power profiles can be compared with the calculated ones, while the latter ones are represented by dashed lines in Figure 4.5.

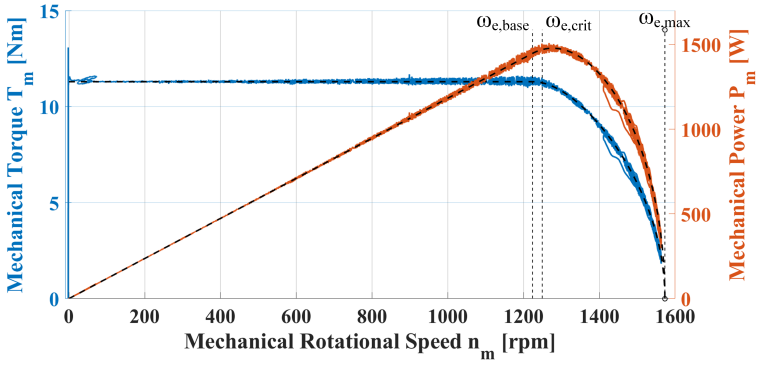

Figure 4.5: Experiment 1 Torque and Power Profiles

To be able to verify that the machine voltages are within limits, the output of the control system (*i.e.* the signals which are being used as references for the VSC switching) needs to be verified. In Chapter 3, it was verified the voltage references in the $\alpha\beta$-frame, since the SVM block used by PLECS has as output the switches' gate signals. For the dSPACE platform used for the experimental verification, the voltage constraint can be verified by using the duty cycle for the switches. Even though not the same signal, both are related by the SVM, and their maximum and minimum values – their envelope – can be used to verify the voltage constraint. The duty cycle for the upper switches of the VSC can be seen in Figure 4.6. This information is given in CPU cycles, which, for this experiment, must lie between 0 and 5000.

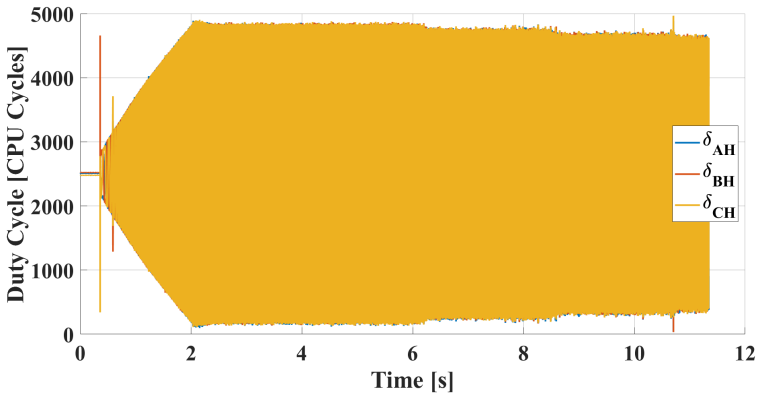

Figure 4.6: Experiment 1 Duty Cycles

It is possible to see in Figure 4.6 that the steady state voltages for each load are different from each other. While the algorithm presented was created in a way that the steady state voltages are the same for the field-weakening region – all the operating points lie over the

VLC – the stator resistance was neglected. It was discussed in section 2.9 that the voltage drop caused by the term $R_s i_{dq}$ is not constant for a changing frequency, since it does not affect v_{dq}, thus v_s, uniformly throughout all the speed range.

However, one might notice that the PWM references are almost hitting their limit. Since there is a 15.47% DC voltage increase due to the SVM, the PWM values should lie between 386.7 and 4613.2 CPU cycles, so the fact that these are reaching nearly 96 for the lowest value and 4890 for the highest value are likely due to the 10% tolerances on the values of λ_{pm}, L_{dq} and R_s given by the machine's manufacturer, indicating a higher back-EMF and resistive voltage drop.

4.2 Experiment 2: System Stop

The second experiment will consist in stopping the system after reaching a steady state under a constant load of $4Nm$ by reducing u_i from 1 to 0.4 in consecutive steps of 0.05, and then setting it to 0. The system speed can be seen in Figure 4.7a.

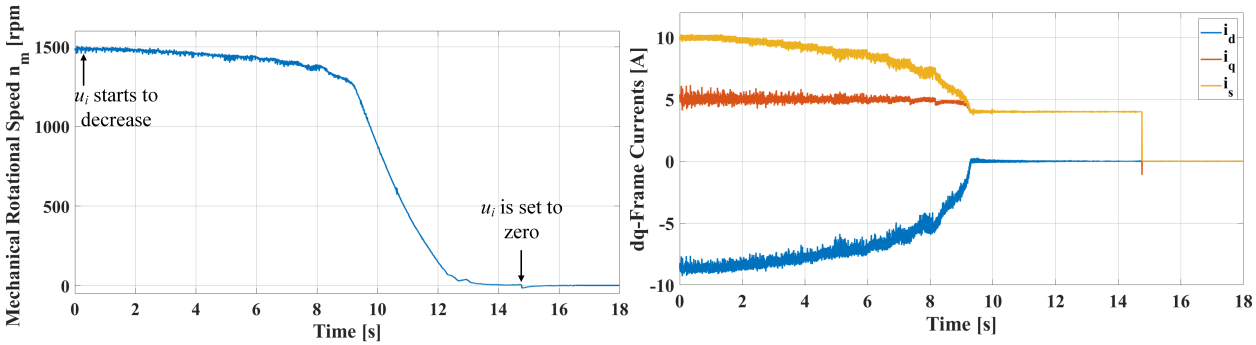

(a) System Speed

(b) dq-Frame Currents in the Time Domain

Figure 4.7: Experiment 2 Results

It is possible to see by Figures 4.7a and 4.7b that even though u_i decreased from 1 to 0.4, the q-axis current – and therefore torque – seems to be reduced very slightly. After each decrease in u_i, i_q decreases, but seems to increase again after a short amount of time. This is due to the decreasing torque with an increasing speed in the field-weakening region. From the steady state point of the beginning of this experiment, a decrease in u_i will decrease the machine torque, which according to (1.48) will decrease the system speed. For the same u_i, with a decrease in speed the machine will reach a new speed in which it is able to generate more torque, thus increasing its torque and finding a new steady state point. This happens

several times, until the machine leaves the field-weakening region, where its torque will not change for a decreasing speed. When the machine torque gets close to the load torque of $4Nm$, there is a very high deceleration, until the system reaches a new steady state at a very low speed, when u_i is set to 0, thus fully stopping the system. This very non-linear behaviour is mostly due to the dynamometer characteristic of the load machine instead of an inertia-friction model.

4.3 Experiment 3: Comparison to Traditional Methods

As a final experiment, the convential method of CVCP is implemented on the drive and the results, seen in Figure 4.8. As previously discussed, this method is simple, but not accurate.

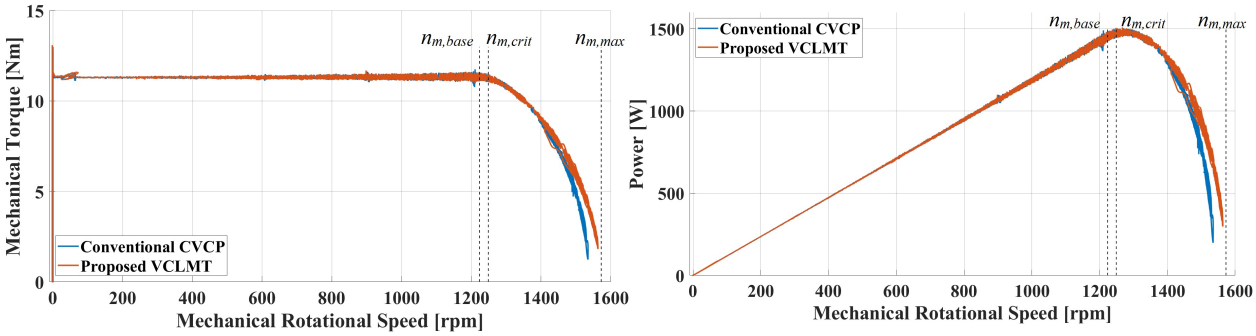

(a) Torque Comparison

(b) Power Comparison

Figure 4.8: Experiment 3 Results

As expected, the simplicity of the CVCP mehtod comes to a cost of performance on the field-weakening region, where the proposed VCLMT method discussed throughout this research was able to provide a higher torque – therefore, power – at higher speeds.

The experimental implementation was satisfactory.

Chapter 5

Conclusion and Future Work

5.1 Conclusion

This research's goal of obtaining a wide-speed control algorithm for any PMSM configuration was achieved. The mathematical modelling in the dq-plane using the plots from the machine equations was evaluated in a MATLAB script providing a good starting point for further development, since it was possible to visualize the dq-frame currents and voltages behaving as expected for all four cases: maximum torque achieved without overcurrents or overmodulation needed. It also demonstrated how the dq-frame currents and voltages behave under zero torque and their limitations. It also included the concepts of finite and in theory infinite speed machines.

A PLECS model was created using all the theory presented in the research and was able to prove that the mathematical modelling is valid in a simulation environment with the same results from the pure mathematical analysis. This was the motivation to move forward with the practical implementation, which concluded the algorithm developed can be used in a real VSC-driven PMSM.

It was observed during the experimental evaluation that the calculation for the machine speed based on a 12-bit incremental encoder provided some "speed ripple" when the MCU calculated the machine's speed: an oscillation of a few rpm, even in a constant speed, caused by the discretization of the position sensor. This speed ripple had no effect below the base speed and a very small effect in "early to middle field weakening operation". However, this effect became more pronounced once the machine was near its maximum speed. This instability in the speed calculation was reflected in the generation of the dq-frame currents, which, for finite speed machines, present a great rate of change in the q-axis current. Since

the machine analyzed was an SPMSM, the q-axis current is the sole contribution for torque generation, thus the speed ripple produced a torque ripple. This would be attenuated with a higher resolution incremental encoder, or solved with the use of a sine-encoder or a resolver for mechanical angle sensing.

The full utilization of the DC link voltage and stator currents showed that the PMSM can provide its optimal torque under any speed of its operating region, from motoring to coasting to regenerative braking, without forcing the machine to operate under overcurrent or overvoltage scenarios.

5.2 Recommendation of Future Work

One limitation of this research, however, is that all machine parameters were considered constants. In a practical scenario, the stator resistance R_s changes with temperature, and the most impacting ones, the dq-frame inductances L_d and L_q, will decrease as the machine core saturates under higher currents. Since the algorithms are based on said parameters, this will affect their performance and accuracy. One way to overcome the non-constant parameters is to consider these changes by utilizing the parameters as a look-up table or as a mathematical function, with data obtained from the machine's manufacturer or by experimental results with the aid of a torque sensor.

References

[1] J. Islam, S. Nategh, R. R. Moghaddam, and A. Boglietti, "Different Traction Motor Topologies Used in E-mobility : Part I: Solutions Without Magnet," *2020 International Conference on Electrical Machines (ICEM)*, 2020.

[2] ——, "Different Traction Motor Topologies Used in E-Mobility : Part II: Magnet-Based Solutions," *2020 International Conference on Electrical Machines (ICEM)*, 2020.

[3] S. Sharifan, S. Ebrahimi, A. Oraee, and H. Oraee, "Performance Comparison Between Brushless PM and Induction Motors for Hybrid Electric Vehicle Applications," *International Conference on Optimization of Electrical and Electronic Equipment (OPTIM)*, 2015.

[4] J. Goss, M. Popescu, and D. Staton, "A Comparison of an Interior Permanent Magnet and Copper Rotor Induction Motor in a Hybrid Electric Vehicle Application," *International Electric Machines and Drives Conference*, 2013.

[5] D. G. Dorrell, M. Popescu, L. Evans, D. A. Staton, and A. M. Knight, "Comparison of Permanent Magnet Drive Motor with a Cage Induction Motor Design for a Hybrid Electric Vehicle," *International Power Electronics Conference - ECCE Asia*, 2010.

[6] X. Zhang, L. Zeng, and R. Pei, "Designing and Comparison of Permanent Magnet Synchronous Reluctance Motors and Conventional Motors in Electric Vehicles," *International Conference on Electrical Machines and Systems (ICEMS)*, 2018.

[7] J. Kammermann, I. Bolvashenkov, and H. Herzog, "Approach for Comparative Analysis of Electric Traction Machines," *International Conference on Electrical Systems for Aircraft, Railway, Ship Propulsion and Road Vehicles (ESARS)*, 2015.

[8] J. Kammermann, I. Bolvashenkov, S. Schwimmbeck, and H. Herzog, "Techniques for Comparative Analysis and its Application to Electric Traction Machines," *19th International Conference on Electrical Machines and Systems (ICEMS)*, 2016.

[9] A. Walker, M. Galea, C. Gerada, A. Mebarki, and D. Gerada, "A topology Selection Consideration of Electrical Machines for Traction Applications: Towards the FreedomCar 2020 Targets," *Tenth International Conference on Ecological Vehicles and Renewable Energies (EVER)*, 2015.

[10] S. Jurkovic, K. M. Rahman, and P. J. Savagian, "Design, Optimization and Development of Electric Machine for Traction Application in GM Battery Electric Vehicle," *IEEE International Electric Machines and Drives Conference (IEMDC)*, 2015.

[11] Y. Shimizu, S. Morimoto, M. Sanada, and Y. Inoue, "Influence of Permanent Magnet Properties and Arrangement on Performance of IPMSMs for Automotive Applications," *19th International Conference on Electrical Machines and Systems (ICEMS)*, 2016.

[12] K. T. Chau, C. C. Chan, and C. Liu, "Overview of Permanent-Magnet Brushless Drives for Electric and Hybrid Electric Vehicles," *IEEE Transactions on Industrial Electronics*, 2008.

[13] X. Liu, H. Chen, J. Zhao, and A. Belahcen, "Research on the Performances and Parameters of Interior PMSM Used for Electric Vehicles," *IEEE Transactions on Industrial Electronics*, 2016.

[14] J. Nerg, M. Rilla, V. Ruusanen, J. Pyrhonen, and S. Ruotsalainen, "Direct-Driven Interior Magnet Permanent-Magnet Synchronous Motors for a Full Electric Sports Car," *IEEE Transactions on Industrial Electronics*, 2014.

[15] A. Yazdani and R. Iravani, *Voltage-Sourced Converters in Power Systems: Modeling, Control, and Applications*. John Wiley & Sons, Inc., 2010.

[16] M. Li, "Flux-Weakening Control for Permanent-Magnet Synchronous Motors Based on Z-Source Inverters," M.S. thesis, Marquette University, 2014.

[17] T. Martin and R. Burke, "Practical Field Weakening Current Vector Control Calculations for PMSM in Vehicle Applications," *2013 World Electric Vehicle Symposium and Exhibition (EVS27)*, 2013.

[18] H. J. Won, "Development and Evaluation of a Novel Neural Network of PMSM for Electric Vehicle," M.S. thesis, The University of Alabama, 2016.

[19] MathWorks, *MTPA Control Reference*, Website, 2022. [Online]. Available: `https://www.mathworks.com/help/mcb/ref/mtpacontrolreference.html`.

[20] B. Wu and M. Narimani, *High-Power Converters and AC Drives*. John Wiley & Sons, Inc., 2017.

[21] D. G. Holmes and T. A. Lipo, *Pulse Width Modulation for Power Converters*. John Wiley & Sons, Inc., 2003.

[22] L. Qinghua, "Analysis, Design and Control of Permanent Magnet Synchronous Motors for Wide-Speed Operation," Ph.D. dissertation, National University of Singapore, 2005.

[23] A. Parviainen, "Design of Axial-Flux Permanent-Magnet Low-Speed Machines and Performance Comparison Between Radial-Flux and Axial-Flux Machines," Ph.D. dissertation, Lappeenranta University of Technology, 2005.

[24] J. F. Gieras, R.-J. Wang, and M. J. Kamper, *Axial Flux Permanent Magnet Brushless Machines*. Springer, 2008.

[25] B. Armstrong and C. C. de Wit, *Friction Modeling and Compensation: The Control Handbook*. CRC Press, 1995.

[26] Group PED4-1038C, "Torque Control in Field Weakening Mode," M.S. thesis, Aalborg University, 2009.

[27] T. M. Jahns, *Modeling, Simulation and Control of Electrical Drives*, M. F. Rahman and S. K. Dwivedi, Eds. The Institution of Engineering and Technology, 2019.

[28] W. Huang, Y. Zhang, X. Zhang, and G. Sun, "Accurate Torque Control of Interior Permanent Magnet Synchronous Machine," *IEEE Transactions on Energy Conversion*, 2014.

[29] B. Boazzo and G. Pellegrino, "Model-Based Direct Flux Vector Control of Permanent-Magnet Synchronous Motor Drives," *IEEE Transactions on Industry Applications*, 2015.

[30] E. M. Prodanov, "Classification of the Real Roots of the Quartic Equation andtheir Pythagorean Tunes," *Int. J. Appl. Comput. Math (2021) 7:218*, 2021.

[31] R. W. D. Nickalls, "The Quartic Equation: Invariants and Euler's Solution Revealed," *The Mathematical Gazette (2009); vol. 93 (March; No. 526), pp. 66–75*, 2009.

[32] E. Weisstein, *Quartic Equation*, Website, 2022. [Online]. Available: `https://mathworld.wolfram.com/QuarticEquation.html`.

[33] S.-Y. Jung, J. Hong, and K. Nam, "Current Minimizing Torque Control of the IPMSM Using Ferrari's Method," *IEEE Transactions on Power Electronics*, 2013.